

VIBRATION AND ACOUSTICAL PROPERTIES OF SANDWICH COMPOSITE  
MATERIALS

Except where reference is made to the work of others, the work described in this dissertation is my own or was done in collaboration with my advisory committee.  
This dissertation does not include proprietary or classified information.

---

Zhuang Li

Certificate of approval:

---

Subhash C. Sinha  
Professor  
Mechanical Engineering

---

Malcolm J. Crocker, Chair  
Distinguished University Professor  
Mechanical Engineering

---

George T. Flowers  
Professor  
Mechanical Engineering

---

A. Scottedward Hodel  
Associate Professor  
Electrical Engineering

---

Stephen L. McFarland  
Acting Dean  
Graduate School

VIBRATION AND ACOUSTICAL PROPERTIES OF SANDWICH COMPOSITE  
MATERIALS

Zhuang Li

A Dissertation

Submitted to

the Graduate Faculty of

Auburn University

in Partial Fulfillment of the

Requirements for the

Degree of

Doctor of Philosophy

Auburn, Alabama  
May 11, 2006

VIBRATION AND ACOUSTICAL PROPERTIES OF SANDWICH COMPOSITE  
MATERIALS

Zhuang Li

Permission is granted to Auburn University to make copies of this dissertation at its discretion, upon request of individuals or institutions and at their expense.  
The author reserves all publication rights.

---

Signature of Author

---

Date of Graduation

## VITA

Zhuang Li, son of Shouan Li and Shuxian Hao, was born on September 4, 1975, in Shijiazhuang, Hebei Province, China. He graduated from the Middle School Attached to Hebei Normal University in 1994. He entered Tianjin University, Tianjin, China in September 1994, and graduated with two Bachelor of Engineering degrees in Precision Instrument Engineering and Industrial Engineering in July 1998. He continued his study in Tianjin University in September 1998, and obtained Master of Engineering degree in Precision Instruments and Machinery in March 2001. He entered Graduate School, Auburn University, in August 2001. He married to Yan Du, daughter of Xingrun Du and Fengqin Liu, on December 25, 2002.

DISSERTATION ABSTRACT  
VIBRATION AND ACOUSTICAL PROPERTIES OF SANDWICH COMPOSITE  
MATERIALS

Zhuang Li

Doctor of Philosophy, May 11, 2006  
(M.E., Tianjin University, 2001)  
(B.E., Tianjin University, 1998)

203 Typed Pages

Directed by Malcolm J. Crocker

In applications where the use of lightweight structures is important, the introduction of a viscoelastic core layer, which has high inherent damping, between two face sheets, can produce a sandwich structure with high damping. Composite sandwich structures have several advantages, such as their high strength-to-weight ratio, excellent thermal insulation, and good performance as water and vapor barriers. So in recent years, such structures have become used increasingly in transportation vehicles. However their fatigue, vibration and acoustic properties are known less. This is a problem since such composite materials tend to be more brittle than metals because of the possibility of delamination and fiber breakage. Structures excited into resonant vibration exhibit very high amplitude displacements which are inversely proportional to their passive damping. The transmission loss of such composite panels is also poor at coincidence. Their passive

damping properties and attempts to improve their damping at the design stage are important, because the damping properties affect their sound transmission loss, especially in the critical frequency range, and also their vibration response to excitation.

The research objects in this dissertation are polyurethane foam-filled honeycomb sandwich structures. The foam-filled honeycomb cores demonstrate advantages of mechanical properties over pure honeycomb and pure foam cores. Previous work including theoretical models, finite element models, and experimental techniques for passive damping in composite sandwich structures was reviewed. The general dynamic behavior of sandwich structures was discussed. The effects of thickness and delamination on damping in sandwich structures were analyzed. Measurements on foam-filled honeycomb sandwich beams with different configurations and thicknesses have been performed and the results were compared with the theoretical predictions. A new modal testing method using the Gabor analysis was proposed. A wavelet analysis-based noise reduction technique is presented for frequency response function analysis. Sound transmission through sandwich panels was studied using the statistical energy analysis (SEA). Modal density, critical frequency, and the radiation efficiency of sandwich panels were analyzed. The sound transmission properties of sandwich panels were simulated using AutoSEA software. Finite element models were developed using ANSYS for the analysis of the honeycomb cell size effects. The effects of cell size on both the Young's modulus and the shear modulus of the foam-filled honeycomb core were studied in this research. Polyurethane foam may produce a negative Poisson's ratio by the use of a special microstructure design. The influence of Poisson's ratio on the material properties was also studied using a finite element model.

## ACKNOWLEDGMENTS

The Author would like to express his sincere appreciation and thanks to his advisor Professor Malcolm J. Crocker for his guidance during the studies. All the committee members provided considerable assistance for which I am grateful. My appreciation also goes to my friends and colleagues at Auburn University. Last and not least, I want to express my special thanks to my parents Shouan Li and Shuxian Hao, and my wife Yan Du, for their support and love.

Journal used: Journal of Sound and Vibration

Computer software used: Microsoft Word 2002



## TABLE OF CONTENTS

LIST OF TABLES . . . . .	xii
LIST OF FIGURES . . . . .	xiii
CHAPTER 1 INTRODUCTION. . . . .	1
1.1 Sandwich Composite Materials . . . . .	1
1.2 Motivation for Research . . . . .	4
1.3 Organization of Dissertation . . . . .	6
CHAPTER 2 LITERATURE OVERVIEW . . . . .	12
2.1 Overview of Damping . . . . .	12
2.1.1 Damping mechanisms . . . . .	13
2.1.2 Measures of damping . . . . .	15
2.1.3 Measurement methods . . . . .	16
2.2 Damping in Sandwich Structures . . . . .	17
2.2.1 Analytical models . . . . .	18
2.2.2 Damping and damage . . . . .	26
2.2.3 Finite element models . . . . .	27
2.2.4 Statistical energy analysis method . . . . .	29
CHAPTER 3 ANALYSIS OF DAMPING IN SANDWICH MATERIALS . . . . .	40
3.1 Equation of Motion . . . . .	41
3.2 Effects of Thickness . . . . .	46

3.3 Effects of Delamination . . . . .	51
3.4 Damping Improvement using Multi-layer Sandwich Structures . . . . .	51
3.5 Experiments . . . . .	55
3.5.1 Experimental setup . . . . .	55
3.5.2 Experimental results . . . . .	56
3.5.3 Discussion . . . . .	57
CHAPTER 4 DAMPING CALCULATION AND MODAL TESTING . . . . .	74
USING WAVELET AND GABOR ANALYSES	
4.1 Wavelet and Gabor Analyses . . . . .	75
4.2 Modal Extraction using Wavelet Analysis . . . . .	79
4.3 Damping Calculation using Gabor Analysis . . . . .	82
4.3.1 Decouple modes using Gabor analysis . . . . .	83
4.3.1 Damping calculation . . . . .	85
4.3.2 Simulations . . . . .	86
4.3.3 Comparison with FFT-based technique. . . . .	88
4.4 Modal Testing using Gabor Transform . . . . .	89
4.5 Experiments . . . . .	92
4.5.1 Experimental setup . . . . .	92
4.5.2 Natural frequency and mode shape . . . . .	93
4.5.3 Damping ratio . . . . .	93
CHAPTER 5 ANALYSIS OF SOUND TRANSMISSION THTROUGH . . . . .	110
SANDWICH PANELS	
5.1 Review of the Sound Transmission Loss of Sandwich Panels . . . . .	111

5.2 Prediction of Sound Transmission through Sandwich Panels using SEA	115
5.2.1 Modal density	119
5.2.2 Analysis of critical frequency	120
5.3 Experimental Results and Discussion	122
5.3.1 Transmission loss measurement using two-room method	122
5.3.2 Transmission loss measurement using sound intensity method	124
5.3.3 Radiation efficiency	125
5.3.4 Simulation using AutoSEA	126
5.3.5 Experimental and simulation results	127
CHAPTER 6 ANALYSIS OF FOAM-FILLED HONEYCOMB CORES USING FEM	144
6.1 Size Effect on the Young's Modulus	145
6.2 Size Effect on the Shear Modulus.	148
6.3 Influence of Poisson's Ratio	150
6.4 More Considerations of Cell Size Effects.	152
CHAPTER 7 CONCLUSIONS	164
REFERENCES	169
APPENDICES	179
APPENDIX A MATLAB PROGRAMS FOR WAVENUMBER AND WAVE SPEED OF SANDWICH PANELS	180
APPENDIX B MATERIAL PROPERTIES OF SANDWICH PLATES	183
NOMENCLATURE	184

## LIST OF TABLES

Table 2.1. Formulas used to calculate the loss factor by different methods .	17
Table 3.1. Configurations of intact beams . . . . .	59
Table 3.2. Configurations of beams with delamination . . . . .	59
Table 4.1. Detected natural frequencies and damping ratios for simulated . signals with different noise level	95
Table 4.2. Damping ratios of two-mode decay signal calculated using . Gabor expansion	95
Table 4.3. Damping results calculated using the Gabor spectrogram method	96
Table 4.4. Comparison of the SNRs of the signals reconstructed using . the FFT method and the Gabor expansion method	96
Table 4.5. Error analysis of the new modal testing method . . . . .	97
Table 4.6. Damping ratios calculated using the Gabor expansion method . and the Gabor spectrogram method	97
Table 5.1. Geometry parameters of panels under study. . . . .	130
Table 5.2. Reverberation times of the receiving room with different panels .	131
Table 6.1. Cell size effect on the Young's modulus of foam-filled . . . . . honeycomb beams	153
Table 6.2. Influence of aspect ratio on the shear modulus calculation using FEM	154
Table 6.3. Cell size effect on the shear modulus of foam-filled honeycomb beams	155

## LIST OF FIGURES

Figure 1.1. Corrugation process used in honeycomb manufacture . . .	9
Figure 1.2. Fabrication of foam-filled honeycomb sandwich panels . . .	10
Figure 1.3. (a) Polyurethane foam-filled paper honeycomb core . . .	11
(b) Built-up sandwich beam with carbon fiber face sheets	
Figure 2.1. The effect of the shear modulus on the total damping . . .	33
in a sandwich structure	
Figure 2.2. The effects of the shear and structural parameters . . .	34
on the system loss factor	
Figure 2.3. The frequency dependence of the damping in sandwich structures	35
Figure 2.4. The shear parameter effect on the total damping . . .	36
in multi-layer sandwich beams	
Figure 2.5. A sandwich beam with a spacer beneath the damping layer . . .	37
Figure 2.6. Variation of modal loss factor with the normalized shear modulus	38
Figure 2.7. Internal damping treatment . . . . .	39
Figure 3.1. A symmetric sandwich beam . . . . .	60
Figure 3.2. Dispersion relation for sandwich beams with a single . . .	61
foam core and a foam-filled honeycomb core	
Figure 3.3. The cross section of a five-layer sandwich beam. . . . .	62
Figure 3.4. A beam with 50.8 mm delaminations on both sides . . . . .	63



	cantilever beam. (b) The wavelet scalogram. (c) The original Gabor coefficients. (d) The Gabor spectrogram	
Figure 4.5.	(a) The original Gabor coefficients of signal shown in Fig 4.4 (a) (b) (c) (d) The modified Gabor coefficients of three modes by using three mask matrices	102
Figure 4.6.	The decoupled modal responses using Gabor expansion. (a) the first mode, (b) the second mode, (c) the third mode, and (d) spectra of the three reconstructed signals	103
Figure 4.7.	Damping calculation simulation using the Gabor transform (a) A simulated free vibration signal, (b) the original Gabor coefficients of this signal, (c) and (d) the reconstructed modal responses, and (e) and (f) envelopes established using the Hilbert transform and the best exponential fits	104
Figure 4.8.	Damping calculation simulation using the Gabor spectrogram (a) A simulated free vibration signal, (b) the Gabor spectrogram, (c) and (d) the two vibration modes calculated using zoom Gabor spectrogram	105
Figure 4.9.	The original complex FFT of a free vibration signal containing three modes. (a) Real part, (b) imaginary part	106
Figure 4.10.	Comparison of the envelopes of the displacement components reconstructed using the FFT and Gabor expansion methods. (a) First mode, (b) second mode, (c) third mode	107
Figure 4.11.	Experimental setup for modal testing	108

Figure 4.12. Comparison of the theoretical and measured mode shapes	109
Figure 5.1. Schematic of the power flow in three-coupled systems using SEA	116
Figure 5.2. Modal distribution of isotropic and anisotropic plates	132
Figure 5.3. Side views of the two reverberation rooms, and experimental setup for transmission loss measurements using intensity probe method	133
Figure 5.4. Comparison of sound transmission loss measurements of composite Plate A using two-room method and sound intensity method	134
Figure 5.5. Sound transmission loss model using AutoSEA software	135
Figure 5.6. Measured and simulated radiation efficiency of Panel E.	136
Figure 5.7. Sound transmission loss of Panel E	137
Figure 5.8. Measured and simulated radiation efficiency of Panel A.	138
Figure 5.9. Measured and simulated radiation efficiency of Panel B.	139
Figure 5.10. Measured and simulated sound transmission loss of Panel A	140
Figure 5.11. Measured and simulated transmission loss of Panel B	141
Figure 5.12. Comparison of sound transmission loss and sound transmission class of plates in study	142
Figure 5.13. Comparison of sound transmission loss and sound transmission class of Plate A and an aluminum plate having the same surface density	143
Figure 6.1. (a) A section of the honeycomb structure. (b) Beam element used to model the honeycomb cell wall	156
Figure 6.2. Cell size effect on the Young's modulus of pure honeycomb structures	157



Figure 6.3. (a) A section of the honeycomb structure.	158
(b) Beam element used to model the honeycomb cell wall	
Figure 6.4. (a) Schematic of the shear modulus calculation. (b) Foam-filled honeycomb finite element mesh and pure shear deformation	159
Figure 6.5. Honeycomb cell size effect on Young's modulus and shear modulus of foam-filled honeycomb structures	160
Figure 6.6. Microstructures giving negative Poisson's ratios.	161
Figure 6.7. Influence of Poisson's ratio on the Young's modulus of foam-filled honeycomb structures	162
Figure 6.8. Influence of Poisson's ratio on the shear modulus of foam-filled honeycomb structures	163

## CHAPTER 1 INTRODUCTION

### 1.1 Sandwich Composite Materials

Attempts have been made to reduce vibration and its transmission through structures and mechanical systems for many years. When an unacceptable noise or vibration problem needs to be solved, it is necessary to understand it completely, for example, the sources of the noise and vibration, the path along which the energy is transmitted, its frequency contents, and other related aspects such as thermal insulation, impact properties, cost, etc. Noise and vibration control methods fall into two categories, active and passive.

Passive control involves modification of the mass, stiffness and (or) damping of the system to make it less sensitive to the noise and vibration environments. In passive control, some structural changes may be made (for example, de-tuning), or some additional elements, such as double walls, spring isolators, and dampers, may be introduced. All these elements simply respond to the sound pressures, deflections, velocities or accelerations which are caused by the other structural components. They do not require external assistance.

On the other hand, active control systems require an external source of power to drive the active devices. Although active control systems may be more effective and

reliable than passive methods, especially at low frequencies, they are more expensive. Active systems must be properly maintained, which also increases the cost.

In applications where the use of lightweight structures is important, the introduction of a viscoelastic damping layer between two face sheets, can produce a sandwich structure with high damping. Sandwich structures have the additional advantage that their strength-to-weight ratios are generally superior to those of metals. The core also increases the thickness of the structure, which leads to an increase in stiffness of the sandwich structure. The increase in stiffness also reduces the modal density of the structure which is proportional to  $1/\sqrt{\text{stiffness}}$ . Therefore, the total RMS response will be lower with the reduced number of modes because the total response depends on the number of modes which are excited.

The ASTM (American Society for Testing and Materials) standards define a sandwich structure as follows: *“a laminar construction comprising a combination or alternating dissimilar simple or composite materials assembled and intimately fixed in relation to each other so as to use the properties of each to attain specific structural advantages for the whole assembly.”* (ASTM C 274-99)

Even though the extensive development of sandwich technology has occurred in the last two or three decades, sandwich construction has been used for more than a century. Fairbairn was reported to be the first person to describe the principle of sandwich constructions way back in 1849. The Mosquito fighter-bomber, built by the De Havilland Aircraft Company in England during World War Two, however, is regarded as the first major application of sandwich panels. The excellent performance demonstrated by this airplane instigated new research to improve techniques of fabricating sandwich

structures and developing new materials to act as facings and cores. The landing of the Apollo space vehicle on the Moon in 1969 marked another significant achievement of sandwich technology. The Apollo capsule was made from a sandwich structure of steel face sheets and an aluminium honeycomb core which was lightweight and yet strong enough to sustain the stresses of launch acceleration and landing deceleration [1-3].

Honeycomb cores, which were developed starting in the 1940's primarily for aerospace industry, have the greatest shear strength and stiffness-to-weight ratios, but require special care to ensure adequate bonding of the face sheets to the core since honeycomb cores are hollow. The standard hexagonal honeycomb is the basic and most common cellular honeycomb configuration, and is currently available in many metallic and nonmetallic materials. Figure 1.1 illustrates the manufacture process, and the L- (ribbon direction) and W- (transverse to the ribbon) directions of the hexagonal honeycomb. In this process, adhesive is applied to the corrugated nodes, the corrugated sheets are stacked into blocks, the node adhesive cured, and sheets are cut from these blocks to the required core thickness. The honeycomb cores are suitable for both plane and curved sandwich applications.

Relatively recent developments in high quality cellular foams have greatly increased the use of sandwich structures. Although cellular foams do not offer such high stiffness-to-weight ratios as honeycomb cores, they have other important features. For example, a foam core is solid on a macroscopic level; so it is easier to bond it to the face sheets. The viscoelasticity of some foam materials leads to higher vibration damping. In addition, the closed cellular foams make the sandwich structure buoyant and resistant to water penetration.

Nowadays, sandwich structures with different face sheet and core materials are increasingly used in various applications. Sandwich structures have many advantages including high stiffness-to-weight and strength-to-weight ratios, high damping capacities, good thermal insulation properties, excellent water and vapour barrier performance, good corrosion resistance, and low cost.

## **1.2 Motivation for Research**

Although sandwich structures have significant advantages, they have some less favorable properties. For example, their high stiffness-to-weight ratio reduces the critical frequency of a sandwich panel. In addition, because sandwich panels are generally orthotropic, the critical frequencies, unlike those of metals, are actually situated in a frequency band instead of at one particular frequency. These features usually result in poor sound transmission loss over a wider frequency range. Additionally, composite materials tend to be more brittle than metals. Because of delamination, debonding and fiber breakage, fatigue in composite materials is of more concern than in metals because of the sudden catastrophic failure that can occur.

Knowledge of the passive damping of sandwich structures and attempts to improve their damping at the design stage thus are important. Analytical models for the sound transmission loss of panels also require knowledge of the damping of the face plates and core materials which is contributed not only by the material, but also by the panel boundaries and acoustic radiation. This dissertation concentrates on improving the damping and sound transmission of sandwich structures.

Cores made of both honeycomb and solid viscoelastic materials have been studied extensively [58,59,100,105-107]. The core used in this dissertation is made of paper honeycomb filled with polyurethane (PUR) foam. As described before, honeycomb material is expected to enhance the stiffness of the entire structure, while the foam improves the damping. In this study, the material for the face sheet is a carbon fiber reinforced composite. Figure 1.2 shows the manufacturing setup for such foam-filled honeycomb sandwich plates. Face sheets and cores of different thicknesses are layered in a vacuum bag according to the configuration design. These laminates are pre-treated with an adhesive. A vacuum pump is used and results in atmosphere pressure applied to the whole sample. If heating is required for adhesive curing, the sample with its vacuum bag can be placed in an oven. Figure 1.3 illustrates a PUR foam-filled honeycomb core and a built sandwich beam sample.

Jung and Aref have reported that sandwich structures with combined honeycomb-foam cores have higher damping than those with individual honeycomb or solid viscoelastic cores [4]. However, Jung and Aref used a static hysteretic damping model, in which the damping ratio is independent of frequency. Their conclusion is obviously not valid. In this dissertation the frequency dependence of damping in sandwich beams with foam-filled honeycomb cores is analyzed, and the effects of thickness of the face sheets and the core, and delamination on damping have been studied. Most of the earlier models ignore the bending and extensional effects in the core. However, this assumption is only valid for soft thin cores. In this dissertation both the bending and shear effects in the core are considered. In the theoretical modal the shear stresses are continuous across the face sheet-core interfaces.

Besides the analysis of the vibration properties of sandwich constructions as structural elements, a study of their acoustical properties must also be taken into account in the initial design stages of aircrafts, automobiles and ships. This is necessary so that the weight saving advantages produced by composites are not compromised by high noise transmission, which would require heavy add-on acoustical treatments in later design stages. In many applications, it is important to know the sound transmission characteristics of the sandwich panels used in order to minimize the sound transmission from the engine into the cabin.

A structural element is generally expected to possess high stiffness (high Young's modulus). In addition, in order to raise the critical frequency out of the audible frequency range, a sandwich panel is expected to have a low shear modulus so that shear waves, rather than bending waves, are dominant at the frequencies of interest. A change of the honeycomb cell size results in changes of both the Young's modulus and the shear modulus of the core. Finite element models were developed to study the size effect of honeycomb cell.

Experiments were conducted to verify the analytical models presented in this dissertation, and to qualitatively determine the vibration damping and sound transmission characteristics. During the experiments, a new damping calculation method based on the Gabor transform was developed. This method can also be used in modal analysis.

### **1.3 Organization of Dissertation**

This dissertation contains the results of the present investigation into the objectives already described. The research work was performed in the Sound and Vibration

Laboratory of the Department of Mechanical Engineering at Auburn University. The results reported are divided into six major chapters.

A thorough review of the damping in sandwich structures is given in Chapter 2. Previous work including theoretical models, finite element models, and experimental techniques for passive damping in composite sandwich structures is reviewed in this chapter. The general dynamic behavior of sandwich structures is discussed.

Chapter 3 analyzes the effects of thickness and delamination on damping in sandwich structures. Measurements on foam-filled honeycomb sandwich beams with different configurations and thicknesses have been performed and the results were compared with the theoretical predictions. The stress-strain relationship and damping of a five-layered sandwich structure are also studied.

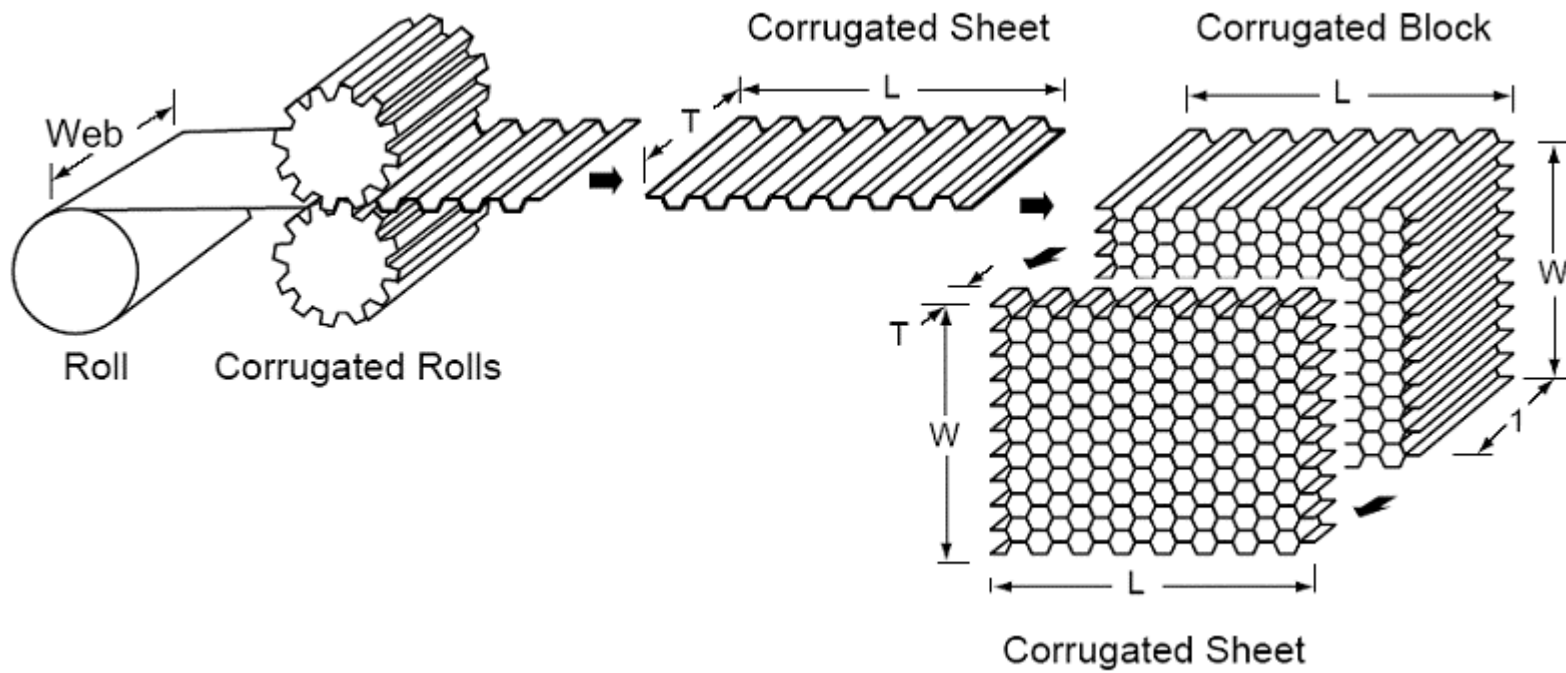
Chapter 4 deals with a new modal testing method using the joint time-frequency analysis. A wavelet analysis-based noise reduction technique is presented for frequency response function analysis. Additionally, a new damping calculation method was developed using the Gabor transform and Gabor spectrogram, and is presented in this chapter.

Chapter 5 is devoted to the study of sound transmission through sandwich panels. This chapter starts with a brief review of the previous research work on sound transmission through sandwich panels. Modal density, critical frequency, and the radiation efficiency of sandwich panels are analyzed. Simulations of the radiation efficiency and the sound transmission loss were conducted using AutoSEA. Experimental results are presented as well.



Chapter 6 covers the use of finite element models for the analysis of the honeycomb cell size effect. The finite element models were developed using ANSYS. The effects of cell size on both the Young's modulus and the shear modulus of the foam-filled honeycomb core were studied in this research. PUR foam may produce a negative Poisson's ratio by the use of a special microstructure design. The influence of Poisson's ratio on the material properties is also presented in this chapter.

The conclusions drawn from this research are given in chapter 7.

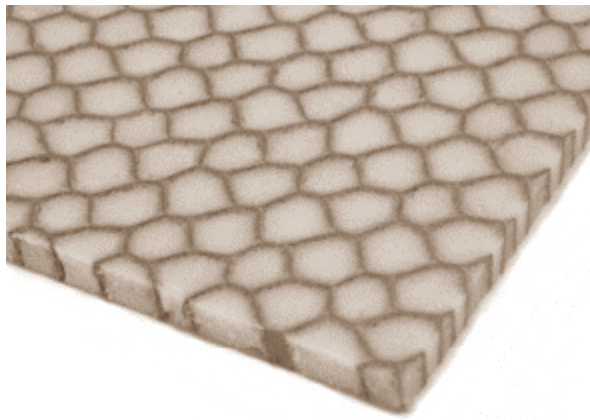


6

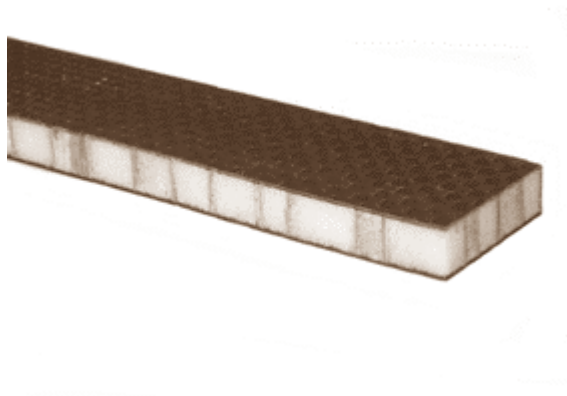
Figure 1.1. Corrugation process used in honeycomb manufacture.



Figure 1.2. Fabrication of foam-filled honeycomb sandwich panels.



(a)



(b)

Figure 1.3. (a) Polyurethane foam-filled paper honeycomb core. (b) Built-up sandwich beam with carbon fiber face sheets.

## CHAPTER 2 LITERATURE OVERVIEW

### 2.1 Overview of Damping

The three essential parameters that determine the dynamic responses of a structure and its sound transmission characteristics are mass, stiffness and damping. Mass and stiffness are associated with storage of energy. Damping results in the dissipation of energy by a vibration system. For a linear system, if the forcing frequency is the same as the natural frequency of the system, the response is very large and can easily cause dangerous consequences. In the frequency domain, the response near the natural frequency is “damping controlled”. Higher damping can help to reduce the amplitude at resonance of structures. Increased damping also results in faster decay of free vibration, reduced dynamic stresses, lower structural response to sound, and increased sound transmission loss above the critical frequency.

There is much literature published on vibration damping. ASME published a collection of papers on structural damping in 1959 [5]. Lazan’s book published in 1968 gave a very good review on damping research work, discussed different mechanisms and forms of damping, and studied damping at both the microscopic and macroscopic levels [6]. This book is also valuable as a handbook because it contains more than 50 pages of data on damping properties of various materials, including metals, alloys, polymers, composites, glass, stone, natural crystals, particle-type materials, and fluids. About 20

years later, Nashif, Jones and Henderson published another comprehensive book on vibration damping [7]. Jones himself wrote a handbook especially on viscoelastic damping 15 years later [8]. Sun and Lu's book published in 1995 presents recent research accomplishments on vibration damping in beams, plates, rings, and shells [9]. Finite element models on damping treatment are also summarized in this book. There is also other good literature available on vibration damping [10-12].

### **2.1.1 Damping mechanisms**

There are many damping mechanisms that convert mechanical energy from a vibratory system into heat and other energy forms. Basically damping mechanisms fall into one of the two categories: external and internal.

#### **External damping mechanisms**

External damping mechanisms include acoustic radiation damping, Coulomb friction damping, joint and boundary damping and so on. The dynamic response of a structure couples with the surrounding fluid medium, such as air, water or other liquid, in different ways, for example, by the creation of bending and shear waves. The damping effects of a fluid medium depends on various factors, including the density of the medium, the sound wave speed and the mass and stiffness characteristics of the structure itself [7]. The sound radiation of panels has been studied by Lyon, Maidanik, Crocker, Clarkson, Mead and other researchers [13-17]. For a solid homogenous panel, the acoustic radiation damping is proportional to the so-called radiation efficiency. For modes whose natural frequencies are higher than the critical frequency, the acoustic

radiation damping is high. At the critical frequency, because the bending wavelength is the same as the wavelength of sound wave propagating in air, the radiation efficiency as well as the acoustic damping is greatest. The acoustic radiation damping is generally small for modes below the critical frequency.

It is worth noticing that some vibration problems benefit from, and others are hurt by, an increase in the acoustic radiation damping [12]. For example, since the radiation loss factor of a sandwich structure is normally much higher than its internal loss factor, if it is excited in a diffuse sound field, then the time-averaged structural vibration levels are almost independent of the acoustic damping. In addition, since the radiation loss factor is proportional to the radiation efficiency, which affects the sound transmission loss, an increase in the acoustic radiation damping leads to a reduction in the sound transmission loss [15]. For a particular problem, the overall effects of damping and other factors on the structural response and sound radiation must be considered.

If a structure is made of normal engineering materials, the material damping is usually smaller than the joint damping. Joint fasteners can be comprised of bolts, rivets, adhesive layers or line welds. This is minimal at a welded joint because the surrounding material is virtually continuous. Adhesive bonding layers are thin and bonding materials are rigid. Therefore, the damping of bonded structures tends to be lower than that of structures with bolted and riveted joints [12].

### **Internal damping mechanisms**

Internal damping, or material damping, refers to the conversion of vibrational energy into heat within the volume of the material. Reference [7] tabulates some of the most important mechanisms including magnetic effects, thermal effects, atomic

phenomena and so on. Any real material subjected to stress/strain cycles dissipates energy. Generally the damping of viscoelastic materials is higher than that of conventional metals.

High damping is not the only beneficial property for good noise and vibration control. The additional effects of many other factors such as mass, stiffness, damage tolerance and so on have to be considered as well. For example, for a joint whose damping mechanism is Coulomb friction, the occurrence of maximum dry slip damping may sometimes develop serious corrosion in the interface regions. High damping is sometimes associated with low stiffness. So the trade-off between the requirements of low vibration level and strength must be carefully considered during the design stage of structures [12].

### 2.1.2 Measures of damping

Basically there are four measures of damping, the loss factor  $\eta$ , the quality factor  $Q$ , the damping ratio  $\zeta$ , and the imaginary part of the complex modulus. However, they are related to each other. The loss factor or damping ratio is used in measurements:

$$\eta = \frac{D}{2\pi W} = \frac{1}{Q} = 2\zeta = \frac{2C}{C_c} = \frac{E''}{E'} = \tan \phi . \quad (2-1)$$

Here  $D$  and  $W$  are the dissipated and total powers in one cycle of vibration,  $C$  and  $C_c$  are the damping coefficient and the critical damping,  $E'$  and  $E''$  are the real and imaginary parts of complex modulus.



### **2.1.3 Measurement methods**

Many references present reviews of damping measurements [7,11,18-20]. Generally, there are three sorts of experimental methods. Table 2.1 lists formulas used to calculate the loss factor with different methods.

#### **Decay rate method**

This method can be used to measure the damping of a single resonance mode or the average of a group of modes in a frequency band. The structure is given an excitation by a force in a given frequency band, the excitation is cut off, the output of the transducer is passed through a band pass filter and then the envelope of the decay is observed. The damping ratio can be calculated from the slope of the envelope of the log magnitude-time plot.

#### **Modal bandwidth method**

With the frequency response function (log magnitude-time plot or Nyquist diagram), the half-power point method is the most common form used to determine the damping. This method applies only to the determination of the damping of a single mode.

#### **Power balance method**

As mentioned in the previous section, the SEA method is based on the relationship between the input power and the dissipated power. So the loss factor can be determined by measuring the input power and the total energy of a modal subsystem.

Method	Loss factor
Decay Rate Method	$\eta = \frac{DR}{27.3f}$
Modal Bandwidth Method	$\eta = \frac{f_2 - f_1}{f_n}$
Power Balance Method	$\eta = \frac{W_{in}}{2\pi f W_{tot}}$ , where $W_{in} = \langle Fv \rangle$ , $W_{tot} = M \langle v^2 \rangle$

Table 2.1. Formulas used to calculate the loss factor by different methods.

## 2.2 Damping in Sandwich Structures

A sandwich structure consists of three elements: the face sheets, the core and the adhesive interface layers. The great advantage of sandwich structures is that optimal designs can be obtained for different applications by choosing different materials and geometric configurations of the face sheets and cores. By inserting a lightweight core between the two face sheets, the bending stiffness and strength are substantially increased compared with a single layer homogenous structure, without the addition of much weight. The viscoelastic core has a high inherent damping capacity. When the beam or plate undergoes flexural vibration, the damped core is constrained to shear. This shearing causes the flexural motion to be damped and energy to be dissipated. Additionally, the normal-to-shear coupling between the core and face sheets reduces the sound transmission. So in recent years, such structures have become used increasingly in transportation vehicles and other applications. Rao has described the applications of viscoelastic damping in automotive and aircraft structures [21]. Besides damping

treatments used in structures, sandwich glass has been used in automotive side and rear windows to reduce noise. Nakra has published a series of reviews on vibration control with viscoelastic materials [22-24]. Trovik has summarized the major uses of constrained layer damping treatments up to 1980 [25]. A thorough review of work in fiber-reinforced composite material damping research has been given by Chandra et al. [26].

### **2.2.1 Analytical models**

When a damping layer is attached to a vibrating structure, it dissipates energy by direct and shear strains. When a solid beam or plate is bending, the direct strain increases linearly with distance from the neutral axis. So unconstrained damping layers which dissipate energy mainly by direct strain are attached to the remote surfaces. On the other hand, the shear stress is the largest at the neutral axis and zero on the free surfaces. Therefore, constrained layers dissipate energy by shear stress. It has been shown that shear damping in viscoelastic materials is higher than in typical structural materials. And the constrained treatment has higher stiffness than unconstrained damping treatment. For these reasons sandwich composite structures are widely used.

Since the late 1950's many papers have been published on the vibration of sandwich structures. The Ross-Ungar-Kerwin model is one of the first theories which was developed for the damping in sandwich structures [28]-[31]. In Kerwin's initial study an analysis was presented for the bending wave propagation and damping in a simply supported three-layer beam [28]. One of the limitations of this analysis is that the bending stiffness of the top layer must be much smaller than that of the bottom layer. Ungar generalized the earlier study and derived an expression for the total loss factor of

sandwich beams in terms of the shear and structural parameters [30]. Based on such an expression, two important conclusions can be drawn. First, if the constraining layer is thinner than the viscoelastic damping layer, then the system damping has a maximum value when the shear parameter of the core has an optimal value in the intermediate range, as shown in Fig. 2.1, where  $X$  and  $Y$  are the shear and structural parameters, and  $\beta$  is the damping in the viscoelastic layer. Second, the loss factor has a maximum value when a three-layer sandwich structure is symmetric about the neutral axis.

Ruzicka summarized earlier research on viscoelastic shear damping mechanisms and presented structural damping design configurations, especially the so-called “cell-insert” idea [32,33]. He stated that the loss factor is independent of stress level for pure viscoelastic materials. He also analyzed the dynamic properties of viscoelastic-damped structures using a lumped-parameter model which resulted in a number of conclusions that agree with those obtained from the flexural wave analysis discussed in [28].

The limitations of Kerwin’s model have been avoided in Yu’s theory by using a variational approach [34]. Yu took into account inertia effects due to transverse, longitudinal and rotary motions, and considered the combined effects of three loss factors associated with the shear and direct stresses of the core and the direct stress in the face sheets. However, Yu only studied the flexural vibration of symmetric sandwich plates. Sadasiviah Rao and Nakra analyzed the damping in unsymmetric sandwich beams and plates and also included the inertia effects of transverse, longitudinal and rotary motion [35]. Inclusion of all the inertia effects in the flexural vibration analysis gives three families of modes in bending, extension and thickness-shear.

In extending the work of Kerwin, DiTaranto derived a sixth-order linear homogeneous differential equation for freely vibrating beams having arbitrary boundary conditions [36]-[38]. In this model, modes are completely uncoupled, which greatly simplifies the general forced vibration problem. However, the loss factor calculated using this equation does not depend on the boundary conditions. This conclusion obviously cannot be correct. Mead and Markus modified the theory and studied different boundary conditions in terms of the transverse displacement [39,40]. Using the separable of variables method, they derived the natural frequencies of sandwich beams and studied the effects of the shear and structural parameters on damping. The relationship is similar to the equation derived in [30]. Mead and Markus proved that the loss factor  $\eta$  is much less sensitive to the change of the shear parameter when the structural parameter  $Y$  is large, as shown in Fig. 2.2. They also showed that the maximum values of the damping are not very sensitive to the boundary condition, while different boundary conditions shift the frequency at which the maximum damping occurs.

In another study, Yan and Dowell initially included the effects of face sheet shear deformation, and longitudinal and rotary inertia [45]. However, from the set of equations obtained, the longitudinal and rotary terms are neglected by assuming the face sheets to be very stiff in shear. This procedure results in a fourth-order partial differential equation. Mead analyzed the damping in symmetric sandwich plates with one pair of opposite edges simply-supported [41]. He also studied the effect of different boundary conditions for the other edges and derived a sixth-order equation. Mead compared the difference between the fourth-order model derived by Yan and Dowell and the sixth-order model [42,44]. Based on Mead's sandwich plate model, Cupial and Nizioł included the shear

deformation of the face layers and rotary inertia and studied simply supported sandwich plates [47]. The damping calculated using the shear deformation model is somewhat lower than obtained from Mead's model. Wang and Chen studied damping in annular sandwich plates [48].

Since high damping is usually associated with relatively low stiffness and strength, it is a good idea to increase the stiffness using multi-span sandwich structures. Mead extended his previous work to periodically supported sandwich plates [43]. The basic idea is that at a particular frequency, all the displacement and forces at a point in one periodic element are identical to those at the corresponding point in the adjacent element, apart from a phase difference which is determined using an iterative technique. The frequency dependence of damping and the effects of support spacing and shear parameters on damping were also studied. Rao and He also analyzed damping in multi-span sandwich beams [49]. Rao and He derived two sixth-order differential equations to govern the transverse and longitudinal motions for each span using Hamilton's principle. The effects of thickness of the face sheets and core, and location of the intermediate support on the damping were studied for a two-span sandwich beam.

Rao derived a similar equation of motion using Hamilton's principle [51]. He presented an extensive study using computer programs to predict the loss factor and natural frequencies for different boundary conditions in terms of the shear parameter. Rao also analyzed flexural vibration of short unsymmetric sandwich beams including all the higher order effects, such as rotary inertia, bending, extensional and shear effects in all the layers [50]. He compared the loss factor and natural frequencies obtained using this new model and earlier models. For a beam where the core is thicker than the face sheets,

all the models predict identical results, although Rao's model includes the higher order effects. This means, for thick core beams, the effects of rotary inertia, extension and shear in all the layers are insignificant.

All the researchers introduced above, except Yu, have only considered the contribution of the damping in the viscoelastic core to the total damping in the entire structure by using the complex form of the shear modulus of the core. An advantage of the use of the complex shear modulus is that the differential equations only contain the even order terms. So they are easy to solve. These models are all based on the following assumptions: (a) the viscoelastic layer undergoes only shear deformation and hence the extensional energy of the core is neglected; (b) face sheets are elastic and isotropic and shear energy contributed in them is neglected; and (c) in the facings plane sections remain plane and normal to the deformed centerlines of the facings. In Reference [44] Mead conducted a comprehensive study on a comparison of these models.

Instead of only considering the damping in the core, Ungar and Kerwin also proposed the so-called modal strain energy (MSE) model in order to include the damping capacities of all the elements. In this model the damping of the material can be characterized by the ratio of the energy dissipated in each element to the energy stored in the material [31]. Based on the MSE method, Johnson and Kienholz produced a method to predict damping in structures with constrained viscoelastic layers by using finite element analysis [84]. Hwang and Gibson studied damping in composite materials and structures at both macromechanical and micromechanical levels using the MSE method [52-55]. They studied the contribution of interlaminar stresses to damping as well [56].

The frequency dependence property of viscoelastic damping was first presented by Lazan [57]. Ruzicka and Mead came to similar conclusions using lumped-parameter models [32,12]. Mead also studied the influence of the boundary conditions on the frequency dependence of the loss factor [40]. Nilsson used Hamilton's principle to derive a sixth-order differential equation which governs the bending of sandwich beams. He also studied the dynamic properties of sandwich structures [58,59]. The behavior of a sandwich structure in the low frequency region is determined by pure bending of the entire structure. In the middle frequency region, the rotation and shear deformation of the core become important. At high frequencies, the bending of the face sheets is dominant. Therefore, if the damping in the core is higher than that in the face sheets, then the overall damping has a maximum value in the middle frequency range. On the other hand, if the damping in the core is less than that in the face sheets, then the total damping has a minimum value in the middle frequency range. Figure 2.3 shows the calculated total loss factors for three different cases, where the loss factor in the core  $\eta_2$  is set to be 2 % and the loss factor in the face sheets  $\eta_1$  varies.

The theoretical models discussed so far can be categorized into two classes, fourth-order models and sixth-order models. Models derived by Mindlin's theory and Timoshenko's theory both lead to a fourth-order differential equation. Mead [42,44], Rao [50] and Nilsson [59] all show that sixth-order models lead to more accurate results on the dynamics and damping than fourth-order models. Nilsson states that due to the frequency dependence of sandwich structure properties, solutions of the fourth-order differential equation agree well with measurements at low frequency. However, as the frequency increases, the calculated results disagree strongly with measurements.



Besides the three-layer sandwich structures, multi-layer sandwich structures are also widely studied [60-67]. Grootenhuis showed that the four-layer and five-layer beams have wider high damping range in terms of the damping layer shear modulus than three-layer sandwich beams, as shown in Fig. 2.4, where  $E$  and  $G$  denote the Young's modulus and shear modulus, and  $h$  is thickness [62]. Asnani and Nakra studied the damping characteristics of symmetric multi-layer beams with identical viscoelastic and elastic layers alternatively arranged [64]. They provided three design criteria and analyzed the effects of the shear parameter and layer thicknesses on the total damping. Alam and Asnani extended the previous work to multilayer structures with orthotropic damping layers where each damping layer is constrained between two elastic layers [65-67]. They considered shear strain in all the layers. But their result does not satisfy continuity of the shear stress across the interfaces. Bhimaraddi proposed a refined shear deformation theory in which the shear stresses are continuous across the interfaces [68]. Rao and He studied several different multilayer configurations using the numerical analysis [69]. Two more fiber reinforced layers are added on the two free surfaces. The total damping can be improved by changing the fiber orientation.

Among the multi-layer sandwich structures, special attention has been given to spaced sandwich structures. In some sandwich panels, a spacer is inserted between the base plate and the viscoelastic damping layer to magnify the shear strain and enhance the damping. Since the viscoelastic damping layer is separated from the neutral axis of the entire structure due to the spacer, the direct stress is increased. To make this configuration effective, the shear stiffness of the spacer must be much greater than that of the damping layer so that the shear stress in the damping layer also increases. Ross,

Ungar and Kerwin present this idea first in [29], as shown in Fig. 2.5. Nakra and Grootenhuis derived the equations of motion using Hamilton's principle [63]. The Two face sheets are assumed to be perfectly elastic, and the damping layer and spacer are viscoelastic. Compared with three layer sandwich beams and plates, multi-layer structures have wider high damping range in terms of the core shear modulus [62,63]. Van Vuure et al. applied the modal strain energy method to model such structures and the finite element method to calculate the loss factor in each layer [60]. They also studied the effects of spacer position.

Since many complex structures have joints, the joint damping is also an interesting phenomenon. Joint fasteners for sandwich composite structures can be bolts, rivets, or adhesive layers. He and Rao analyzed the damping in adhesively bonded double-strap joints [70]. The effects of the shear modulus of the damping layer and structural parameters, such as the damping and constraining layer thicknesses, on the modal loss factor are studied. If the viscoelastic damping layer is much softer than the constraining layer, the total loss factor varies little with the shear modulus of the damping layer. In Fig. 2.6 the normalized shear modulus is defined as the ratio of the core shear modulus to the face sheet Young's modulus.

In general, the damping of bonded structures tends to be lower than that of structures with bolted and riveted joints [12]. Nanda and Behera conducted a theoretical analysis and experiments for the damping in bolted laminated structures [71]. The damping in such structures depends on many factors such as the diameter of the bolts, tightening torque on the bolts, number of layers, and so on.

Marsh and Hale presented a different damping configuration, which consists of an internal shear damping treatment [72]. Such structures are hollow with viscoelastic damping materials bonded inside the structures. This is very similar to the “cell-insert” concept presented by Ruzicka [32,33]. Marsh and Hale analyzed the effects of geometry and mechanical parameters on the damping in such structures. Figure 2.7 illustrates the internal damping treatment idea.

### **2.2.2 Damping and damage**

Damage is another mechanism which causes increased damping. Prasad and Carlsson analyzed debonding and crack growth in foam core sandwich beams using the finite element method [73]. Experiments were carried out with cantilever beams and shear specimens [74]. Luo and Hanagus studied the dynamics of delaminated beams by using a piecewise-linear spring model to simulate the behavior of delaminated layers [75]. Delamination introduces friction in the unbounded region of the interface. And the damping increases with the size of the delamination. Meanwhile, increased damping leads to lower natural frequencies. This effect is significant in the high frequency range [76].

Delamination affects the stiffness of sandwich beams as well. For beams with delamination, the bending stiffness is reduced substantially. If there is delamination on both sides of the beam, the bending stiffness is reduced more than if there is delamination only on one side. This conclusion is the same as that resulting from Frostig’s model which is based on high-order elastic theory [77].

It is worth noticing that high damping is not the only criterion for noise and vibration control. The overall effects of many factors such as mass, stiffness, damage tolerance and so on have to be considered as well. High damping is usually associated with relatively low stiffness. So the trade-off between the requirement for low vibration levels and strength and stiffness must be analyzed during the design stage. Some criteria for assessing the damping effectiveness can be found in [78].

### **2.2.3 Finite element models**

The complex eigenvalue method and the direct frequency response method are two conventional methods that can be used to evaluate damping. Lu et al. conducted a series of research on vibration of damped sandwich structures using the direct frequency response method [79-83]. However, these two conventional methods are both computationally expensive. In recent years the modal strain energy method and the Golla-Hughes-McTavish (GHM) method have come into more common use.

As discussed in the first section, the modal strain energy method was proposed by Ungar and Kerwin and developed by Johnson using finite element analysis. Although this is an approximate technique for the prediction of damping, the advantage is that only the response of undamped normal modes needs to be calculated and the energy distributions are of direct use to the designer in deciding where to locate damping layers [84]. Veley and Rao studied the effect of the thicknesses of all the layers, and the amount and the location of the damping treatment [85]. They claim that an increase in the constrained layer thickness increases the loss factor. Although an increase in the viscoelastic layer thickness increases the loss factor of the first mode, it decreases the loss factor of higher

modes. Zambrano et al. studied the accuracy of this method for the estimation of the response of structures using viscoelastic dampers [86]. Plagianakos and Saravanos presented a new finite element model for sandwich beams involving quadratic and cubic terms for approximation of the in-plane displacement in each layer [87]. The damping is calculated using the modal strain energy method. The effects of ply orientation, thickness and boundary conditions on the damping are analyzed. Shorter used a one-dimensional finite-element mesh to describe the low order cross-sectional deformation of laminates and the modal strain energy method to calculate the damping [88]. This finite element model showed that below a particular frequency only longitudinal, shear and bending waves are observed, while at high frequencies additional propagating waves appear which involve the out-of-phase flexural motion of the face sheets, which is called symmetric motion or dilatational motion by other researchers [131,132,140].

The GHM method is a technique for deriving a viscoelastic finite element from the commonly-used elastic finite element and for measurements of both frequency domain and time domain material behavior [89]. Based on this model, Wang et al. analyzed the vibration characteristics of sandwich plates incorporated with the Galerkin method and conducted experiments with simply supported and clamped plates [90]. The GHM method can successfully predict the frequency dependence of the complex shear modulus in the core.

Chen et al. presented an order-reduction-iteration approach to predict the damping in sandwich structures [91]. Such a method consists of two steps, the first-order asymptotic solution of the nonlinear real eigenequation and the order-reduction-iteration of the complex eigenequation.

Nayfeh analyzed five-layered sandwich beams using finite element implementation of the modal strain energy model [92]. He studied different boundary conditions and partially covered sandwich beams, the effects of the coupling factor, and ratio between the stiffnesses of the face sheets and the core.

#### **2.2.4 Statistical energy analysis method**

Finite element models are generally only efficient for problems at low and middle frequencies. Since the size of elements must be considerably smaller than the minimum wavelength, the required number of elements increases dramatically with frequency range of interest, as well as the geometry and complexity of structure. The statistical energy analysis (SEA) or power balance method is attractive at high frequencies where a deterministic analysis of all resonant modes of vibration is not practical. In SEA model, a complex structure is virtually divided into coupled subsystems. Energy flows from one subsystem to others. Based on the assumption of power balance of these subsystems, the averaged behavior of the whole structure can be predicted. Because SEA calculates the spatial and frequency averaged response, the SEA model for a complex structure could be quite simple. Modal density, internal loss factor for each subsystem, and coupling loss factors between the subsystems are the basic SEA parameters.

Since the SEA model is widely used in sound transmission research and damping is related to the sound transmission properties, especially at the critical frequency, SEA is also used in damping estimations. Although this method cannot be applied for measurement of damping in an individual mode of vibration, it is very practical for the estimation of damping in a particular frequency band. Actually this feature of SEA is

very experimentally useful, because the uncertainty and severe modal overlap of the frequency response functions of sandwich structures at high frequencies make it is difficult to determine the loss factor for an individual mode.

Lyon has presented the concept of SEA in the 1960's and used this approach to formulate a model for the prediction of damping [13,93]. Bloss and Rao measured the damping in laminated glass for vehicle side windows using the SEA method [94]. The damping in a particular frequency band predicted by SEA is based on the ratio of the dissipated energy to the total energy measured in this frequency band. And under steady state condition, the dissipated energy is equal to the input energy that can be calculated using the input force and modal density. The total energy of a subsystem is the product of mass and the spatial average of mean square value of velocity.

As mentioned before, modal density is one of the basic SEA parameters. The first theoretical study of the modal density of sandwich shell with an isotropic core was conducted by Wilkinson based on a fourth-order equation of motion [96]. Erickson showed that for typical honeycomb structures the effect of rotary inertia and bending stiffness of the face sheet can be neglected, but the shear flexibility of the core is important [96]. So he modified the theoretical expression for the modal density of honeycomb plates. Clarkson and Ranky derived a new theoretical expression based on the sixth-order equation of motion [97]. This new expression gives a good estimation of the modal density of plain honeycomb plates and is independent of the shape of the structure. Renji et al. derived an expression to evaluate the modal density of a honeycomb sandwich panel with orthotropic face sheets based on a fourth-order governing differential equation [105].

As for experimental methods to determine the modal density of panels and beams, Lyon and DeJong have described some basic approaches [93]. The mode count is a straightforward method, which identifies and counts the number of resonance peaks from the frequency response function. At high frequencies, severe modal overlap makes the modes are indistinct. Clarkson and Pope developed an experimental technique to determine the modal density of a lightly damped structure by measuring the spatial average of the driving point mobility  $Y(i\omega) = V(i\omega)/F(i\omega)$ , where  $V$  and  $F$  are the Fourier transforms of the velocity and force signals [97,98]. Theoretically the real part of the driving point mobility must be positive. Several papers were published later on to improve this technique. Ranky and Clarkson demonstrated that the one-third octave bands are too wide. A more suitable bandwidth is 100 Hz for metal plates, but 500 Hz for honeycomb plates because the modal density of sandwich structures is relatively low [99]. Because the measured velocity at the driving point include a non-propagating (near field) component which is not related to the energy input, the velocity of the driving point should not be included in the calculation of the spatial average velocity. Clarkson and Ranky also studied the effect of discontinuities in honeycomb plates, such as circular cut-outs, added mass and added stiffeners [100]. In order to solve the presence of negative values in the real part of driving point mobility, Brown presented a three-channel technique by measuring one more signal  $s(t)$  which is the original signal to drive the power amplifier [101]. The driving point mobility is then calculated as  $Y(i\omega) = G_{sv}(i\omega)/G_{sf}(i\omega)$ , where  $G$  is the cross-spectrum. Brown and Norton suggested a method to correct the error in mobility calculation introduced by the added mass between the transducer and the structure [102]. Keswick and Norton studied three different



excitation arrangement ways of an impedance head and used the spectral mass method to correct the measured mobility [103]. Hakansson and Carlsson presented a similar correction method using a dual-channel FFT analyzer with an unloaded impedance head [104]. Applying Brown and Norton's correction method, Renji measured the modal density of foam-filled honeycomb sandwich panels using an improved input mobility method by including both the real and imaginary parts [106]. Beyond a particular frequency, the measured modal density decreases with frequency although the theoretical results still increase. Renji explains this is because the vibration of the honeycomb cells that occurs at high frequencies.

Based on the experimental techniques introduced above, the loss factors of sandwich structures are then also measured [97,99,107]. It is important to notice that the frequency average loss factor in a frequency band is not the arithmetic average of individual modal loss factors.

If measurements are made in air, the measured loss factor is basically the total effect of the internal and acoustic radiation loss factors. Since the coincidence frequency of a sandwich structure is generally lower than thin metal plates due to both the bending and shear waves propagating in it, the radiation loss factor could be very significant in the frequency bands of interest. Clarkson and Brown have shown that the use of the loss factor measured in air in SEA model can lead to large errors in the estimated response, because for honeycomb sandwich plates, the acoustic damping is the major component of the total damping [16,108].

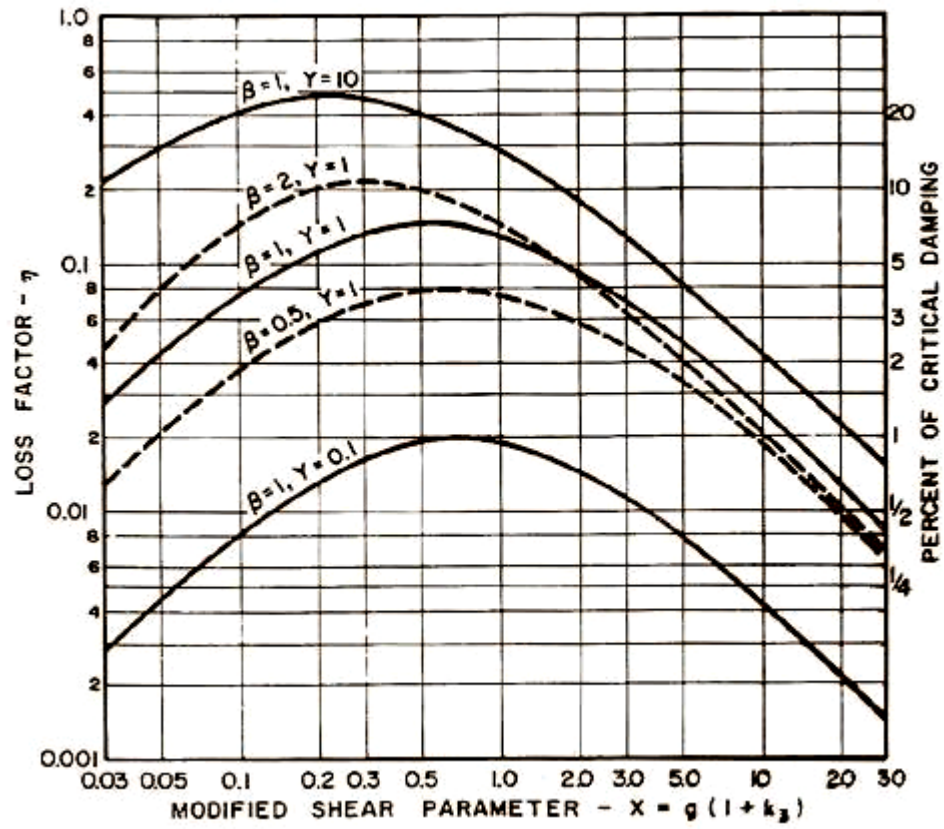


Figure 2.1. The effect of the shear modulus on the total damping in a sandwich structure.

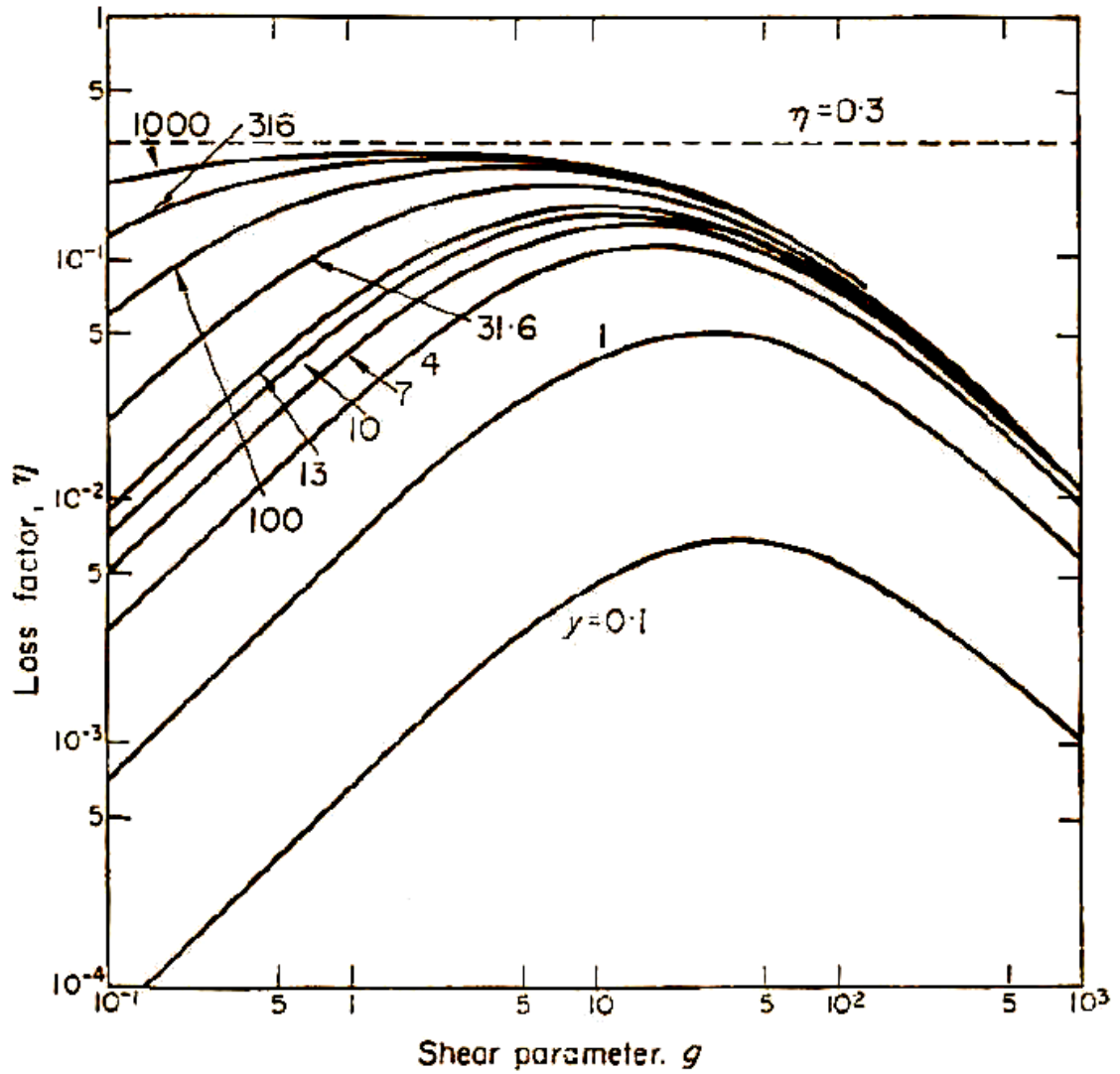


Figure 2.2. The effects of the shear and structural parameters on the system loss factor.

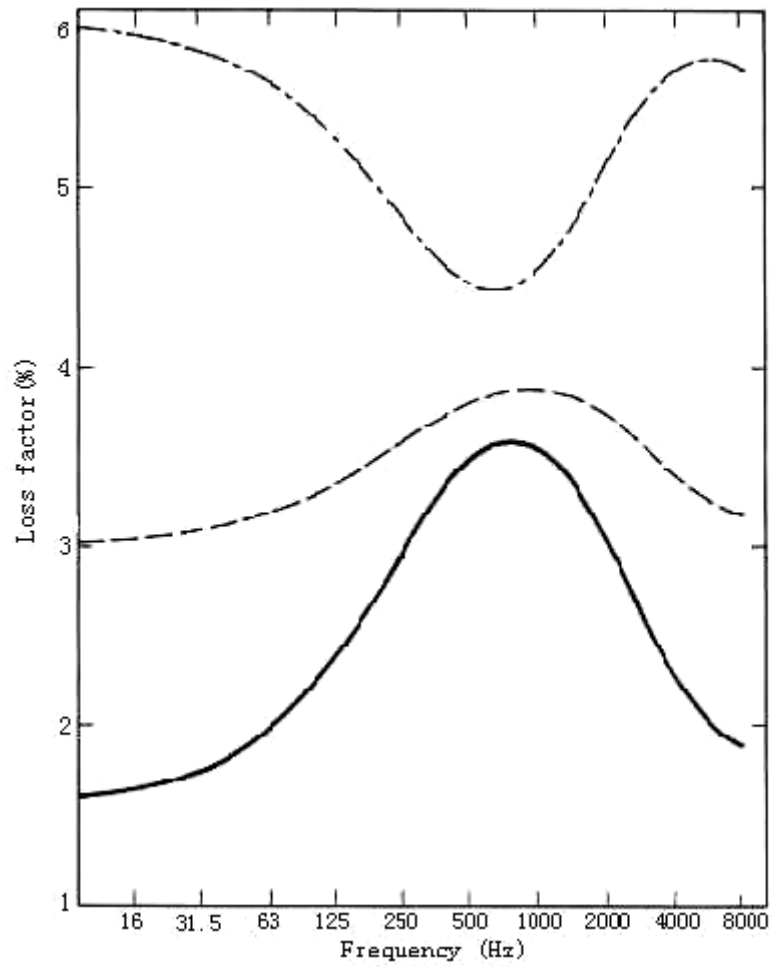


Figure 2.3. The frequency dependence of the damping in sandwich structures. Solid line,  $\eta_1 = 1.5 \%$ ,  $\eta_2 = 2 \%$ ; dashed line,  $\eta_1 = 3 \%$ ,  $\eta_2 = 2 \%$ ; dotted line,  $\eta_1 = 6 \%$ ,  $\eta_2 = 2 \%$ .

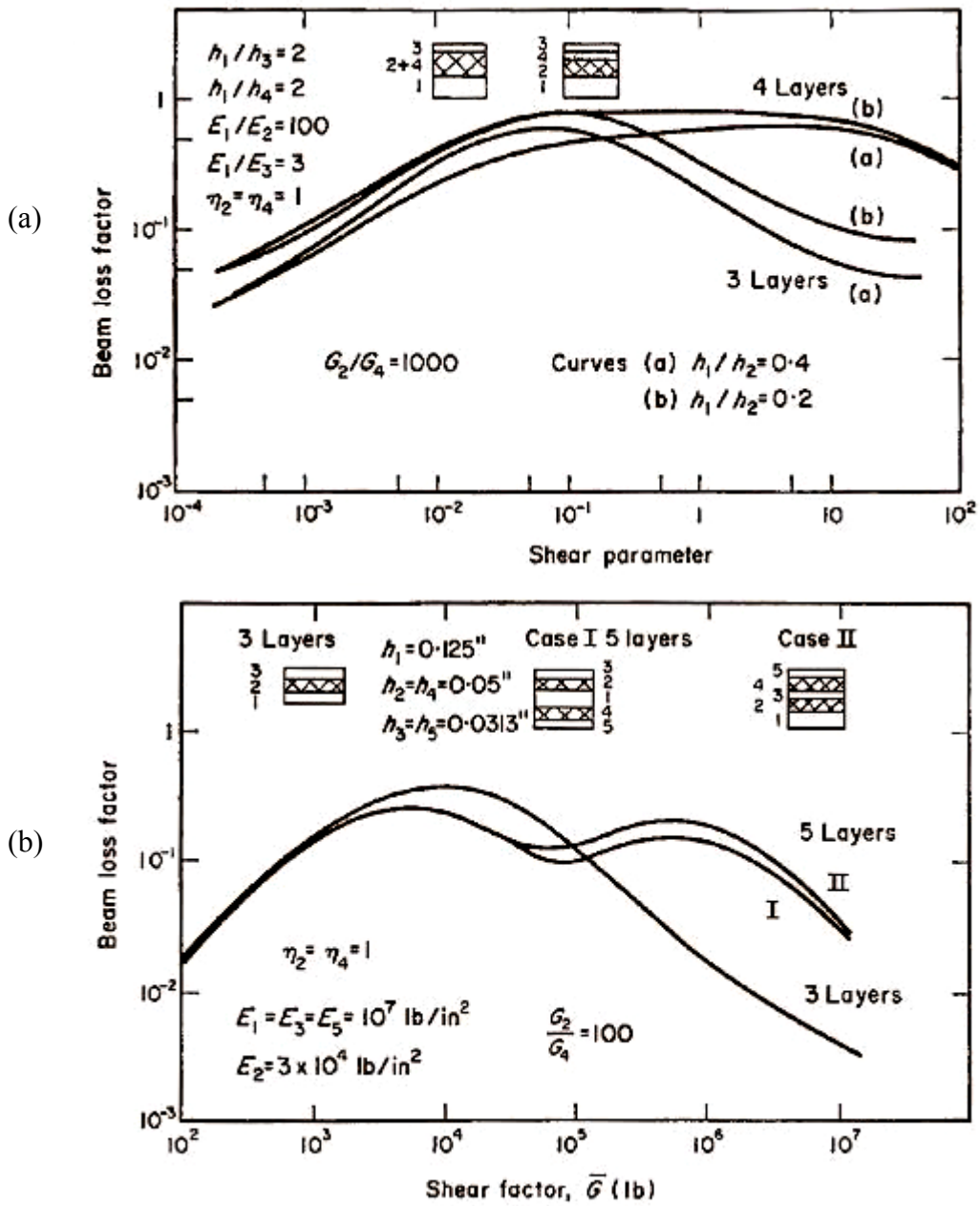


Figure 2.4. The shear parameter effect on the total damping in multi-layer sandwich beams.

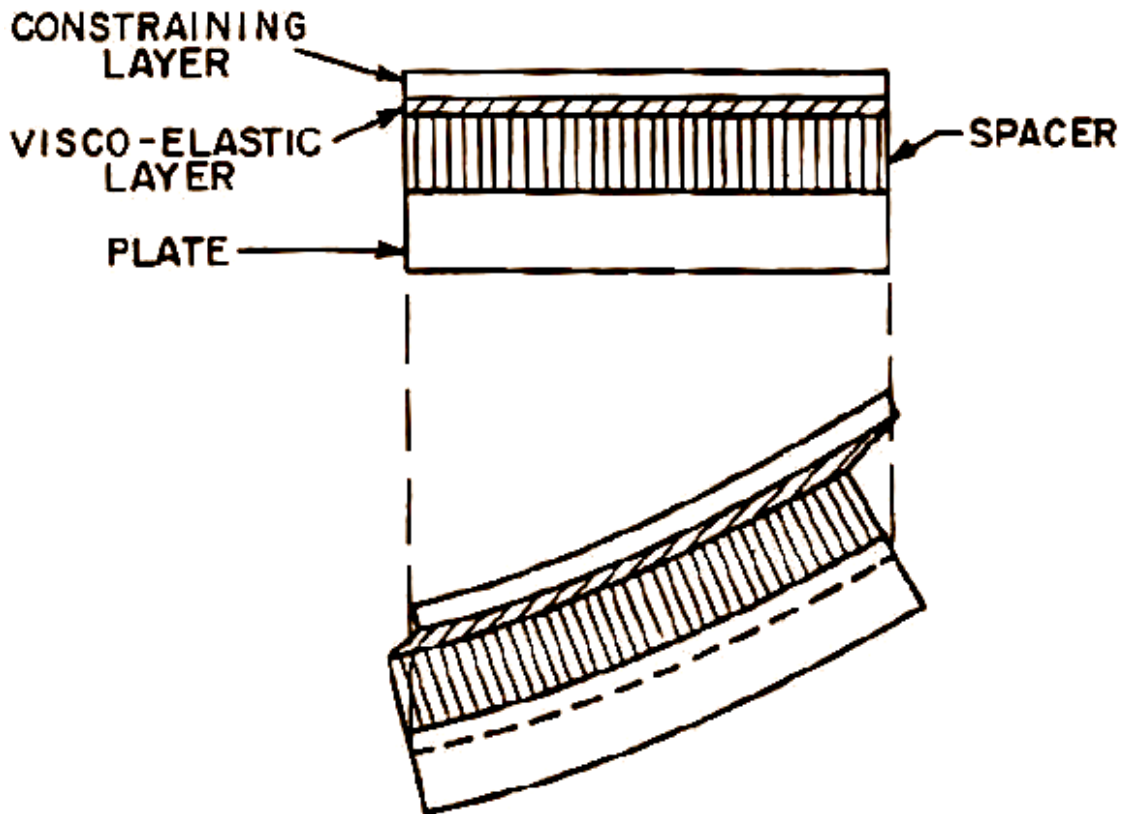


Figure 2.5. A sandwich beam with a spacer beneath the damping layer.

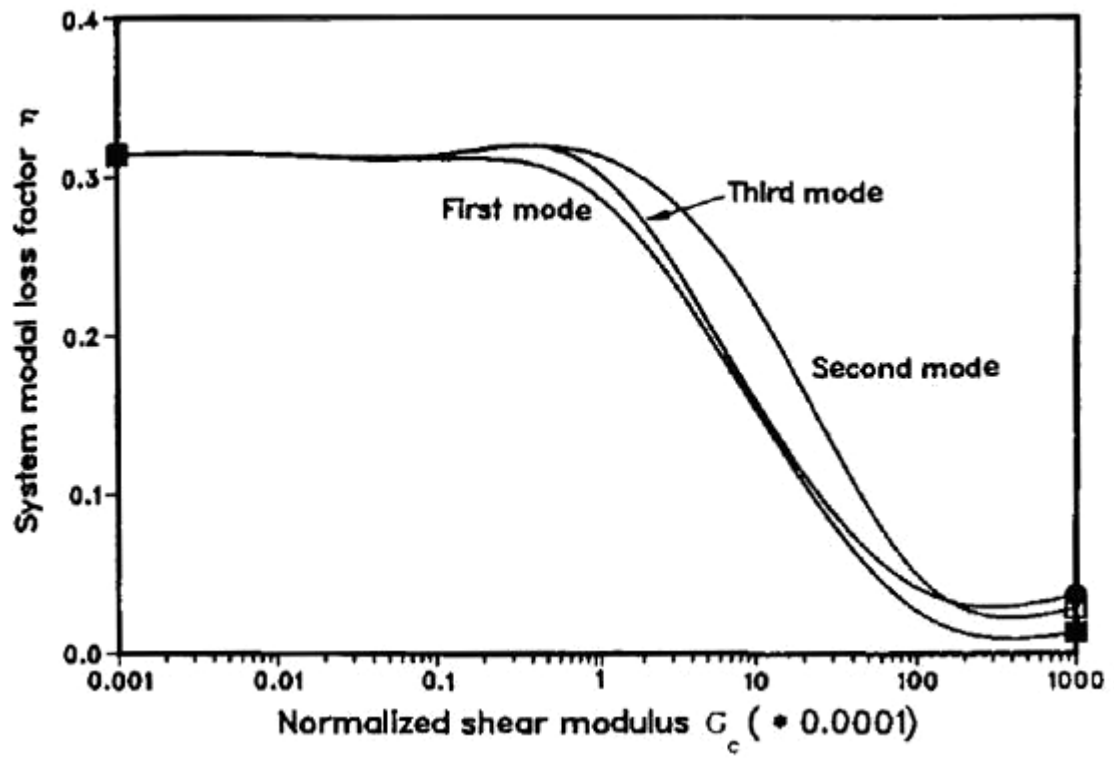


Figure 2.6. Variation of modal loss factor with the normalized shear modulus.

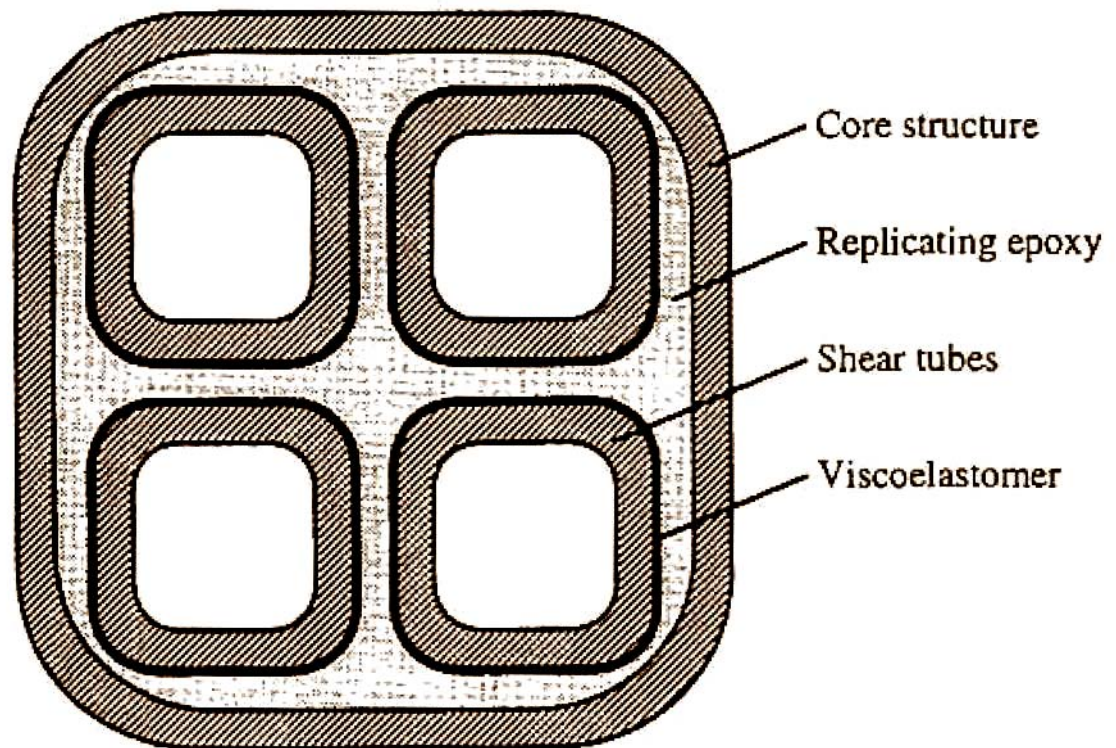


Figure 2.7. Internal damping treatment.



### CHAPTER 3 ANALYSIS OF DAMPING IN SANDWICH MATERIALS

In the recent research, cores made of either honeycomb or solid viscoelastic material have been studied [58,59,105-107]. The core in this particular study was made of paper honeycomb filled with polyurethane (PUR) foam. The honeycomb material is expected to enhance the stiffness of the entire structure, while the foam improves the damping. Jung and Aref reported that sandwich structures with combined honeycomb-foam cores have higher damping than those with individual honeycomb or solid viscoelastic cores [4]. However, Jung and Aref used a static hysteretic damping model, so damping ratios are independent of frequency. This conclusion is obviously not valid. In this paper the frequency dependence of damping in sandwich beams with foam-filled honeycomb cores is analyzed, and the effects of thickness of the face sheets and core, and delamination on damping are studied. Most of the earlier models ignore the bending and extensional effects in the core. However, this assumption is only valid for soft thin cores. In this paper both the bending and shear effects are considered. And the shear stresses are continuous across the face sheet-core interfaces.

The sixth-order equations of motion for sandwich beams are derived using Hamilton's principle. The wavenumber and speed of flexural wave propagating in sandwich beams are thus studied. The effect of thickness and delamination on damping in sandwich structures is analyzed. Measurements on honeycomb-foam sandwich beams

with different configurations and thicknesses have been performed and the results compared with the theoretical predictions.

### 3.1 Equation of Motion

First of all, the bending stiffness of a symmetric sandwich beam can be expressed as

$$\begin{aligned}
 D &= \int E z^2 dA = \int_{-t_f - \frac{t_c}{2}}^{-\frac{t_c}{2}} E_f z^2 b dz + \int_{-\frac{t_c}{2}}^{\frac{t_c}{2}} E_c z^2 b dz + \int_{\frac{t_c}{2}}^{t_f + \frac{t_c}{2}} E_f z^2 b dz \\
 &= 2 \int_{\frac{t_c}{2}}^{t_f + \frac{t_c}{2}} E_f z^2 b dz + 2 \int_0^{\frac{t_c}{2}} E_c z^2 b dz \\
 &= b \cdot \left[ \frac{E_f t_f^3}{6} + \frac{E_f t_f d^2}{2} + \frac{E_c t_c^3}{12} \right] = 2D_f + D_0 + D_c,
 \end{aligned} \tag{3-1}$$

where  $b$  is the width of the beam,  $t_f$  and  $t_c$  are the thicknesses of the face sheet and core,  $E_f$  and  $E_c$  are the Young's moduli of the face sheet and core, and  $d = t_f + t_c$ .  $D_f$  is the bending stiffness of a face sheet about its own neutral axis,  $D_0$  is the stiffness of the face sheets associated with bending about the neutral axis of the entire sandwich, and  $D_c$  is the stiffness of the core. Figure 3.1 shows the beam dimensions and layer configuration.

Considering the shear deformation, the slope of the deflection curve is not equal to the rotation of the beam cross section. According to Timoshenko's beam model, the total curvature due to both the bending and shear is

$$\frac{d^2 w}{dx^2} = \frac{d\beta}{dx} + \frac{d\gamma}{dx}, \tag{3-2}$$

where  $w$  is the total flexural displacement,  $\beta$  and  $\gamma$  are the bending and shear deformation.

Next, Hamilton Principle will be used to derive the equations of motion and natural boundary conditions for sandwich beams.

The total kinetic energy due to translation and rotation has the form

$$T(t) = \frac{1}{2} \int_0^L m(x) \left( \frac{\partial w(x,t)}{\partial t} \right)^2 dx + \frac{1}{2} \int_0^L J(x) \left( \frac{\partial \beta(x,t)}{\partial t} \right)^2 dx, \quad (3-3)$$

where  $L$  is the total length of the beam,  $m(x)$  is mass per unit length, and  $J(x)$  is mass moment of inertia per unit length. And for a symmetric sandwich beam, we have

$$m(x) = b(2\rho_f t_f + \rho_c t_c),$$

$$\text{and } J(x) = \int_{-\frac{t_c}{2}-t_f}^{\frac{t_c}{2}+t_f} \rho(z) z^2 dA = b \left( \frac{\rho_f t_f^3}{12} + \frac{\rho_f t_f d^2}{2} + \frac{\rho_c t_c^3}{12} \right).$$

The total potential energy contains three parts. The potential energy due to pure bending of the entire beams, under the bending moment  $M(x,t)$ , is

$$U_1 = \frac{1}{2} \int_0^L M(x,t) \frac{\partial \beta(x,t)}{\partial x} dx = \frac{1}{2} \int_0^L EI \left[ \frac{\partial \beta(x,t)}{\partial x} \right]^2 dx. \quad (3-4a)$$

The potential energy due to shear deformation in the core, under the shear force  $V(x,t)$ , is

$$U_2 = \frac{1}{2} \int_0^L V(x,t) \gamma(x,t) dx = \frac{1}{2} \int_0^L k' G b t_c \gamma^2(x,t) dx, \quad (3-4b)$$

where  $k'$  is the shear coefficient which is 5/6 for a beam with rectangular cross-section,  $G$  is the shear modulus of the core. The third part of the potential energy is due to additional bending deformation in the two face sheets caused by the shear deformation in the core

$$U_3 = \int_0^L D_f \left( \frac{\partial \gamma}{\partial x} \right)^2 dx. \quad (3-4c)$$

Then the total potential energy of a sandwich beam can be obtained by combining the three expressions above. By also including the external distributed load  $p(x)$  as shown in Fig. 3.1, we have

$$W = -\frac{1}{2} \int_0^L \left[ D \left( \frac{\partial \beta}{\partial x} \right)^2 + 2D_f \left( \frac{\partial \beta}{\partial x} \right)^2 + k' G b t_c \gamma^2 \right] dx + \int_0^L p(x) w(x) dx. \quad (3-5)$$

Applying Hamilton's Principle, we let

$$\delta \int_{t_1}^{t_2} (T + W) dt = 0. \quad (3-6)$$

From Eq. (3-3) we have

$$\begin{aligned} \delta \int_{t_1}^{t_2} T dt &= \int_{t_1}^{t_2} \int_0^L m \frac{\partial w}{\partial t} \delta \left( \frac{\partial w}{\partial t} \right) dx dt + \int_{t_1}^{t_2} \int_0^L m \frac{\partial \beta}{\partial t} \delta \left( \frac{\partial \beta}{\partial t} \right) dx dt \\ &= - \int_{t_1}^{t_2} \int_0^L \left( m \frac{\partial^2 w}{\partial t^2} \delta w + J \frac{\partial^2 \beta}{\partial t^2} \delta \beta \right) dx dt. \end{aligned} \quad (3-7)$$

After some calculations, the variation of the second term in  $W$  is

$$\begin{aligned} & - \int_{t_1}^{t_2} \int_0^L 2D_f \left( \frac{\partial^2 w}{\partial x^2} - \frac{\partial \beta}{\partial x} \right) \left[ \frac{\partial^2}{\partial x^2} (\delta w) - \frac{\partial}{\partial x} (\delta \beta) \right] dx dt \\ &= \int_{t_1}^{t_2} \int_0^L 2D_f \left[ \delta w \left( \frac{\partial^3 \beta}{\partial x^3} - \frac{\partial^4 w}{\partial x^4} \right) + \delta \beta \left( \frac{\partial^2 \beta}{\partial x^2} - \frac{\partial^3 w}{\partial x^3} \right) \right] dx dt + \int_{t_1}^{t_2} 2D_f \left( \frac{\partial^3 w}{\partial x^3} - \frac{\partial^4 \beta}{\partial x^4} \right) \delta w \Big|_0^L dt \\ & \quad + \int_{t_1}^{t_2} 2D_f \left( \frac{\partial^2 w}{\partial x^2} - \frac{\partial \beta}{\partial x} \right) \delta \beta \Big|_0^L dt + \int_{t_1}^{t_2} 2D_f \left( \frac{\partial \beta}{\partial x} - \frac{\partial^2 w}{\partial x^2} \right) \frac{\partial}{\partial x} (\delta w) \Big|_0^L dt. \end{aligned} \quad (3-8)$$

Similarly, the variation of the third term in  $W$  is

$$\begin{aligned}
& -\int_{t_1}^{t_2} \int_0^L k' G dt_c \left( \frac{\partial w}{\partial x} - \beta \right) \left[ \frac{\partial}{\partial x} (\delta w) - \delta \beta \right] dx dt \\
& = -\int_{t_1}^{t_2} \int_0^L k' G dt_c \left[ \frac{\partial w}{\partial x} \frac{\partial}{\partial x} (\delta w) - \frac{\partial w}{\partial x} \delta \beta - \beta \frac{\partial}{\partial x} (\delta w) + \beta \delta \beta \right] dx dt \\
& = -\int_{t_1}^{t_2} \left( k' G dt_c \frac{\partial w}{\partial x} \delta w \Big|_0^L - \int_0^L k' G dt_c \delta w \frac{\partial^2 w}{\partial x^2} dx \right) dt + \int_{t_1}^{t_2} \int_0^L k' G dt_c \frac{\partial w}{\partial x} \delta \beta dx dt \\
& \quad + \int_{t_1}^{t_2} \left( k' G dt_c \beta \delta w \Big|_0^L - \int_0^L k' G dt_c \delta w \frac{\partial \beta}{\partial x} dx \right) dt - \int_{t_1}^{t_2} \int_0^L k' G dt_c \beta \delta \beta dx dt.
\end{aligned} \tag{3-9}$$

Then

$$\begin{aligned}
\delta \int_{t_1}^{t_2} W dt & = -\int_{t_1}^{t_2} \int_0^L D \frac{\partial \beta}{\partial x} \frac{\partial}{\partial x} \delta \beta dx dt + (3-8) + (3-9) + \int_{t_1}^{t_2} \int_0^L p(x) \delta w dx dt \\
& = -\int_{t_1}^{t_2} \left( D \frac{\partial \beta}{\partial x} \delta \beta \Big|_0^L - \int_0^L D \frac{\partial^2 \beta}{\partial x^2} \delta \beta dx \right) dt + (3-8) + (3-9) + \int_{t_1}^{t_2} \int_0^L p(x) \delta w dx dt.
\end{aligned} \tag{3-10}$$

Substitute (3-7) and (3-10) into (3-6), we have

$$\begin{aligned}
& \int_{t_1}^{t_2} \int_0^L \delta w \left[ -m \frac{\partial^2 w}{\partial t^2} + k' G dt_c \left( \frac{\partial^2 w}{\partial x^2} - \frac{\partial \beta}{\partial x} \right) - 2D_f \left( \frac{\partial^4 w}{\partial x^4} - \frac{\partial^3 \beta}{\partial x^3} \right) + p \right] dx dt \\
& + \int_{t_1}^{t_2} \int_0^L \delta \beta \left[ -J \frac{\partial^2 \beta}{\partial t^2} + D \frac{\partial^2 \beta}{\partial x^2} + k' G dt_c \left( \frac{\partial w}{\partial x} - \beta \right) - 2D_f \left( \frac{\partial^3 w}{\partial x^3} - \frac{\partial^2 \beta}{\partial x^2} \right) \right] dx dt \\
& + \int_{t_1}^{t_2} \delta w \left[ -k' G dt_c \left( \frac{\partial w}{\partial x} - \beta \right) + 2D_f \left( \frac{\partial^3 w}{\partial x^3} - \frac{\partial^2 \beta}{\partial x^2} \right) \right]_0^L dt + \int_{t_1}^{t_2} \delta \beta \left[ -D \frac{\partial \beta}{\partial x} + 2D_f \left( \frac{\partial^2 w}{\partial x^2} - \frac{\partial \beta}{\partial x} \right) \right]_0^L dt \\
& + \int_{t_1}^{t_2} 2D_f \delta \left( \frac{\partial w}{\partial x} \right) \left( \frac{\partial \beta}{\partial x} - \frac{\partial^2 w}{\partial x^2} \right)_0^L dt = 0.
\end{aligned} \tag{3-11}$$

Therefore, we have the governing equations:

$$-m \frac{\partial^2 w}{\partial t^2} + k' G dt_c \left( \frac{\partial^2 w}{\partial x^2} - \frac{\partial \beta}{\partial x} \right) - 2D_f \left( \frac{\partial^4 w}{\partial x^4} - \frac{\partial^3 \beta}{\partial x^3} \right) + p = 0. \tag{3-12}$$

$$-J \frac{\partial^2 \beta}{\partial t^2} + D \frac{\partial^2 \beta}{\partial x^2} + k' G dt_c \left( \frac{\partial w}{\partial x} - \beta \right) - 2D_f \left( \frac{\partial^3 w}{\partial x^3} - \frac{\partial^2 \beta}{\partial x^2} \right) = 0. \tag{3-13}$$

Also, since  $\delta w$ ,  $\delta\beta$  and  $\delta\left(\frac{\partial w}{\partial x}\right)$  are arbitrary, the last three integrals in (3-11) must equal to zero to get the natural boundary conditions. At  $x = 0, L$ , we have

$$k'Gdt_c\left(\frac{\partial w}{\partial x} - \beta\right) = 2D_f\left(\frac{\partial^3 w}{\partial x^3} - \frac{\partial^2 \beta}{\partial x^2}\right), \quad \text{or } w = 0, \quad (3-14)$$

$$D\frac{\partial \beta}{\partial x} = 2D_f\left(\frac{\partial^2 w}{\partial x^2} - \frac{\partial \beta}{\partial x}\right), \quad \text{or } \beta = 0, \quad (3-15)$$

$$\frac{\partial \beta}{\partial x} = \frac{\partial^2 w}{\partial x^2}, \quad \text{or } \frac{\partial w}{\partial x} = 0, \quad (3-16)$$

Assume harmonic solutions  $w = Ae^{j(\omega t - kx)}$  and  $\beta = Be^{j(\omega t - kx)}$ . Substitute them into Eqs. (3-12) and (3-13), then

$$\begin{pmatrix} m\omega^2 - k'Gbt_c k^2 - 2D_f k^4 & j(k'Gbt_c k + 2D_f k^3) \\ -j(k'Gbt_c k + 2D_f k^3) & J\omega^2 - Dk^2 - k'Gbt_c - 2D_f k^2 \end{pmatrix} \begin{Bmatrix} w \\ \beta \end{Bmatrix} = \begin{Bmatrix} p \\ 0 \end{Bmatrix}. \quad (3-17)$$

Since  $w$  and  $\beta$  can be arbitrary, the coefficient matrix must be singular. Therefore, by setting the determinant of the coefficient matrix to zero, we have a sixth-order equation for the wavenumber  $k$  and speed of wave in sandwich beam  $c_b$ :

$$\begin{aligned} & 2D_f Dk^6 + (k'GAD - 2D_f J\omega^2)k^4 \\ & - (mD\omega^2 + 2mD_f \omega^2 + k'GAJ\omega^2)k^2 + (mJ\omega^4 - mk'GA\omega^2) = 0. \end{aligned} \quad (3-18)$$

$$\begin{aligned} & m(J\omega^2 - k'GA)\omega^2 c_b^6 - m(D + 2D_f + k'GAJ)\omega^6 c_b^4 \\ & + (k'GAD - 2D_f J\omega^2)\omega^4 c_b^2 + 2D_f D\omega^6 = 0. \end{aligned} \quad (3-19)$$

### 3.2 Effects of Thickness

In the Ross-Ungar-Kerwin model [7,11,30], the loss factor is given by the following formula

$$\eta = \frac{\beta Y X}{1 + (2 + Y)X + (1 + Y)(1 + \beta^2)X^2}, \quad (3-20)$$

where

$$X = \frac{Gb}{k^2 t_c} S, \quad \frac{1}{Y} = \frac{E_t I_t + E_b I_b}{d^2} S, \quad S = \frac{1}{E_t A_t} + \frac{1}{E_b A_b}, \quad (3-21)$$

$\beta$  is the loss factor of the viscoelastic material, and  $d$  is the distance between the neutral axes of the two face sheets, as shown in Figure 3.1.  $E$ ,  $I$ ,  $A$  and  $k$  represent the Young's modulus, moment of inertia, cross-sectional area and wavenumber.  $X$  and  $Y$  are the shear and structural parameters, respectively. Subscripts  $t$  and  $b$  denote the top and bottom face sheets, and  $c$  denotes the core.

Substituting  $S$  in the expression for  $Y$ , we have

$$Y = \frac{3r(1+r)}{1+r^3}, \quad r = \frac{t_t}{t_b}. \quad (3-22)$$

Differentiating the loss factor with respect to the structural parameter  $Y$  gives

$$\frac{\partial \eta}{\partial Y} = \beta X \frac{1 + 2X + (1 + \beta^2)X^2}{[1 + (2 + Y)X + (1 + Y)(1 + \beta^2)X^2]^2} > 0, \quad (3-23)$$

which is always positive. That means the loss factor is a monotonically increasing function of the structural parameter  $Y$ .

Setting

$$\frac{dY}{dr} = 3 \left[ \frac{1 + 2r}{1 + r^3} - \frac{3r^2(r + r^2)}{(1 + r^3)^2} \right] = 0, \quad (3-24)$$

we obtain  $r = \pm 1$ . So when  $r = 1$ , the loss factor has a maximum value. Then we can define  $t_i = t_b = t_f$ , where the subscript  $f$  stands for the face sheets. In this paper only symmetric sandwich structures have been studied, as shown in Fig. 3.1.

Similarly, by taking the derivative of the loss factor  $\eta$  with respect to the shear parameter  $X$ , an optimal value of the shear modulus  $G$  can be calculated to obtain maximum damping. That means, in an intermediate range of core shear modulus value, the beam or plate damping has its highest value.

The material for the face sheet is a carbon fiber reinforced composite. The Young's modulus of such a material aggregated with epoxy is 60 GPa, similar to that of aluminum. So it is very stiff. Paper honeycombs are manufactured by processing paper with resin to make it water resistant. This produces a low cost core, but one which has very good mechanical properties. PUR foams have low thermal conductivity and diffusion coefficients, giving them very good thermal insulation properties. Another advantage of PUR foams is that they can be produced in finite size blocks as well as in-situ, thus providing an integrated manufacturing process in conjunction with the manufacture of the sandwich elements.

We will compare two cases in order to study the effect of the thicknesses of the face sheets and core on the damping.

1. Since the core is stiff in shear but soft generally, its Young's modulus is much smaller than that of the face sheet. By assuming  $E_c \ll E_f$  and  $D \approx 2D_f + D_0$ , the normal stresses in the face sheets and the shear stresses in the core are

$$\sigma_{f1} = \frac{MzE_f}{2D_{f1} + D_{01}}, \quad \tau_{c1} = \frac{VE_f t_{f1} d_1}{2(2D_{f1} + D_{01})}, \quad (3-25)$$



where  $M$  and  $V$  are the bending moment and the shear force, respectively.

2. If we assume not only that  $E_c \ll E_f$  but also that the face sheets are thin,  $t_f \ll t_c$ , then,  $D \approx D_0$ . The normal stresses in the face sheet and the shear stresses in the core become

$$\sigma_{f2} = \frac{M}{t_{f2}d_2}, \quad \tau_{c2} = \frac{V}{d_2}, \quad (3-26)$$

and the normal stresses in the core and the shear stresses in the face sheets are zero. So the face sheets carry bending moments as tensile and compressive stresses and the core carries transverse forces as shear stresses.

Comparing the two cases, by assuming they have the same core thickness  $t_c$ , bending moment  $M$  and shear force  $V$ , we have

$$\frac{\tau_{c1}}{\tau_{c2}} = \frac{E_f t_{f1} d_1}{2\left(\frac{E_f t_{f1} d_1^2}{2} + \frac{E_f t_{f1}^3}{6}\right)} \cdot d_2 = \frac{d_1 d_2}{d_1^2 + \frac{t_{f1}^2}{3}} < 1, \quad (3-27)$$

and

$$\frac{\sigma_{f1}}{\sigma_{f2}} = \frac{MzE_f}{\frac{E_f t_{f1} d_1^2}{2} + \frac{E_f t_{f1}^3}{6}} \frac{t_{f2} d_2}{M} = \frac{zt_{f2} d_2}{\frac{t_{f1} d_1^2}{2} + \frac{t_{f1}^3}{6}}.$$

Since

$$\max\{\sigma_{f1}\} = \sigma_{f1}\left(z = \pm \frac{d_1 + t_{f1}}{2}\right),$$

then

$$\frac{\max\{\sigma_{f1}\}}{\sigma_{f2}} = \frac{(2t_{f1} + t_c)t_{f2}d_2}{t_{f1}d_1^2 + \frac{t_{f1}^3}{3}} = \frac{2t_{f1}t_{f2}^2 + 2t_{f1}t_{f2}t_c + t_{f2}^2t_c + t_{f2}t_c^2}{\frac{4}{3}t_{f1}^3 + 2t_{f1}^2t_c + t_{f1}t_c^2}.$$

Let  $a = \frac{t_{f1}}{t_{f2}}$ , and  $b = \frac{t_c}{t_{f2}}$ , then

$$\frac{\max\{\sigma_{f1}\}}{\sigma_{f2}} = \frac{2a + 2ab + b + b^2}{\frac{4}{3}a^3 + 2a^2b + ab^2} < 1, \quad \text{if } 1.247 < a < b. \quad (3-28)$$

It is easy to prove that Equation (3-28) is a monotonically decreasing function of  $a$  and  $b$ .

Equations (3-27) and (3-28) show that the thinner the face sheets are, the larger is the shear in the core and the normal stress in the face sheets. That means, if we increase the thickness of the face sheets by a factor more than 1.247, the shear in the core is more constrained. And the direct stress in the face sheets also becomes smaller because the cross-sectional area is larger.

Consider the dynamic case. Vibration energy can propagate through a sandwich structure mainly in the form of bending waves and shear waves. Since bending waves create substantial transverse displacements, bending waves couple best with the surrounding fluid and are mostly responsible for the sound radiation. However, as shown before, the shear deformation in the core is significant in sandwich structures in comparison with homogeneous materials. So shear waves must also be considered. In Section 3.1 the speed of wave in sandwich beam was derived. Based on Eq. (3-19), Fig. 3.2 compares the variation of the bending wave speed in two sandwich beams with different core materials. The MATLAB programs, which are used to calculate the speeds of wave in sandwich structures with isotropic and orthotropic cores, can be found in the appendices. Case (a) corresponds to a single foam core and case (b) a foam-filled honeycomb core. The Young's moduli of the foam core and the foam-filled honeycomb core are 10.16 MPa and 36.4 MPa. In each plot, the curve  $C_p$  represents the speed of

wave propagation including the effects of shear deformation. The upper and lower straight lines depict the pure bending wave speeds of the entire sandwich structure and of the two face sheets only, respectively. Both the plots demonstrate that at low frequencies, the wave speed of the sandwich structure is close to the pure bending wave speed in the entire structure, while at high frequencies, it approaches the speed of the pure bending wave only propagating in the face sheets. Comparing the two plots, it can be seen that, for the sandwich beam with a single foam core, the shear deformation is only effective in the middle frequency range. For a sandwich beam with a foam-filled honeycomb core, however, the shear deformation is still effective in the high frequency range, because the honeycomb increases the stiffness of the core.

Therefore, in the low frequency region the energy is dissipated by pure bending ( $D \approx D_0$ ). With increasing frequency, more energy is dissipated due to the increased normal-to-shear coupling, in which the motion of the face sheets is mostly transformed into the shear deformation and in-plane waves in the core. Because of the viscoelastic property of the foam, the damping in the core is greater than that in the face sheets. Thus the damping has an increasing trend with frequency.

At high frequencies, if the core is very soft compared with the face sheet, the bending stiffness of the face sheets about their own neutral axes is dominant and the total damping is determined by the face sheets ( $D \approx 2D_f$ ). That means that the damping reaches a maximum and decreases again at high frequency [58]. However, for the material studied, the honeycomb increases the stiffness of the core compared with a core made only of foam. So the normal-to-shear coupling is still effective in the high frequency range and thus the damping is increased substantially.

Therefore, with an increase in the face sheet thickness, the damping in the low and high frequency ranges is lower, but it is still high in the middle frequency range. On the other hand, if the thickness of the core is doubled, the damping is very much increased in the middle and high frequency ranges.

### **3.3 Effects of Delamination**

Damage is another mechanism which causes increased damping. Delamination introduces friction in the unbounded region of the interface. And the damping increases with the size of the delamination. Meanwhile, increased damping leads to lower natural frequencies. This effect is significant in the high frequency range [76]. In reference [85] a finite element program developed for a sandwich cantilever beam using NASTRAN shows that the damping increases with increasing delamination. Our experimental results presented in this paper are seen to be consistent with this prediction.

Delamination affects the stiffness of sandwich beams as well. The bending stiffness expression, Eq. (3-1), is derived for undamaged sandwich beams. For beams with delamination, the integral limits become smaller and the resulting bending stiffness is reduced substantially. And if there is delamination on both sides of the beam, the bending stiffness is reduced more than when there is delamination only on one side. This prediction is the same as Frostig's model based on high-order elastic theory [77].

### **3.4 Damping Improvement using Multi-layer Sandwich Structures**

Inspired by the basic sandwich effect, an improved high passive-damping sandwich structure is designed in this chapter. The new structure consists of five layers. Two new

viscoelastic layers are inserted between the core and the face sheets, as shown in Fig. 3.3. The two new layers are expected to introduce more damping into the structure. Since the Young's modulus is changed along the  $z$ -axis, the bending stiffness of a five-layer beam can be obtained by using five integrals. For a symmetric structure,

$$\begin{aligned}
D &= \int E z^2 dA = \int_{-t_f - t_v - \frac{t_c}{2}}^{-t_v - \frac{t_c}{2}} E_f z^2 b dz + \int_{-t_v - \frac{t_c}{2}}^{-\frac{t_c}{2}} E_v z^2 b dz + \int_{-\frac{t_c}{2}}^{\frac{t_c}{2}} E_c z^2 b dz + \int_{\frac{t_c}{2}}^{t_v + \frac{t_c}{2}} E_v z^2 b dz + \int_{t_v + \frac{t_c}{2}}^{t_f + t_v + \frac{t_c}{2}} E_f z^2 b dz \\
&= 2 \int_{t_v + \frac{t_c}{2}}^{t_f + t_v + \frac{t_c}{2}} E_f z^2 b dz + 2 \int_{\frac{t_c}{2}}^{t_v + \frac{t_c}{2}} E_v z^2 b dz + 2 \int_0^{\frac{t_c}{2}} E_c z^2 b dz \\
&= b \cdot \left[ \frac{E_f t_f^3}{6} + \frac{E_v t_v^3}{6} + \frac{E_f t_f d_2^2}{2} + \frac{E_v t_v d_1^2}{2} + \frac{E_c t_c^3}{12} \right] \\
&= 2D_f + 2D_v + D_{f0} + D_{v0} + D_c,
\end{aligned} \tag{3-29}$$

where  $E_c$ ,  $E_v$ ,  $E_f$  are the Young's moduli of the core, the viscoelastic layer and the face sheet, respectively, and  $b$  is the width of the beam. The subscripts  $c$ ,  $v$  and  $f$  represent the core, the viscoelastic layer and the face sheet.  $d_1$  is the distance between the center lines of the two viscoelastic layers,  $d_1 = t_v + t_c$ .  $d_2$  is the distance between the center lines of the two face sheets,  $d_2 = t_f + 2t_v + t_c$ .  $D_f$  and  $D_v$  are the bending stiffnesses of each face sheet and the viscoelastic layer about their own neutral axes,  $D_{f0}$  and  $D_{v0}$  are the stiffnesses of the face sheets and the viscoelastic layers associated with bending about the neutral axis of the entire sandwich, and  $D_c$  is the stiffness of the core.

Therefore, the normal stresses in these layers are:

$$\sigma_f = \frac{ME_f z}{D}, \quad \frac{t_c}{2} + t_v < |z| \leq \frac{t_c}{2} + t_v + t_f, \quad (3-30a)$$

$$\sigma_v = \frac{ME_v z}{D}, \quad \frac{t_c}{2} < |z| \leq \frac{t_c}{2} + t_v, \quad (3-30b)$$

$$\sigma_c = \frac{ME_c z}{D}, \quad |z| \leq \frac{t_c}{2}. \quad (3-30c)$$

Noticing that the shear force  $V_x = \frac{dM}{dx}$ , by definition, the shear stress in the beam is

$$\tau_{xz} = \int_z^{\frac{d_2+t_f}{2}} \frac{d\sigma_x}{dx} dz = \int_z^{\frac{d_2+t_f}{2}} \frac{dM}{dx} \frac{Ez}{D} dz = \frac{V_x}{D} \int_z^{\frac{d_2+t_f}{2}} E z dz = \frac{V_x Q(z)}{D}, \quad (3-31)$$

where  $Q(z)$  is the first moment of area. In the core, or  $|z| \leq \frac{t_c}{2}$ , the first moment of area is

$$Q_c = \int_z^{\frac{t_c}{2}} E_c z dz + \int_{\frac{t_c}{2}}^{t_v+\frac{t_c}{2}} E_v z dz + \int_{t_v+\frac{t_c}{2}}^{\frac{t_c}{2}+t_v+t_f} E_f z dz = \frac{E_c}{2} \left( \frac{t_c^2}{4} - z^2 \right) + \frac{E_v t_v d_1}{2} + \frac{E_f t_f d_2}{2}. \quad (3-32)$$

Similarly, in the viscoelastic layers, for  $\frac{t_c}{2} < |z| \leq \frac{t_c}{2} + t_v$ , we have

$$Q_v = \int_z^{t_v+\frac{t_c}{2}} E_v z dz + \int_{t_v+\frac{t_c}{2}}^{\frac{t_c}{2}+t_v+t_f} E_f z dz = \frac{E_v}{2} \left( \frac{t_c}{2} + t_v + z \right) \left( \frac{t_c}{2} + t_v - z \right) + \frac{E_f t_f d_2}{2}, \quad (3-33)$$

and in the face sheets, for  $\frac{t_c}{2} + t < |z| \leq \frac{t_c}{2} + t_v + t_f$ ,

$$Q_f = \int_z^{\frac{t_c}{2}+t_v+t_f} E_f z dz = \frac{E_f}{2} \left( \frac{t_c}{2} + t_v + t_f + z \right) \left( \frac{t_c}{2} + t_v + t_f - z \right). \quad (3-34)$$

Substituting Eqs. (3-32) to (3-34) back into (3-31), then the shear stresses become

$$\tau_c = \frac{V_x}{D} Q_c, \quad |z| \leq \frac{t_c}{2}, \quad (3-35.a)$$

$$\tau_v = \frac{V_x}{D} Q_v, \quad \frac{t_c}{2} < |z| \leq \frac{t_c}{2} + t, \quad (3-35.b)$$

$$\tau_f = \frac{V_x}{D} Q_f, \quad \frac{t_c}{2} + t_v < |z| \leq \frac{t_c}{2} + t_v + t_f. \quad (3-35.c)$$

From Eq. (3-35) we can find that the maximum shear stress occurs at the neutral axis of the entire beam, when  $z = 0$ ,

$$\max\{\tau_c\} = \tau_c|_{z=0} = \frac{V_x}{D} \left[ \frac{E_c t_c^2}{8} + \frac{E_v t_v d_1}{2} + \frac{E_f t_f d_2}{2} \right], \quad (3-36)$$

and the shear stresses are continuous across the interfaces. On the interface between the core and the viscoelastic layer, the shear stress is

$$\tau_c|_{z=\frac{t_c}{2}} = \tau_v|_{z=\frac{t_c}{2}} = \frac{V_x}{D} \left[ \frac{E_v t_v d_1}{2} + \frac{E_f t_f d_2}{2} \right], \quad (3-37)$$

and on the interface between the viscoelastic layer and the face sheet,

$$\tau_v|_{z=\frac{t_c}{2}+t_v} = \tau_f|_{z=\frac{t_c}{2}+t_v} = \frac{V_x}{D} \frac{E_f t_f d_2}{2}. \quad (3-38)$$

On the free surface of the beam,  $|z| = \frac{t_c}{2} + t_v + t_f$ , from Eq. (3-35.c), the shear stress is zero.

Comparing Eqs. (3-29), (3-30) and (3-35) and the results derived in Section 3.2, we can see that the bending stiffness and the stresses in the five-layer structure are all greater than those of the traditional three-layer sandwich structure. That implies that the insertion of two thin but highly damped viscoelastic layers will improve the material properties and the capability to dissipate energy.

### 3.5 Experiments

We studied three intact and six delaminated beams. Their configurations are listed in Tables 3.1 and 3.2. All the other dimensions of the delaminated beams are the same: length 609.6 mm, width 25.4 mm, core thickness 6.35 mm and face sheet thickness 0.33 mm. Figure 3.4 illustrates a beam with 50.8 mm delaminations on both sides.

#### 3.5.1 Experimental setup

Figure 3.5 shows the experimental set up for the damping measurements on sandwich composite beams. The beams were excited with white noise by a shaker mounted at the middle of the beam. The density of the sandwich material is  $278 \text{ kg/m}^3$  and the mass of the beam A is 27.33 grams. For such a light structure a general purpose accelerometer is not applicable, because the effect of mass loading is significant [109]. Therefore a Polytech laser vibrometer was employed to measure the beam response. The frequency response functions measured by a B&K accelerometer type 4570 shows that the resonance frequencies are 10% lower measured by the accelerometer than the laser vibrometer. The B&K PULSE system was used to analyze the signals with the Dual FFT mode and the damping ratio was determined directly.

At low frequencies, the coherence between the response and force is very poor for lightweight structures, because the surrounding airflow affects the excitation-response relationship. So it is difficult to obtain satisfactory measurements for the first mode. One solution is to excite the structures and to measure the corresponding responses in extremely narrow frequency bands. In practice both the 3.125 Hz band and the 1.63 Hz band were used to excite the structures and make measurements using the zoom FFT



mode. Since the beams were excited in a very narrow band, in which the excitation energy was concentrated, the airflow influence is negligible. In that way the coherence between the force excitation and response was increased up to 0.977.

### **3.5.2 Experimental results**

Figures 3.6 and 3.7 compare the receptance frequency response functions and damping ratios of beams with single and double-layer face sheets. Double-layer face sheets add 13% more mass to the beams. Figure 3.6 shows that the vibration properties do not change very much. However, from Fig. 3.7 we can see that, as expected, the damping in beam B is lower than that in beam A (see Table 3.1) in the low and high frequency ranges, because the thicker face sheets constrain the deformation of the core in beam B more than in beam A. However, in the middle frequency range, the damping ratio reaches its maximum value.

Figures 3.8 and 3.9 compare the receptance frequency response functions and damping ratio in beams A and C. The density of the core is  $156 \text{ kg/m}^3$ . So a core which is twice as thick adds 56% more mass to the beam. Then the natural frequencies shift dramatically to lower frequencies. And the damping increases, especially in the middle and high frequency ranges.

Figures 3.10 and 3.11 show the receptance frequency response functions and damping ratio of the intact beam A and the delaminated beam D. From Fig. 3.11 we can see that the effect of delamination is more obvious in the high frequency range. The damping increases as the mode number increases.

Figures 3.12 and 3.13 show the damping ratios of the delaminated beams. With 5% delamination, the damping of each mode increases evenly. With 10% delamination, the damping ratio of the second mode is seen to be very high. With 20% delamination, both the first and the second modes have very high damping. Beams with delaminations on both sides have more damping than those with delamination only on one side.

The fundamental frequency of a cantilever beam is given by

$$f_1 = \frac{3.5160}{2\pi} \sqrt{\frac{EI}{mL^4}}, \quad (3-39)$$

where  $m$  is the mass per unit length and  $L$  is the length of the beam. Then the equivalent Young's modulus can be obtained by measuring the fundamental frequencies of the intact and delaminated sandwich beams. Figure 3.14 shows the effect of delamination on the equivalent Young's modulus.

### 3.5.3 Discussion

As discussed before, the system loss factor  $\eta$  reaches a maximum value when the shear modulus of the core has an optimal value in the intermediate range. In the Ross-Ungar-Kerwin model, the shear parameter  $X$  is inversely proportional to the core thickness  $t_c$ . This means that only when the core thickness is also in an optimal range, can the damping reach a maximum value. He and Rao reported the same prediction using a numerical simulation [49]. However, the loss factor also depends on the total bending stiffness which is also affected by the core thickness. Mead proved that the loss factor  $\eta$  is much less sensitive to the change of the shear parameter  $X$  when the structural parameter  $Y$  is large [12]. The shear parameter is then in a much wider range of the

optimum value for maximum  $\eta$ . In He and Rao's study, the core is thinner than the face sheets and  $Y = 27$ . However, for the beams studied in this paper, the face sheets are much thinner than the cores. So the structural parameter is large as listed in Table 3.1.

In addition, Mead presented the relationship between the maximum loss factor  $\eta_{\max}$  and the structural parameter  $Y$ :

$$\eta_{\max} = \frac{\beta Y}{(2 + Y) + 2\sqrt{(1 + Y)(1 + \beta^2)}} \quad (3-40)$$

Taking the derivative of  $\eta_{\max}$  yields:

$$\frac{d\eta_{\max}}{dY} = \frac{\beta[2 + Y + 2\sqrt{(1 + Y)(1 + \beta^2)}] - \beta Y[1 + \frac{1 + \beta^2}{\sqrt{(1 + Y)(1 + \beta^2)}}]}{[2 + Y + 2\sqrt{(1 + Y)(1 + \beta^2)}]^2} = \frac{A}{B} \quad (3-41)$$

The denominator  $B$  is always positive. The numerator  $A$ :

$$\begin{aligned} A &> \beta[2 + 2\sqrt{(1 + Y)(1 + \beta^2)} - Y\sqrt{\frac{1 + \beta^2}{1 + Y}} - \sqrt{1 + \beta^2}] \\ &= \beta[2 + 2\sqrt{(1 + Y)(1 + \beta^2)} - \sqrt{(1 + Y)(1 + \beta^2)}] \\ &= \beta[2 + \sqrt{(1 + Y)(1 + \beta^2)}] > 0 \quad (3-42) \end{aligned}$$

So the derivative (3-41) is always positive. This means that the loss factor increases monotonically with increasing value of  $Y$ , if other parameters are fixed. The theoretical analysis given in Section 3.2 and the experimental results presented in this paper agree with Mead's prediction.

<b>Intact beams</b>	<b>Length (mm)</b>	<b>Width (mm)</b>	<b>Core thickness (mm)</b>	<b>Face sheet thickness (mm)</b>	<b>Structural parameter <i>Y</i></b>
Beam A	609.6	25.4	6.35	0.33	1229
Beam B	609.6	25.4	6.35	0.66	338
Beam C	609.6	25.4	12.7	0.33	4627

Table 3.1. Configurations of intact beams.

<b>Delaminated beams</b>	<b>Delamination length (mm) (percentage of length)</b>	<b>Delamination location</b>
Beam D	12.7 (5%)	One side
Beam E	12.7 (5%)	Both sides
Beam F	25.4 (10%)	One side
Beam G	25.4 (10%)	Both sides
Beam H	50.8 (20%)	One side
Beam I	50.8 (20%)	Both sides

Table 3.2. Configurations of beams with delamination.

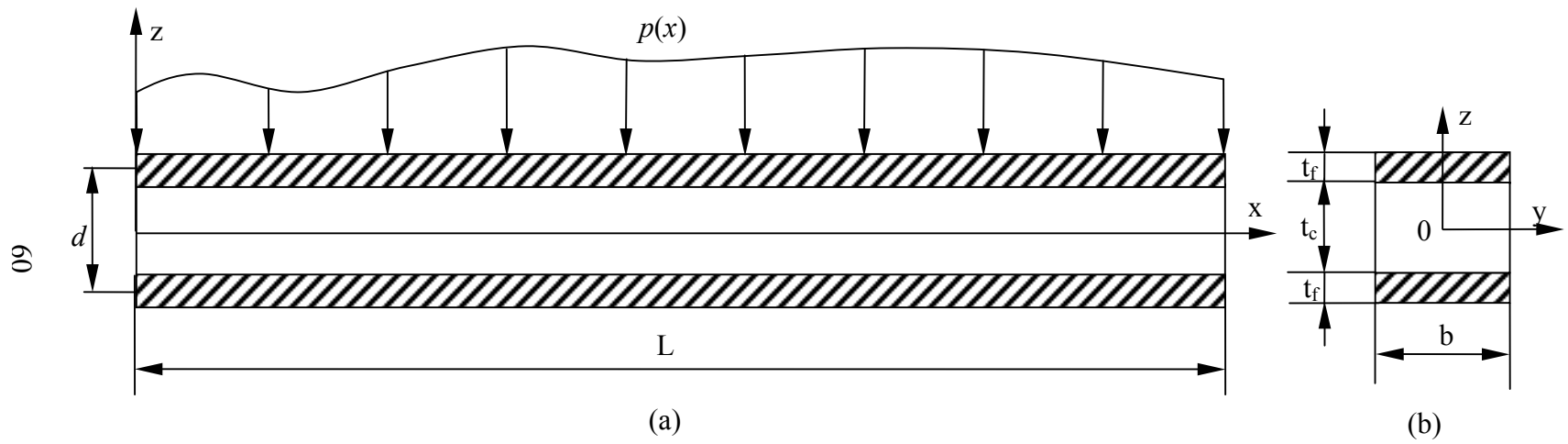


Figure 3.1. A symmetric sandwich beam. (a) Side view, (b) cross section.

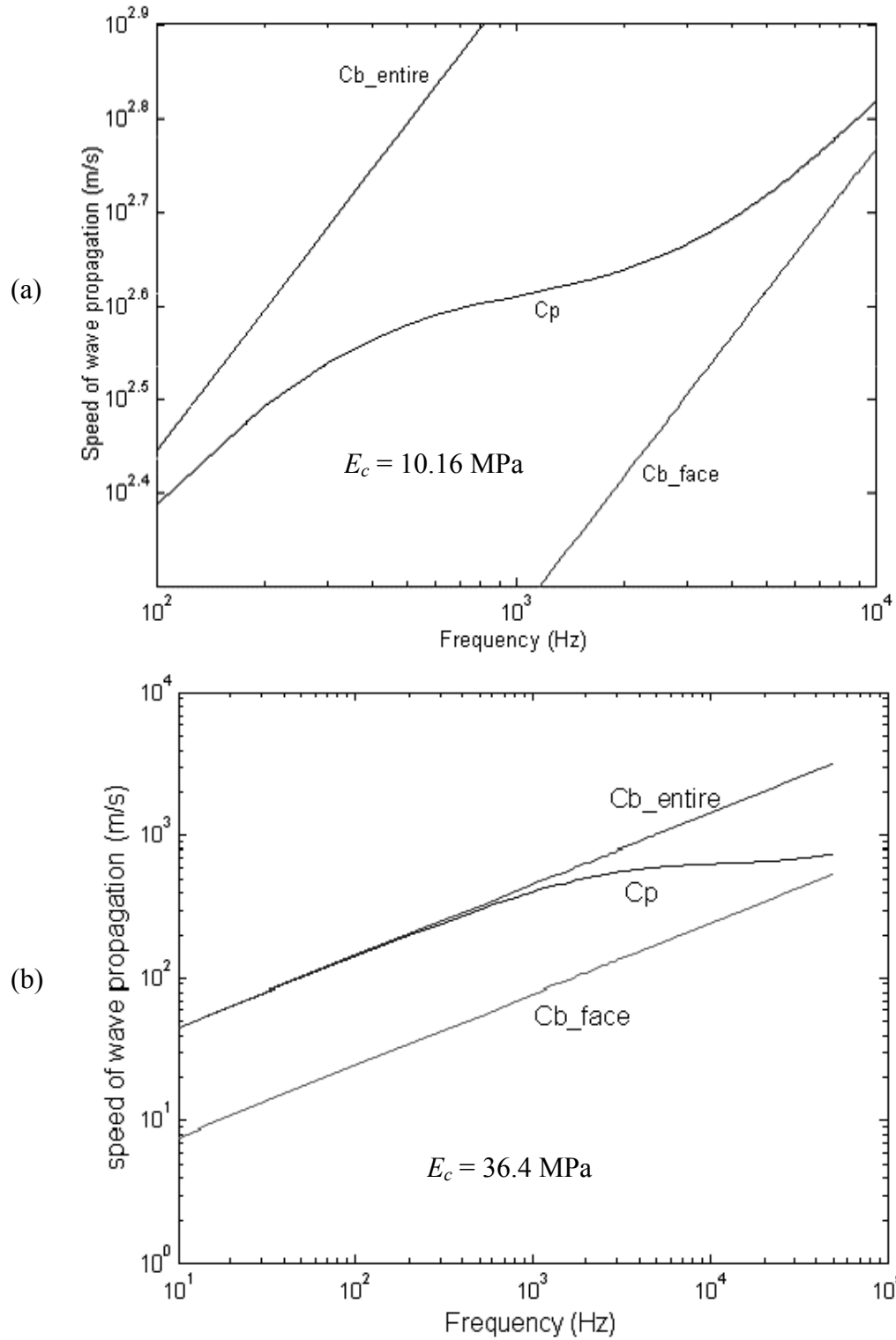


Figure 3.2. Dispersion relation for sandwich beams with a single foam core (a) and a foam-filled honeycomb core (b).

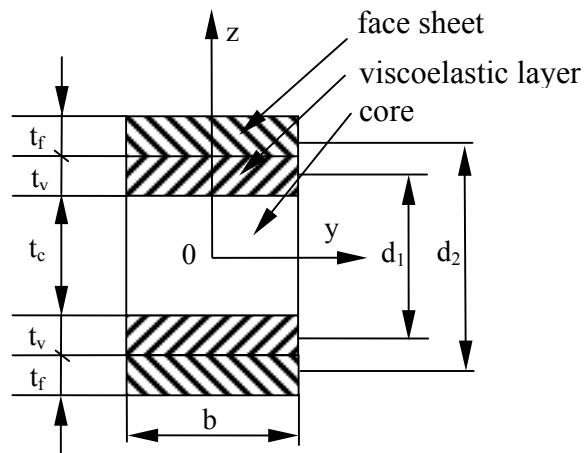


Figure 3.3. The cross section of a five-layer sandwich beam.

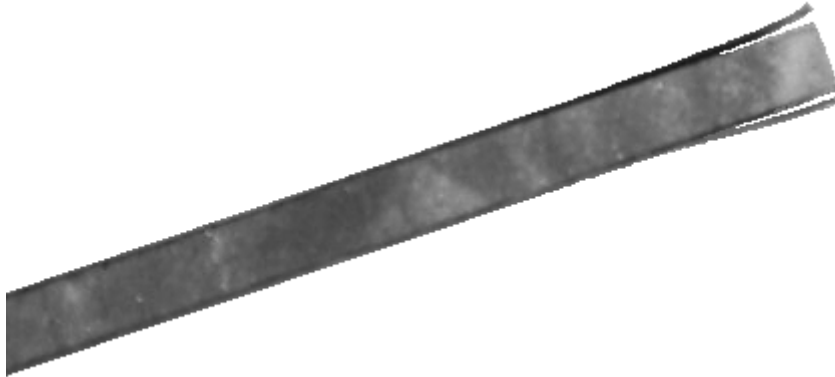


Figure 3.4. A beam with 50.8 mm delaminations on both sides.





Figure 3.5. Experimental setup for damping measurements.

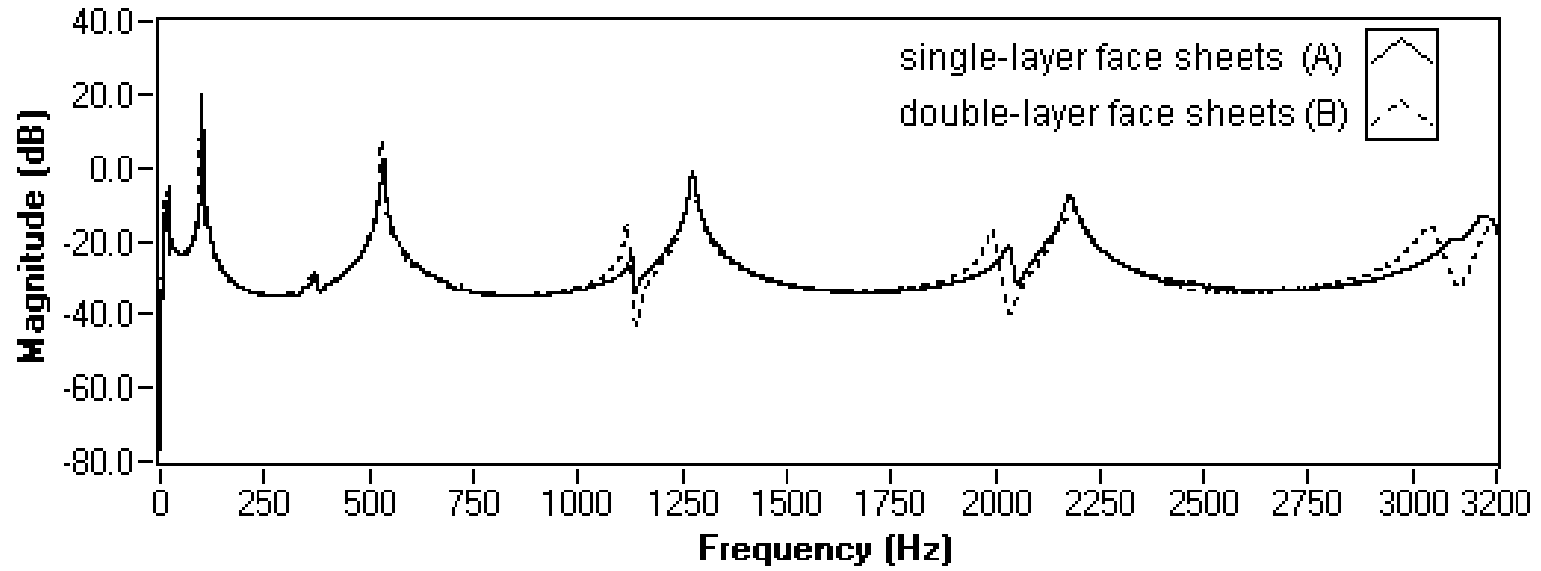


Figure 3.6. Receptance FRFs of beams A and B.

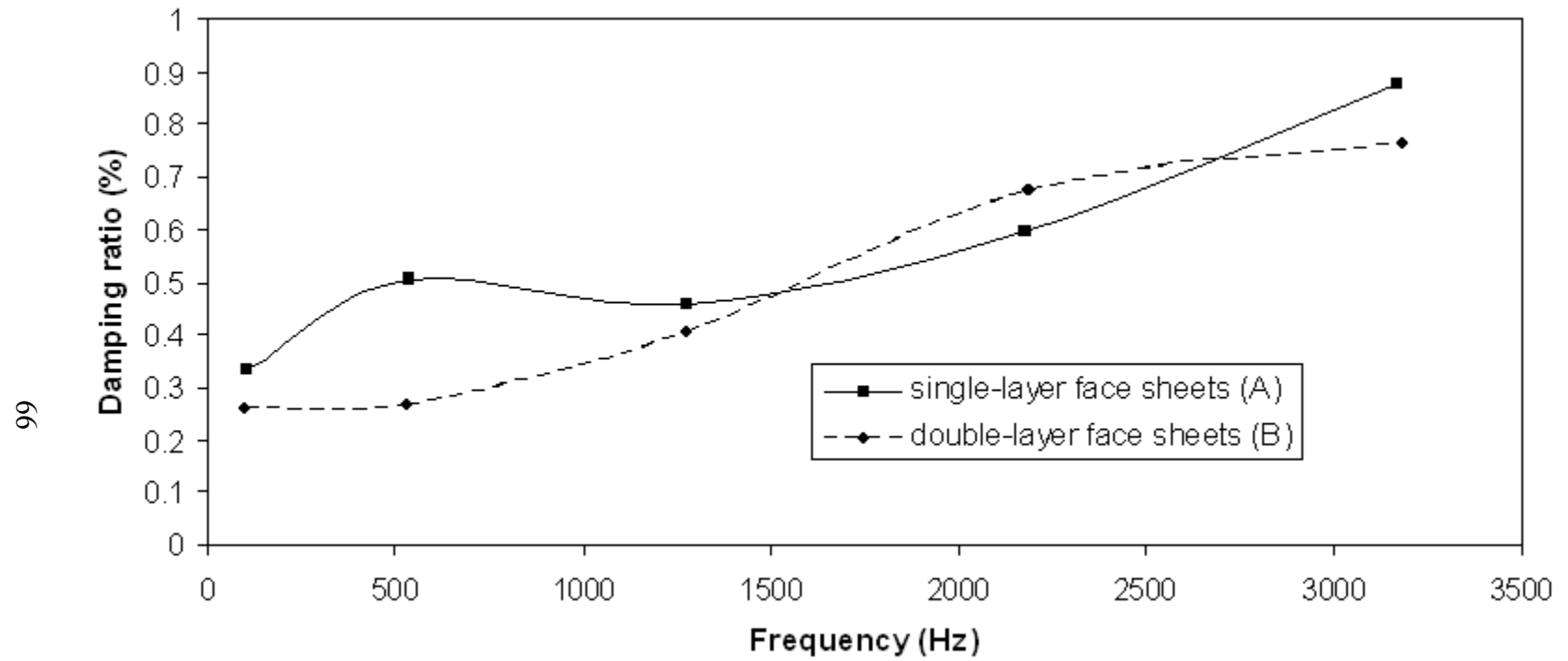


Figure 3.7. Comparison of damping ratio in beams A and B.

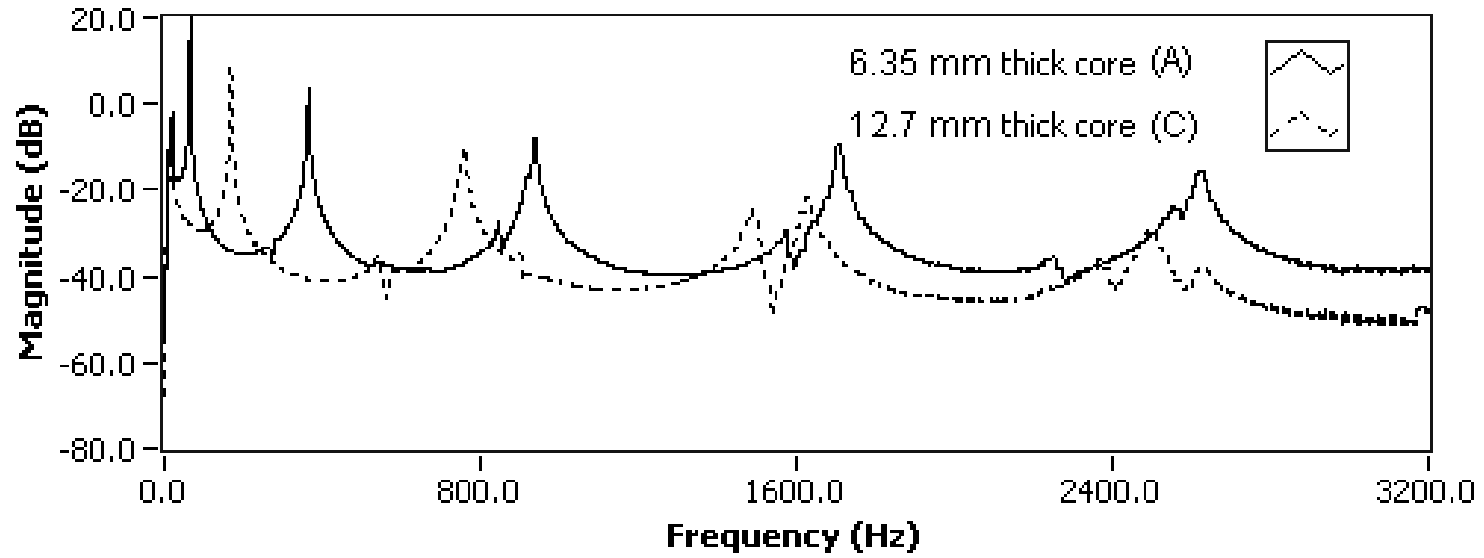


Figure 3.8. Receptance FRFs of beams A and C.

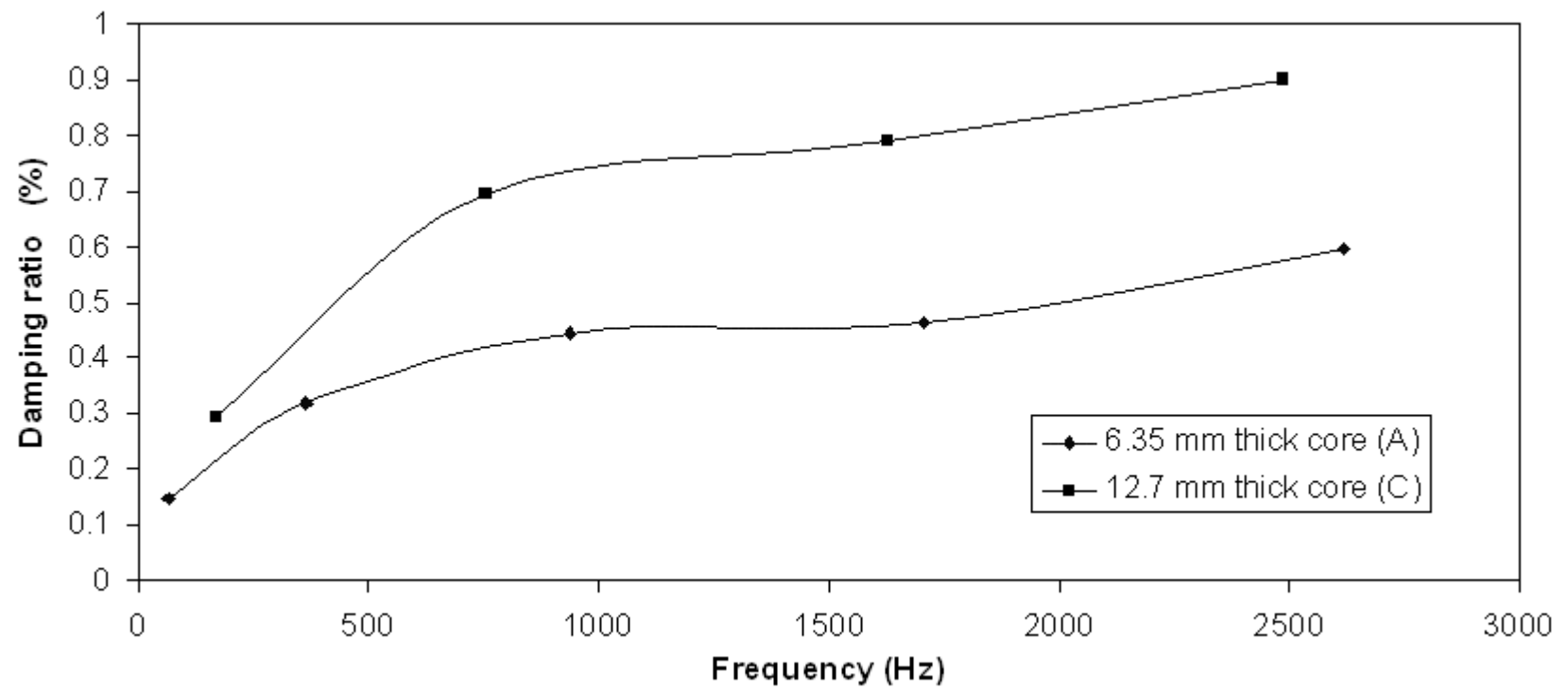


Figure 3.9. Comparison of damping ratio in beam A and beam C.

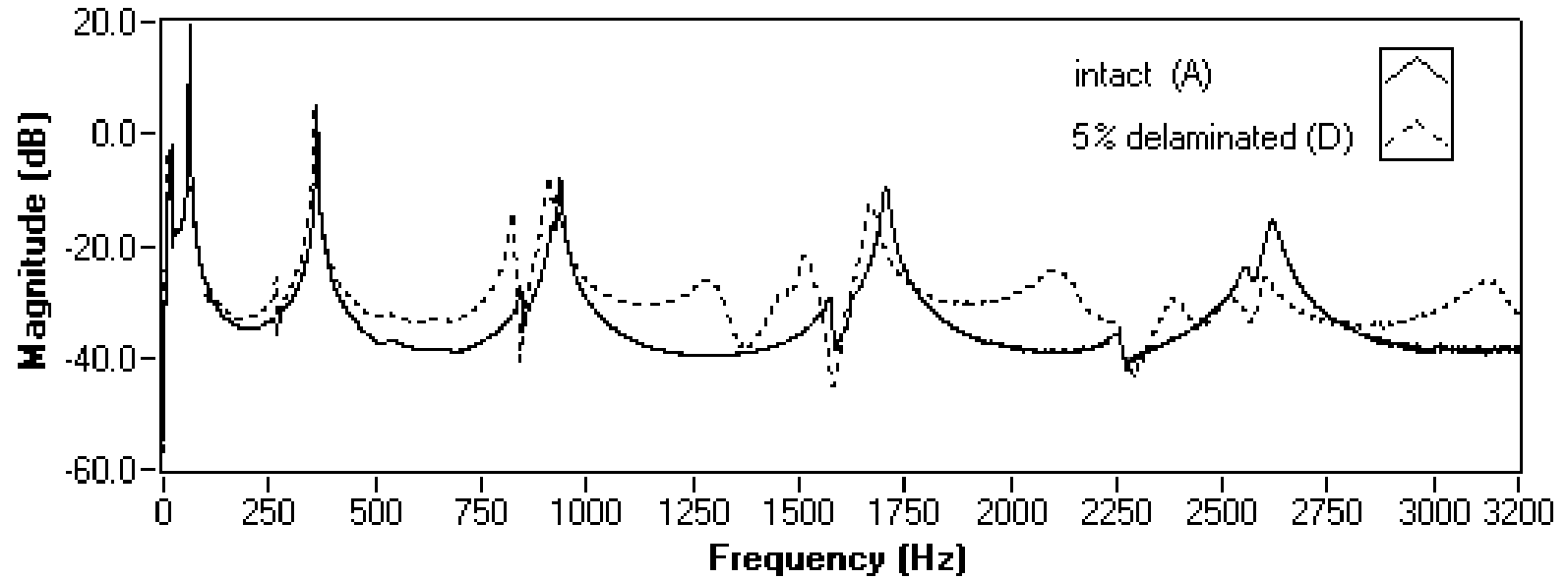


Figure 3.10. Receptance FRFs of intact beam A and delaminated beam D.

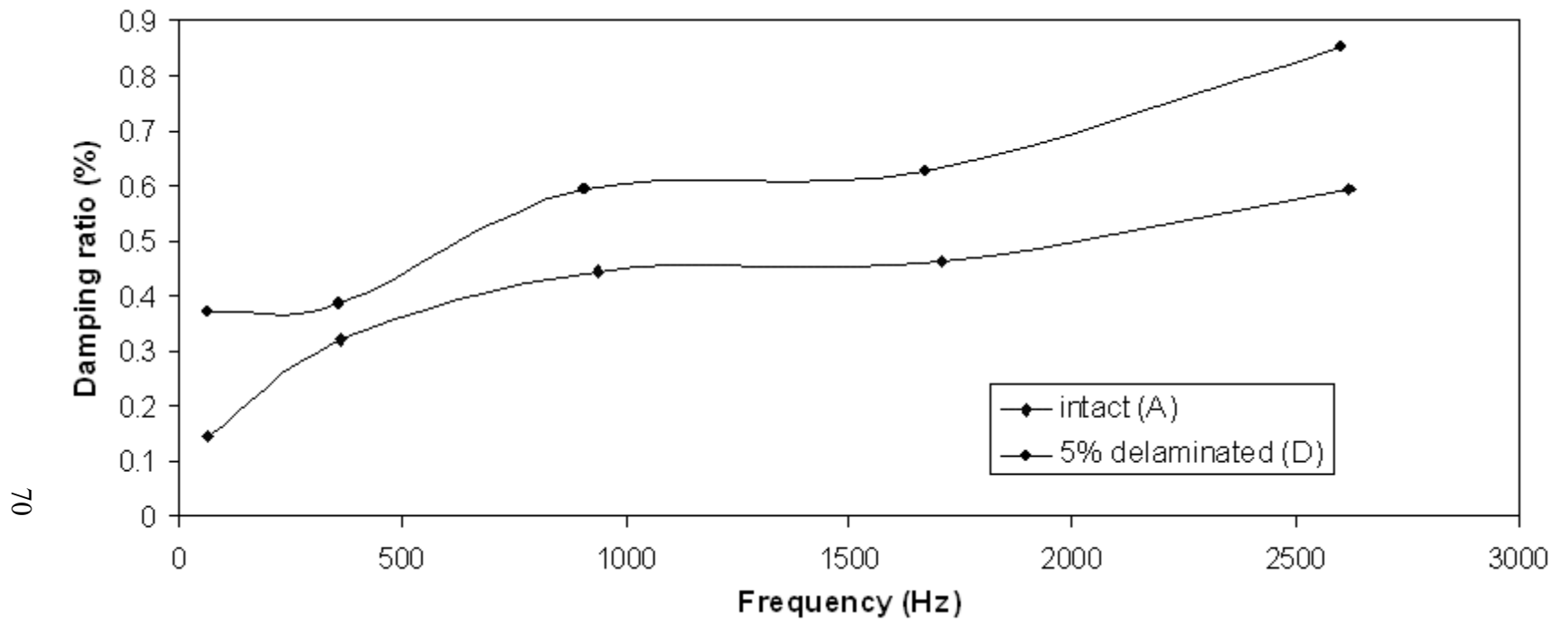


Figure 3.11. Comparison of damping ratio of intact beam A and delaminated beam D.

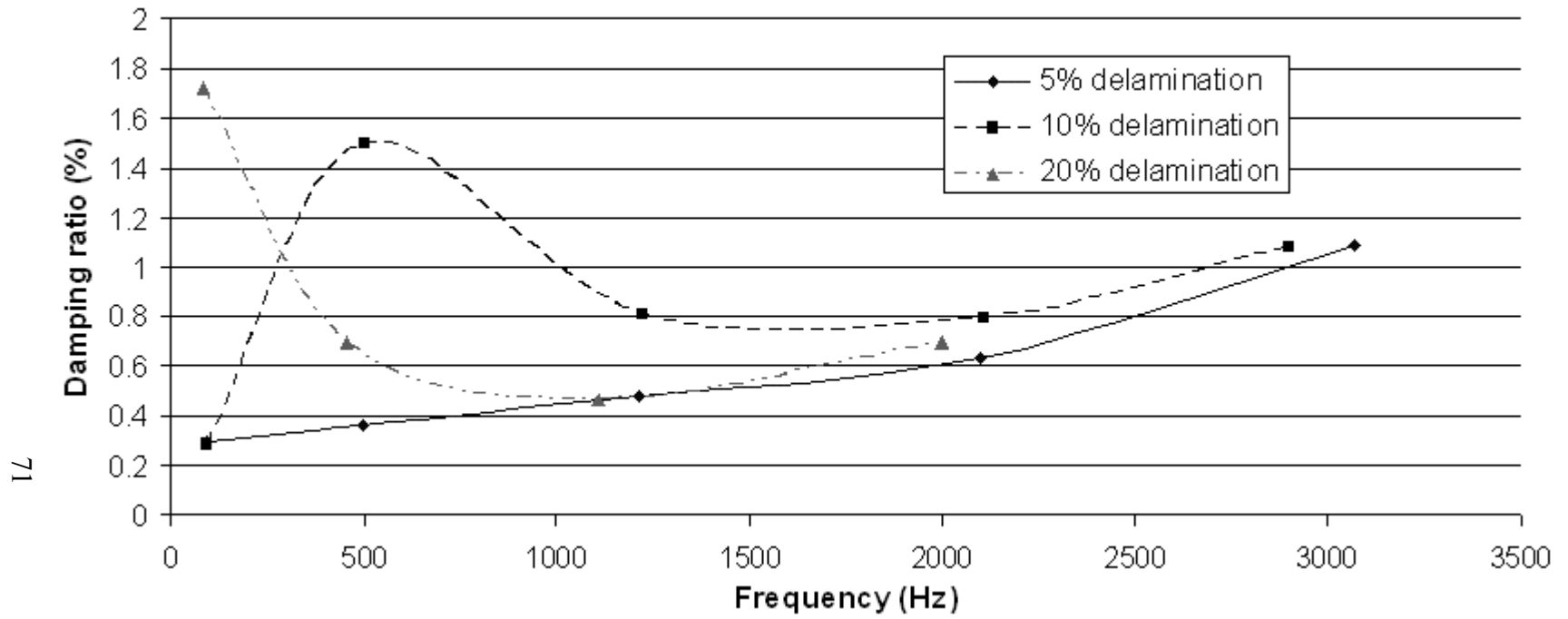


Figure 3.12. Damping ratios of beams with delamination only on one side.



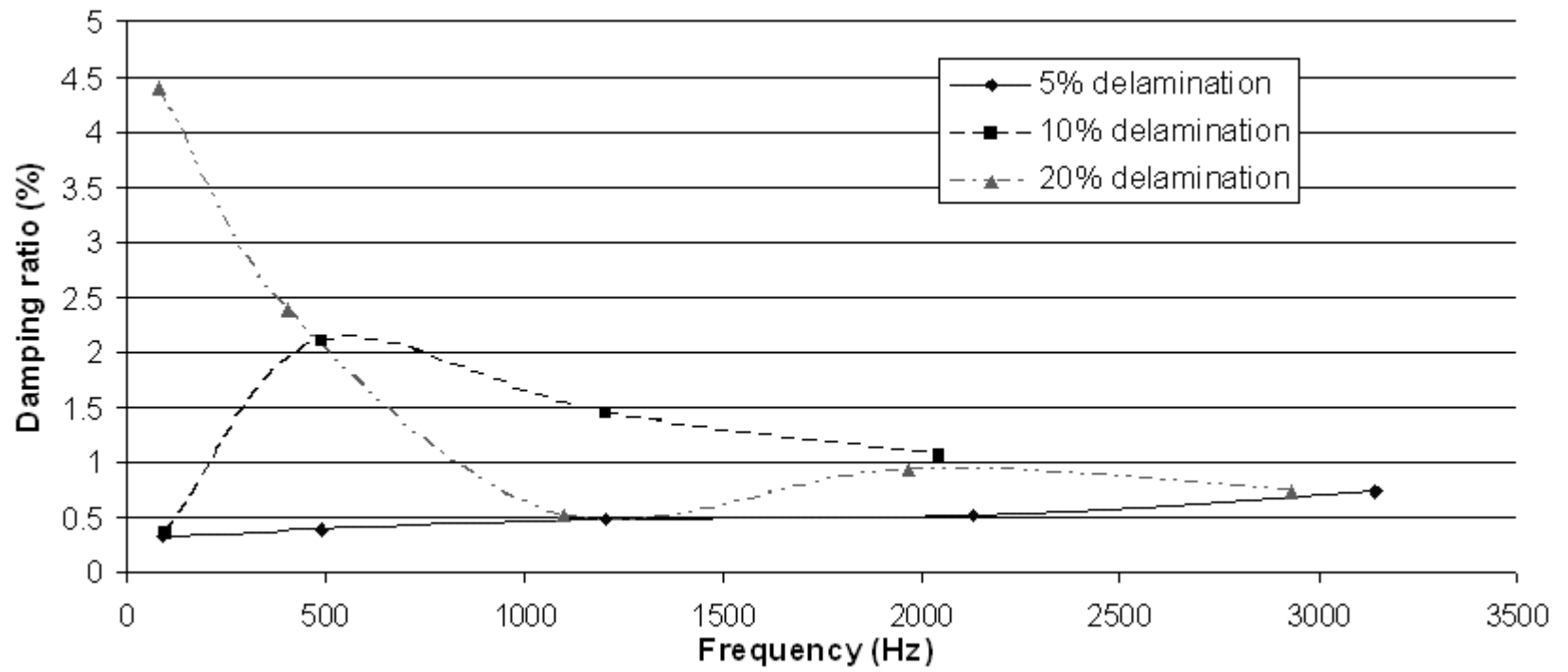


Figure 3.13. Damping ratios of beams with delaminations on both sides.

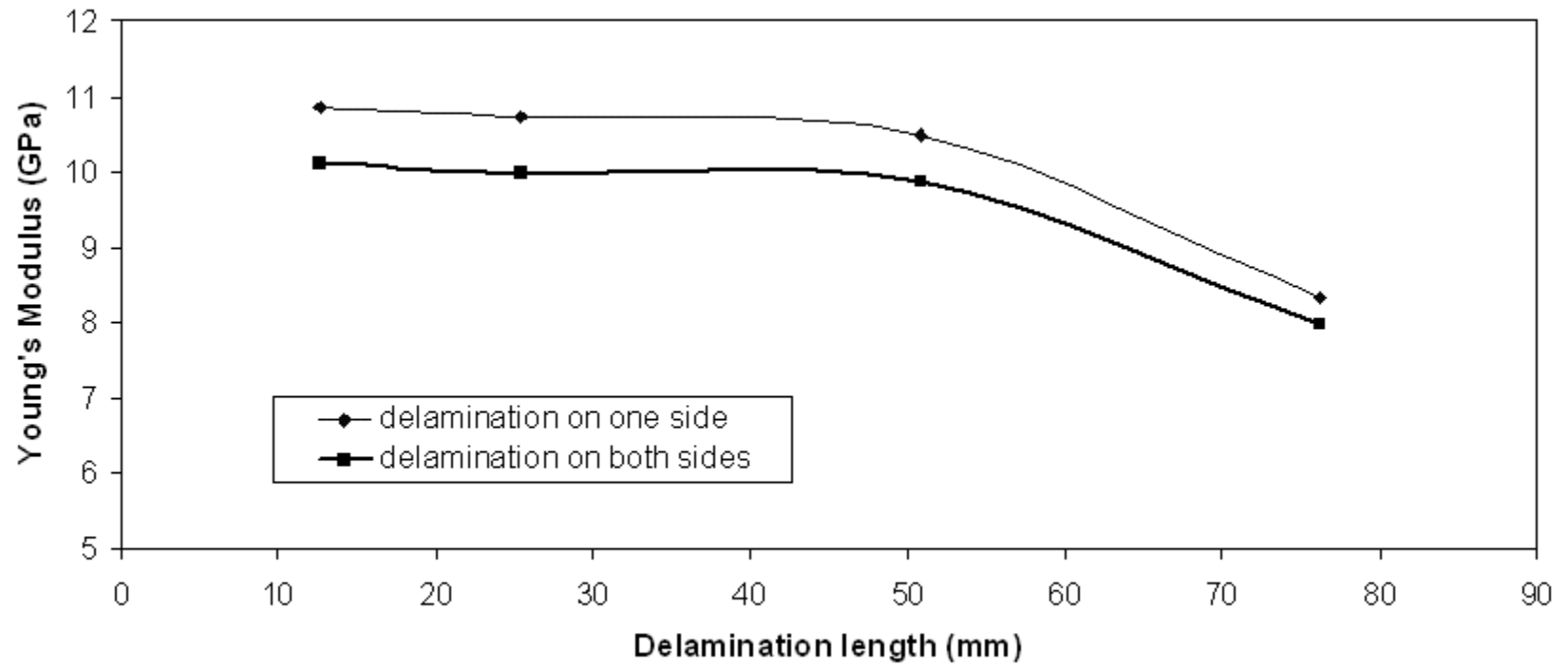


Figure 3.14. Young's modulus of sandwich beams as a function of delamination length.

## **CHAPTER 4 DAMPING CALCULATION AND MODAL TESTING USING WAVELET AND GABOR ANALYSES**

Three elementary parameters used in the modal analysis of a dynamic system are its natural frequency, modal damping and magnitude. A considerable amount of attention has been devoted to frequency response function (FRF) analysis [20,110,111]. However, the conventional Fourier analysis approach is restricted to only one domain, because the elementary functions used to decompose the signals exist from negative infinity to positive infinity in the time domain. In other words, Fourier analysis cannot provide information on how the frequency contents of a signal change with time. Therefore, Fourier analysis is only useful for stationary signals. For non-stationary signals, time-frequency representations are needed. Consider a simple case, the decay of free vibration. The decaying vibration signal is non-stationary because its magnitude decreases exponentially. So it can be viewed as a transient phenomenon. Although it is not difficult to calculate the loss factor by the decay rate method for lightly damped systems, the method only works for a single mode at resonance, and the result is very sensitive to noise. Joint time-frequency analysis (JTAF) can be used instead to separate the modal components contained in signals and to reduce noise. The modal parameters of each mode separated thus can be extracted.

Joint time-frequency analysis algorithms fall into two categories: the linear JTFA and the quadratic JTFA. In the linear JTFA, the short-time Fourier transform (STFT) and

the Gabor expansion, which can be regarded as the inverse of the STFT, are two algorithms. If we consider the linear JTFA as the evolution of the conventional Fourier transform, the quadratic JTFA is the counterpart of the standard power spectrum. Quadratic algorithms include the Gabor spectrogram, Cohen's Class and the adaptive spectrogram [112-114]. The difference between linear and quadratic JTFA methods is that the linear transform can be inverted to reconstruct the time signal. Thus, the linear transform is suitable for signal processing, such as time-varying filtering. However, the quadratic JTFA describes the energy distribution of the signal in the joint time-frequency domain, which is useful for signal analysis. Since the phase information is lost in the quadratic time-frequency representation, the time histories cannot be reconstructed. In this paper both the linear and quadratic JTFA approaches are used for damping calculations.

In this chapter the damping calculation and model testing methods using wavelet and Gabor analyses are studied. This chapter starts with a brief introduction to the wavelet and Gabor analyses. The modal extraction technique using the undecimated wavelet-based denoising method in the FRF analysis is then presented in Section 4.2. In order to decouple the components in a free vibration signal and then calculate the damping and mode shapes, a new modal testing approach based in the Gabor expansion was proposed in Sections 4.3 and 4.4.

#### **4.1 Wavelet and Gabor Analyses**

Wavelet and Gabor analyses are two sorts of JTFA. The continuous wavelet and Gabor transforms of a time signal  $x(t)$  are defined as

$$CWT(a,b) = \langle x, \psi_{a,b} \rangle = \frac{1}{\sqrt{|a|}} \int_{-\infty}^{+\infty} x(t) \psi^* \left( \frac{t-b}{a} \right) dt, \quad (4-1)$$

$$CGT(b, \omega) = \langle x, g_{b,\omega} \rangle = \int_{-\infty}^{+\infty} x(t) g^*(t-b) e^{-j\omega t} dt, \quad (4-2)$$

where the elementary functions are

$$\psi_{a,b} = \frac{1}{\sqrt{|a|}} \psi \left( \frac{t-b}{a} \right), \quad (4-3)$$

$$g_{b,\omega} = g(t-b) e^{j\omega t}, \quad (4-4)$$

and \* denotes the complex conjugate.

A comparison of Eqs. (4-1) and (4-2) shows that the wavelet transform and the Gabor transform are similar except that the elementary functions are different. The wavelet transform uses the dilated and translated version of the mother wavelet  $\psi(t)$  to decompose the signal, while the Gabor transform uses the modulated and shifted copy of  $g(t)$ . Both  $\psi_{a,b}$  and  $g_{b,\omega}$ , however, are concentrated at a region of the time-frequency plane. For example,

$$CWT(a = \frac{\omega_0}{\omega}, b = t) = TF(t, \frac{\omega_0}{\omega}), \quad (4-5)$$

and

$$CGT(b = mT, \omega = n\Omega) = TF(mT, n\Omega). \quad (4-6)$$

From the two equations above, we can show that the bandwidth of the elementary functions in the wavelet transform varies with its center frequency, while the bandwidth of the elementary functions in the Gabor transform does not. This difference leads to the fact that the time-frequency resolutions of these two transforms are different. According to the Heisenberg Uncertainty Principle, we cannot obtain high time-resolution and high

frequency-resolution simultaneously. The wavelet transform has high time-resolution but low frequency-resolution at high frequency, and high frequency-resolution but low time-resolution at low frequency. However, the Gabor transform has a constant time-frequency resolution once the analysis window is determined [113]. Figure 4.1 compares the sampling grids of the wavelet transform and the Gabor transform. These features are appropriate for different applications.

For example, a high-frequency signal lasts for a short time physically. Then it is necessary to use a function with a high time-resolution to analyze the signal. On the other hand, a low frequency signal lasts for a long time. Then an elementary function with a low time-resolution is acceptable. However, this low frequency signal may have a narrow bandwidth because of the time-scaling property of the Fourier transform. So we need an elementary function with a high frequency-resolution. Wavelets satisfy such requirements.

For computer applications, numerical wavelet analysis (discrete wavelet transform, or referred to as DWT) is implemented by filter banks [113,115].

On the other hand, the discrete Gabor transform for a given discrete time sequence  $x[k]$  is computed from

$$C_{m,n} = \sum x[k] \gamma^*[k - mT] e^{\frac{j2n\pi k}{N}}, \quad (4-7)$$

where  $C_{m,n}$  is a matrix whose entries are called the Gabor coefficients,  $\gamma[k]$  is the analysis window, and  $*$  denotes the complex conjugate. The parameters  $T$  and  $N$  represent the discrete time sampling interval and the total number of frequency lines [113]. The analysis function  $\gamma[k]$  is localized in the joint time-frequency domain. So the Gabor coefficients will depict the local time-frequency properties of  $x[k]$ .

Random noise is evenly distributed over the entire joint time-frequency domain because it is not limited to a short time period or a narrow frequency band. On the contrary, the joint time-frequency representation of a signal is always concentrated in a relatively small region. After identifying the signal component, a mask can be applied to filter the signal components and take the inverse transform in order to obtain the noise-free waveform signal in the time domain.

After computing the Gabor coefficients by Eq. (4-7), a time-varying filter, which is actually a two-dimensional binary mask function  $M_{m,n}$ , is used to modify the Gabor coefficient as

$$\hat{C}_{m,n} = M_{m,n} C_{m,n} . \quad (4-8)$$

The component of interest can then be extracted. As long as some requirements are satisfied, the component in the time domain can be reconstructed as

$$\hat{x}[k] = \sum_{m=0}^{M-1} \sum_{n=0}^{N-1} \hat{C}_{m,n} h[k - mT] e^{\frac{j2\pi nk}{N}} , \quad (4-9)$$

where  $h[k]$  is called the synthesis function [113,116]. Qian had shown that if the functions  $h[k]$  and  $\gamma[k]$  are identical, the Gabor coefficients of the reconstructed signal  $\hat{x}[k]$  will be optimally close to  $\hat{C}_{m,n}$ , in the sense of least square error. This process is called orthogonal-like Gabor transformation [113]. In this procedure Eq. (4-7) is called the Gabor transform (or analysis). And the inverse transform Eq. (4-9) is called the Gabor expansion (or synthesis).

The Gabor transform is linear JTFA. The quadratic Gabor analysis is called Gabor spectrogram. Based on the Gabor transform, the Gabor spectrogram is defined as

$$GS_D[i, k] = \sum_{|m-n|+|n-n'| \leq D} C_{m,n} C_{m',n'} WVD_{h,h}[i, k] , \quad (4-10)$$

where  $WVD_{h,h}[i, k]$  is the cross Wigner-Ville distribution of the frequency-modulated Gaussian functions. The order of the Gabor spectrogram,  $D$ , controls the degree of smoothing [114].

#### 4.2 Modal Extraction using Wavelet Analysis

In the modal bandwidth method introduced in Chapter 2, in order to obtain high coherence between the spectra of acceleration and force and to avoid frequency leakage, zoom measurement with sufficient frequency resolution was used for each mode. The maximum frequency resolution of the B&K PULSE system is 6400 lines. However, because of the fact that the sandwich composite materials have a more complicated performance than homogenous metals, vibration signals tend to be much noisier. Even after 400 averages, the frequency response function was not smooth enough with such high resolution. Figure 4.2 (a) shows a noisy acceleration FRF measured on a sandwich beam at the resonance frequency of 135 Hz. Since the frequency response function is in the frequency domain, the general filtering technique does not work. Fortunately, we can calculate the convolution of the frequency response with a smooth function. Wavelet analysis is suitable for noise reduction in this situation.

The model for a noisy signal can be expressed as

$$x[k] = s[k] + \sigma \cdot n[k], \quad k = 0, \dots, L-1, \quad (4-11)$$

where  $k$  is the index of the data sample, and  $L$  is the length of the data.  $x[k]$  is the noisy signal,  $s[k]$  is the true signal we want to recover,  $n[k]$  is assumed to be Gaussian white



noise, and  $\sigma$  is the noise level. With two-channel filter banks consisting of pairs of lowpass and highpass filters, the signal is decomposed into low-frequency outline and high-frequency detail as shown in Fig 4.2 (b) and (c). The small coefficients from the highpass filter are dominated by noise  $n[k]$ , while coefficients with high absolute values carry more signal information  $s[k]$  [118]. Replacing the small, noisy coefficients by zero, we can obtain the essential signal with less noise.

Donoho proposed the wavelet-thresholding denoising method based on the traditional DWT, or decimation algorithm [119]. This method consists of three stages, decomposition (referred to as analysis), thresholding detail coefficients, and signal reconstruction (referred to as synthesis).

After the raw signal is decomposed by multi-resolution analysis (MRA) through two-channel filter banks at some level, the soft threshold, defined as the fixed form  $t = \sqrt{2 \cdot \log(L)}$ , is performed to the detail coefficients from the highpass filter. The soft thresholding method sets all the detail coefficients with absolute values lower than the threshold to zero and then shrinks all the other detail coefficients towards zero. The soft thresholding method has better mathematical properties than the hard thresholding method. The advantages of the DWT are that the coefficients of the analysis and synthesis filters do not change at each stage of MRA and the computation complexity decreases continuously. However, because of decimation, or what is known as downsampling, for each order, the time-resolution of the signal is much lower than the raw data. It has to be reconstructed to restore the original time resolution. In Fig. 4.2, (a) is the raw acceleration frequency response function signal, and (b) and (c) are the output of the lowpass and highpass filters after the fifth-order MRA, respectively. The wavelet

used is biorthogonal with 5<sup>th</sup> order analysis (decomposition) filter and 3<sup>rd</sup> order synthesis (reconstruction) filter, or the so-called bior3\_5 wavelet. Because the analysis filter is built by a fifth-order spline function, the analysis mother wavelet is very smooth. The x-axes of the plots are the numbers of the data samples. The number of frequency lines of the raw FRF is 6400. After the fifth-order MRA, the number of frequency lines of the data in (b) and (c) become 200. That means the time-resolution is  $2^5 = 32$  times less than that of the original signal. So the signal must be reconstructed using the output of each order of the filter banks to get a smooth curve. It is important to note that the coefficients of the synthesis filters, which construct the dual filter bank of the analysis filter bank, must converge. Note that the synthesis using bio3\_5 wavelet does not converge although its analysis effect is very good.

Moreover, as the traditional DWT is translation-variant due to the decimation, the signal reconstructed from the wavelet coefficients with the nonlinear soft threshold may also include some distortion. If the maximum point is not at the decimated sample point, it may be neglected after the thresholding.

An alternative is the so-called A'trous algorithm, or sometimes known as the undecimated DWT. It uses the same filter banks scheme, but the decomposition is time-invariant [117]. In other words, the resolution of the signal does not decrease after decomposition. So it is not necessary to reconstruct the signal. Because of the same reason, the convergence of the synthesis filters is not required. Another advantage of the undecimated DWT is that the denoising result has a better balance between the smoothness and accuracy than the traditional DWT. So the denoising based on the undecimated wavelet transform is superior to the method using the standard DWT.

In order to test the accuracy of the undecimated DWT denoising method, the following simulation was conducted. The forced response of a single DOF system is governed by

$$\ddot{x}(t) + 2\zeta\omega_n\dot{x}(t) + \omega_n^2x(t) = F \cos \omega t ,$$

where  $\zeta$  is the damping ratio,  $\omega_n$  is the undamped natural angular frequency, and  $F$  is the force magnitude. Since white noise is used to excite the structure,  $F$  is constant in the frequency range we are interested in. The acceleration magnitude is then

$$A(\omega) = \frac{F}{\sqrt{\left[1 - \left(\frac{\omega}{\omega_n}\right)^2\right]^2 + \left(\frac{2\zeta\omega}{\omega_n}\right)^2}} . \quad (4-12)$$

Figure 4.3 (a) illustrates a simulated noisy accelerance FRF, where  $\zeta = 0.02$  ,  $F = 0.001$  , the natural frequency  $f_n = 200$  Hz, and the standard deviation of the Gaussian white noise is 0.1. Figure 4.3 (b) shows the denoising result using a five-order undecimated DWT. The filter coefficients are derived from the bio3\_5 wavelet. It can be seen that the FRF signal is greatly improved. Table 4.1 lists the detected natural frequencies and damping ratios for different standard deviation levels of the Gaussian white noise. The numbers in parentheses are relative errors.

### 4.3 Damping Calculation using Gabor Analysis

In some applications, information about the excitation force is not available. Although the decay rate method can be used to evaluate the loss factor from a free vibration signal, as mentioned at the beginning of this chapter, the decay rate method only works for a single mode at resonance, and the result is very sensitive to noise.

Schwarz and Richardson use a curve fitting technique to estimate the modal parameters from ambient response data [120]. Bonato et al. use Cohen's class to estimate the modal parameters from the non-stationary response to an unknown excitation [121]. However, the algorithms in Cohen's class, such as the Wigner-Ville Distribution, have cross-term interferences in the time-frequency representation. References [122] and [123] present a method for the determination of the logarithmic decrement of free vibration by using the wavelet scalogram. However, as demonstrated before, the frequency-resolution of the wavelet transform decreases with increasing frequency. If more than one mode exists in the vibration decay signal, satisfactory resolution for all modes cannot be obtained. This is an inherent characteristic of wavelet analysis. In the present research the modal parameters are estimated using the Gabor expansion and the Gabor spectrogram.

#### **4.3.1 Decouple modes using Gabor analysis**

Figure 4.4 (a) illustrates a free vibration signal obtained from the free vibration of an aluminum cantilever beam. This signal contains three modes at 34.5, 214.4 and 597.5 Hz. Figure 4.4 (b) is the corresponding wavelet scalogram. As the frequency-resolution is less in the high frequency range than that in the low frequency range, the vibration components of the second and third modes are blurred in the scalogram. Even though Lardies has stated that a modified Morlet wavelet can improve the frequency-resolution, it is indeed a compromise because the time-resolution is decreased compared to the original Morlet wavelet. Another problem is that the wavelet scalogram is quadratic, so it cannot be inverted to reconstruct the time signals. Moreover, since Staszewski and Lardies calculated the wavelet transform of analytic signals, the computation complexity is twice that of the

real signal itself. Finally, the instantaneous frequency components of a real signal and its corresponding analytic signal may be very different, particularly in the low frequency range [113].

Unlike the wavelet analysis, the Gabor analysis has a constant time-frequency resolution once the analysis window is determined. Although such resolution may not be optimum at a particular point on the time-frequency plane, the Gabor analysis has a globally optimum time-frequency resolution compared with the wavelet transform, as shown in Figure 4.4 (c) and (d). In addition, in the present research, in order to avoid the problems caused by the analytic signal, instead the analytic signal is calculated after signal reconstruction using the Gabor expansion.

By applying the procedure in Eqs. (4-7) through (4-9) to the Gabor coefficients shown in Fig. 4.4 (c), the three modes can be reconstructed and the loss factor associated with each mode thus can be obtained. Figure 4.5 (a) is the same original Gabor coefficients shown in Fig. 4.4 (c) which is calculated using Eq. (4-7). Three modal responses at 34.5 Hz, 214.4 Hz and 597.5 Hz can be seen clearly. The color intensity in the Gabor coefficient plot represents the displacement magnitude which is displayed in decibels. The noise is distributed in the entire time-frequency domain. By using three time-varying filters, or actually three mask matrices, the three modal responses can be decoupled as shown in Figs. 4.5 (b), (c) and (d). A 1024-point optimal Gaussian window is used to serve as the analysis and synthesis functions in this calculation. The three decoupled modes thus can be reconstructed using Eq. (4-9). Figure 4.6 illustrates the reconstructed waveforms and their spectra. It is seen that the property of the signal is improved significantly and the noise is dramatically reduced. Since each reconstructed

waveform becomes a single-mode signal, the natural frequency, magnitude, phase and damping ratio can also be extracted easily.

Figure 4.4 (d) illustrates the Gabor spectrogram of the same signal shown in Fig. 4.4 (a). The energy distribution of the three modes is clearly seen in the spectrogram. From this the natural frequencies, damping ratios and magnitude relationships between these modes can be extracted. However, since the phase information is lost, time histories cannot be reconstructed from the spectrogram.

### 4.3.1 Damping calculation

The free response of an underdamped single-degree-of-freedom (DOF) system due to an impact excitation is given by

$$y(t) = Ae^{-\zeta\omega_n t} \cos(\omega_d t - \phi), \quad (4-13)$$

where  $\zeta$  is the damping ratio,  $\omega_n$  is the undamped natural angular frequency and the damped natural angular frequency  $\omega_d$  is

$$\omega_d = \omega_n \sqrt{1 - \zeta^2}. \quad (4-14)$$

For a small value of damping coefficient  $\zeta$ ,  $\omega_d \approx \omega_n$ . The damping ratio can be calculated by obtaining the envelope. The traditional decay rate method in which the ratio of successive peak amplitudes is measured is very sensitive to noise. Another approach to obtain the envelope is to compute the analytic signal by using the Hilbert transform.

For a given real signal  $y(t)$ , its analytic signal  $y_a(t)$  is

$$y_a(t) = y(t) + jH\{y(t)\}, \quad (4-15)$$

where the subscript  $a$  stands for analytic, and the Hilbert transform of  $y(t)$  is defined as

$$H\{y(t)\} = -\frac{1}{\pi} \int \frac{y(\tau)}{t-\tau} d\tau . \quad (4-16)$$

Using Parseval's formula, we can show that the Fourier transform of  $H\{y(t)\}$  is

$$H(\omega) = -j \operatorname{sgn}(\omega) Y(\omega) , \quad (4-17)$$

where  $\operatorname{sgn}(\omega)$  is a sign function, and  $Y(\omega)$  is the Fourier transform of  $y(t)$ . So the Hilbert transform can be easily realized by taking the fast Fourier transform (FFT) of  $y(t)$ . Then the magnitude of the vector  $y_a(t)$  is the envelope of the signal  $y(t)$ . The damping ratio  $\zeta$  associated with each mode can be evaluated by exponential curve fitting from

$$\zeta = -\frac{\Pi_e}{2\pi f} , \quad (4-18)$$

where  $\Pi_e$  is the power of the best exponential fit, and  $f$  is the natural frequency extracted from the reconstructed signal.

### 4.3.2 Simulations

In order to ensure that the method introduced above result in accurate damping values, the following simulation was carried out. Figure 4.7 (a) illustrates a simulated free vibration signal obtained using Eq. (4-19):

$$y(t) = e^{-0.01 \cdot 2\pi \cdot 200t} \sin(2\pi \cdot 200t) + 0.85e^{-0.008 \cdot 2\pi \cdot 350t} \sin(2\pi \cdot 350t) + 0.6 + n(t) . \quad (4-19)$$

There are two damped sinusoids, 200 Hz and 350 Hz. Their damping ratios are chosen to be 0.01 and 0.008, respectively. The noise level  $n(t)$  is 0.1. The sampling rate is 1000 Hz and the data length is 300 points. Figure 4.7 (b) shows the Gabor coefficients.

By using the Gabor analysis-based time-varying filters, the two simulated modes can be separated and reconstructed, as shown in Figs. 4.7 (c) and (d). Figures 4.7 (e) and (f) show the envelopes selected from the decay parts and the corresponding best exponential fits. The results and the mean squared errors (MSE) are listed in Table 4.2. The numbers in brackets are the relative errors.

If one is only interested in the damping, and reconstruction is not necessary, the Gabor spectrogram can also be utilized. Figure 4.8 (a) illustrates the same signal simulated by Eq. (4-19). Figure 4.8 (b) is the Gabor spectrogram calculated using Eq. (4-10). The two modes, their frequencies, and the difference between their magnitudes and damping can be distinguished in this figure. By setting the frequency zoom, we can easily decouple the modes as shown in Figs. 4.8 (c) and (d).

If the ridges are extracted from the two 3-D plots, then the exponential decay curves are recovered again. Reference [124] describes several algorithms for ridge detection. An advanced wavelet application, the so-called ridgelet, has been developed in recent years [125]. In this research, it is quite simple to recover the decaying vibration signals because the ridges are concentrated at fixed frequencies.

Unlike the exponential envelope of the signal which can be reconstructed using the Gabor expansion, the modulation term in Eq. (4-13) is squared because the Gabor spectrogram calculated using Eq. (4-10) is quadratic. So the term should be divided once more by two compared with Equation (4-18). Then the damping ratio is

$$\zeta = -\frac{\Pi_{es}}{4\pi f}, \quad (4-20)$$

where  $\Pi_{es}$  represents the exponential power of the ridge in the Gabor spectrogram. The



results are listed in Table 4.3. The numbers in brackets are the relative errors. On comparing Tables 4.2 and 4.3, it can be seen that the error of the curve fitting obtained with the Gabor spectrogram method is smaller than that obtained with the Gabor expansion method.

### 4.3.3 Comparison with FFT-based technique

In above analysis, it is basically assumed that the system is linear. So the natural frequencies are constant. In another words, the modal components can be decoupled directly from the FFT. Then, what is the advantage of using the time-frequency transform? In this section we shall compare the decoupling/reconstruction approaches using the FFT and the Gabor expansion.

Figure 4.9 shows the real part and the imaginary part of the original FFT coefficients of the signal given in Fig. 4.4 (a). Note that the FFT,  $Y(\omega)$ , is a complex sequence. The first half of  $Y(\omega)$  represents the “negative” frequencies and the second half represents the positive frequencies.

According to the bandwidth of each component, analogous to the 2-D mask matrix used in Eq. (4-8), a 1-D mask array can be applied to the complex FFT. The FFT coefficients in the passband are preserved and all of the other coefficients outside of the band are set to be zero. Now that the original FFT contains both positive and “negative” frequency components, there are two passbands in the mask array. So the mask array actually contains two symmetric rectangular windows. Then the time signal of a particular component can be reconstructed using the inverse FFT of the modified FFT coefficients. Figure 4.10 compares the envelopes of the three response modes

reconstructed using the FFT method and the Gabor expansion method. It can be seen that the envelopes computed using the FFT method are noisier than their counterparts computed using the Gabor expansion method. When the magnitude of each free vibration mode is decreasing exponentially with time, the signal-to-noise ratio is lower. So the bandwidth of the signal is relatively decreasing in the time domain. However, the bandwidth of the 1-D mask array used in the FFT method is constant once the passband is determined. On the other hand, the bandwidth of the 2-D mask matrix used in the Gabor expansion method can vary according to the change in magnitude of the signal so that the bandwidth of the time-varying filter is optimal in the time-frequency space.

The signal-to-noise-ratio (SNR) is defined in terms of the mean-square values as

$$\text{SNR} = 10 \log_{10} \frac{E\{s[k]^2\}}{E\{n[k]^2\}} = 20 \log_{10} \frac{\|s\|_2}{\|n\|_2}, \quad (4-21)$$

where  $s$  and  $n$  represent the exact free vibration signal and noise in the reconstructed signal,  $E\{\bullet\}$  is the expected value, and  $\|\bullet\|_2$  denotes the 2-norm of a vector defined by  $\|x\|_2 = \sqrt{\sum_k x_k^2}$ . Table 4.4 compares the SNRs of the reconstructed displacement components using the FFT and the Gabor expansion methods.

#### 4.4 Modal Testing using Gabor Transform

As mentioned at the beginning of this chapter, natural frequency, modal damping and magnitude are three elementary parameters in the modal analysis. A new modal testing method based on the Gabor analysis was developed for free vibration signals without excitation information. Two damping calculation methods have been presented in

the previous section. The natural frequency and mode shape calculations are introduced next.

The natural frequency of each reconstructed signal can be calculated easily using the FFT. Figure 4.6 (d) shows the spectra of the three reconstructed modes. The natural frequencies correspond to the three peaks in the spectra.

For an  $N$ -degree-of-freedom (DOF) damped system, the general equations of motion written in matrix form are

$$[M]\{\ddot{y}\} + [C]\{\dot{y}\} + [K]\{y\} = \{f(t)\}, \quad (4-22)$$

where  $[M]$ ,  $[C]$  and  $[K]$  are the mass, damping and stiffness matrices, and  $\{f(t)\}$  is the force vector. For a passive system, the  $N \times N$  matrices  $[M]$ ,  $[C]$  and  $[K]$  are symmetric and positive definite. Then the mode shapes are identical to the mode shapes for the undamped system [126].

For an undamped system, the natural frequencies are the eigenvalues of the matrix  $[M]^{-1}[K]$ , and the mode shape corresponding to one natural frequency is the eigenvalue which satisfies

$$[M]^{-1}[K]\{y_i\} = \omega_i^2 \{y_i\}, \quad (4-23)$$

where  $\omega_i$  is the  $i$ -th natural frequency, and the mode shape  $\{y_i\}$  is an  $N$ -dimensional column vector

$$\{y_i\} = [y_{i1}, y_{i2}, \dots, y_{iN}]^T. \quad (4-24)$$

Here the subscripts 1 through  $N$  indicate the grid points which are evenly distributed on the  $N$ -DOFs structure.

The absolute values of these elements are the magnitudes of the vibration at the  $N$  grid points. The signs indicate the phase differences. The same sign for two elements means that the vibration at these two points is in phase. Different signs mean that the two points are vibrating  $180^\circ$  out-of-phase. Although the actual values of the vector elements are arbitrary, the ratios between them are unique. Therefore, even without the information of excitation, the mode shapes can be obtained by simply measuring the magnitudes and phase angles of the responses at the grid points. We can choose one of the grid points as the reference point and compare the magnitudes and phase angles measured at other points to those measured at the reference point for all the modes of interest.

After the modes in a vibration signal measured at a point are decoupled and reconstructed, the magnitude and the phase angle for each mode can be obtained using the FFT. Fourier transformation is a complex process, resulting in both magnitude and phase information.

Let  $p(t) = Ae^{-\zeta\omega_n t}$  and  $q(t) = \cos(\omega_d t - \phi)$ . Then Eq. (4-13) becomes  $y(t) = p(t) \cdot q(t)$ . The single-sided spectrum of the pure cosine function  $q(t)$  is  $Q(\omega) = 2\pi e^{-j\phi} \delta(\omega_d)$ . The Fourier transform of  $p(t)$  is

$$P(\omega) = \int_0^{\infty} Ae^{-\zeta\omega_n t} e^{-j\omega t} dt = A \int_0^{\infty} e^{-(\zeta\omega_n + j\omega)t} dt = -\frac{A}{j\omega + \zeta\omega_n} e^{-(\zeta\omega_n + j\omega)t} \Big|_0^{\infty} = \frac{A}{j\omega + \zeta\omega_n}. \quad (4-25)$$

Using the convolution property of the Fourier transform,

$$\begin{aligned} Y(\omega) &= P(\omega) * Q(\omega) = \frac{2\pi A e^{-j\phi}}{j\omega_d + \zeta\omega_n} = \frac{2\pi A e^{-j\phi}}{(\zeta\omega_n)^2 + (\omega_d)^2} \cdot (\zeta\omega_n - j\omega_d) \\ &= \frac{2\pi A}{(\omega_d)^2} [(\zeta\omega_n \cos \phi - \omega_d \sin \phi) - j(\omega_d \cos \phi + \zeta\omega_n \sin \phi)] \quad (4-26) \\ &= |Y(\omega)| \cdot e^{j\Phi} \end{aligned}$$

It is easy to show that the calculated magnitude  $|Y(\omega)|$  and phase angle  $\Phi$  of a single-mode free vibration at its natural frequency  $\omega_n$  is

$$|Y(\omega)| = \frac{2\pi A}{\omega_n^2}, \text{ and } \Phi = 90 - \phi. \quad (4-27)$$

Then the mode shape can be obtained by the magnitude ratios and phase differences which are

$$\frac{|y_{i1}|}{|y_{im}|} = \frac{A_{i1}}{A_{im}} = \frac{|Y_{i1}(\omega)|}{|Y_{im}(\omega)|}, \quad m = 2, \dots, N, \quad (4-28)$$

and

$$\phi_{i1} - \phi_{im} = \Phi_{i1} - \Phi_{im}, \quad m = 2, \dots, N. \quad (4-29)$$

## 4.5 Experiments

### 4.5.1 Experimental setup

A three-DOF model of an aluminum cantilever beam was studied experimentally as shown in Fig. 4-11. For a cantilever beam, the first three natural frequencies are

$$f_{1,2,3} = (1.194^2, 2.988^2, 5^2)\pi \cdot \kappa \cdot c_l / 8L^2, \quad (4-30)$$

where  $L$  is the length of the cantilever beam,  $\kappa$  is the radius of gyration and  $c_l$  is the longitudinal wave speed. The thickness of the cantilever beam is  $t = 6.43$  mm. So  $\kappa = t / \sqrt{12} = 1.86 \times 10^{-3}$  m. And the wave speed in aluminum is 5055 m/s. The theoretical natural frequencies are listed in Table 4.5.

A heavy steel block and two clamps were used to fix the beam at the left end. The

free end, point #1 was selected as the reference point. Two Polytech laser vibrometers were employed to measure the beam responses. Since the reference point and one of the other points must be measured simultaneously, one laser vibrometer was fixed at point 1, and the other one was used to measure the responses at the other two points. A National Instruments PCMCIA 6036E card was used for data acquisition and analysis programs were developed in LabVIEW. The sampling rate was 1500 Hz. Totally 20 measurements were carried out at points #2 and #3, ten measurements at each point. Each data file also contains the free response acquired at the reference point.

#### **4.5.2 Natural frequency and mode shape**

Figure 4.4 shows one of the typical measurements. Based on the Gabor transform procedure in Eqs. (4-7) to (4-9), the modes which were overlapping in one free vibration signal were separated and reconstructed. Then the natural frequency, magnitude and phase angle associated with each mode were extracted using the FFT. Consequently, the magnitude ratios and phase differences at different grid points are determined using Eqs. (4-28) and (4-29). Table 4.5 lists the theoretical and calculated values. The measured natural frequencies are less than the theoretical values due to the non-ideal boundary conditions. However, the magnitude ratios and phase differences are quite accurate. Figure 4.12 compares the theoretical and measured mode shapes for the three modes.

#### **4.5.3 Damping ratio**

In the 20 measurement data files there are altogether 40 time histories. Both the Gabor expansion method and the Gabor spectrogram method were used to calculate the

damping ratios. Table 4.6 presents the averages. The numbers in the brackets are the corresponding standard deviations. The standard deviation of the damping of the third mode is the highest because it is relatively difficult to excite the higher mode into free vibration. Since the vibration magnitude of the third mode is the smallest, the signal-to-noise ratio of the third mode is the lowest.

<b>STD of <math>n[i]</math></b>	0.05	0.1	0.2	0.3	0.4
<b>detected <math>f_n</math></b>	199.84 (0.08%)	199.80 (0.1%)	199.78 (0.11%)	199.76 (0.12%)	199.75 (0.125%)
<b>detected <math>\zeta</math></b>	1.994 (0.3%)	1.989 (0.55%)	1.976 (1.2%)	1.960 (2%)	1.942 (2.9%)

Table 4.1. Detected natural frequencies and damping ratios for simulated signals with different noise level.

<b>Mode</b>	<b>Damping ratio</b>	<b>Calculated damping ratio</b>	<b>MSE of exponential curve fitting</b>
first	0.01	0.009998 (0.020%)	$2.46 \times 10^{-4}$
second	0.008	0.00797 (0.375%)	$1.14 \times 10^{-4}$

Table 4.2. Damping ratios of two-mode decay signal calculated using Gabor expansion.



<b>Mode</b>	<b>Damping ratio</b>	<b>Calculated damping ratio</b>	<b>MSE of exponential curve fitting</b>
first	0.01	0.0101 (1.00%)	$3.00 \times 10^{-9}$
second	0.008	0.00797 (0.375%)	$6.45 \times 10^{-10}$

Table 4.3. Damping results calculated using the Gabor spectrogram method.

<b>Mode</b>	<b>FFT method</b>	<b>Gabor Expansion method</b>
first	17.8 dB	22.4 dB
second	13.8 dB	20.3 dB
third	12.6 dB	12.8 dB

Table 4.4. Comparison of the SNRs of the signals reconstructed using the FFT method and the Gabor expansion method

		<b>Theoretical Value</b>	<b>Calculated Value</b>
Fundamental Mode	Frequency (Hz)	35.788	34.610 (-3.3%)
	$A_{11}/A_{12}$	1.792	1.780 (-0.70%)
	$A_{11}/A_{13}$	5.968	5.746 (-3.69%)
	$\phi_{11} - \phi_{12}$	0°	0.09°
	$\phi_{11} - \phi_{13}$	0°	0.17°
Second Mode	Frequency (Hz)	224.398	214.164 (-4.56%)
	$A_{21}/A_{22}$	2.175	2.390 (9.98%)
	$A_{21}/A_{23}$	1.577	1.583 (0.34%)
	$\phi_{21} - \phi_{22}$	180°	178.92°
	$\phi_{21} - \phi_{23}$	180°	181.27°
Third Mode	Frequency (Hz)	628.265	597.569 (-4.89%)
	$A_{31}/A_{32}$	1.365	1.383 (1.36%)
	$A_{31}/A_{33}$	1.385	1.366 (-1.37%)
	$\phi_{31} - \phi_{32}$	180°	182.49°
	$\phi_{31} - \phi_{33}$	0°	3.86°

Table 4.5. Error analysis of the new modal testing method.

<b>Mode</b>	<b>Gabor expansion method</b>	<b>Gabor spectrogram method</b>
Fundamental	0.373% ( $2.9 \times 10^{-4}$ )	0.367% ( $1.3 \times 10^{-4}$ )
Second	0.108% ( $2.3 \times 10^{-5}$ )	0.109% ( $2.7 \times 10^{-5}$ )
Third	0.085% ( $8.6 \times 10^{-4}$ )	0.085% ( $6.8 \times 10^{-4}$ )

Table 4.6. Damping ratios calculated using the Gabor expansion method and the Gabor spectrogram method.

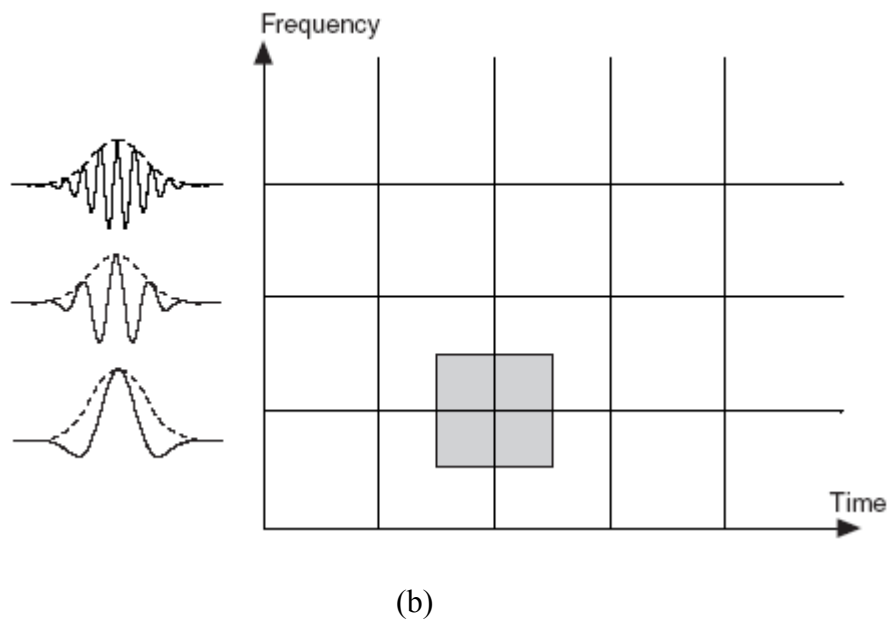
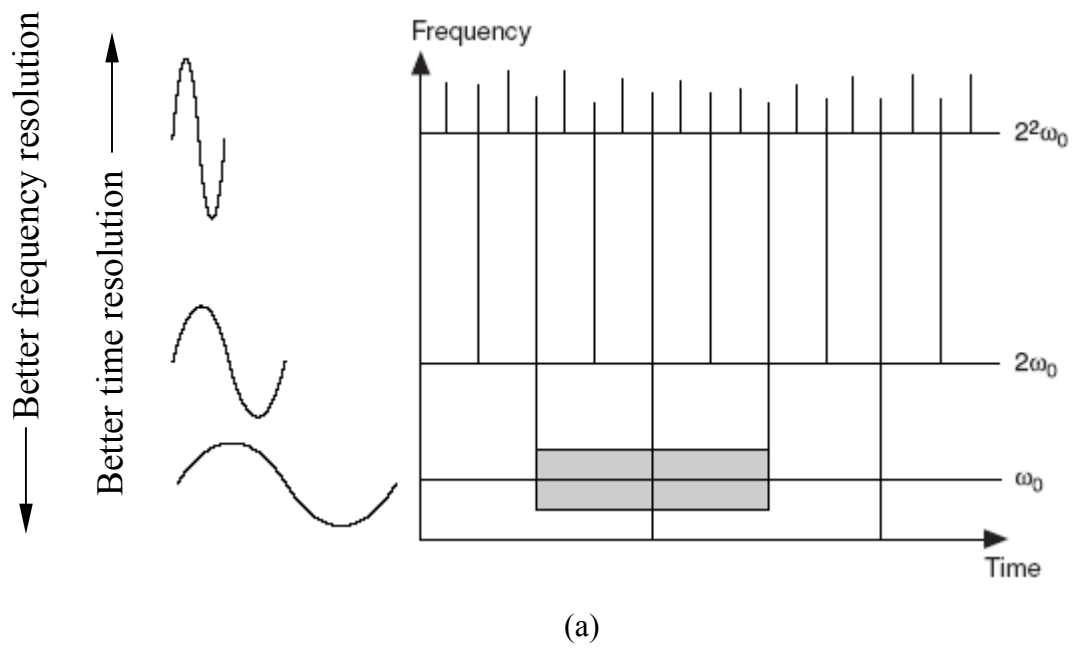


Figure 4.1. Sampling grids for (a) wavelet transform and (b) Gabor transform.

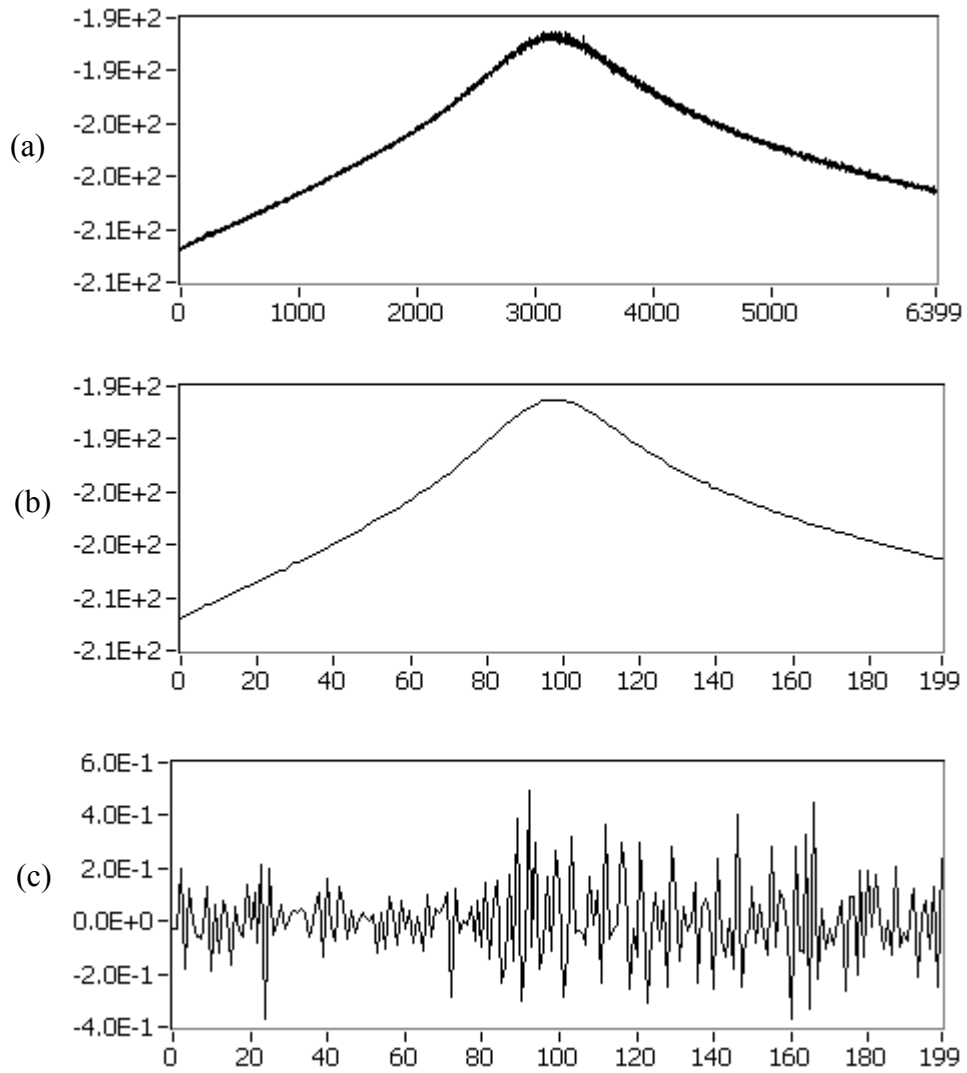


Figure 4.2. (a) An accelerance FRF measured from a sandwich beam.

(b) Outline coefficient from the lowpass filter branch of a five-order standard DWT.

(c) Detail coefficients from the high-pass filter branch of a five-order standard DWT.

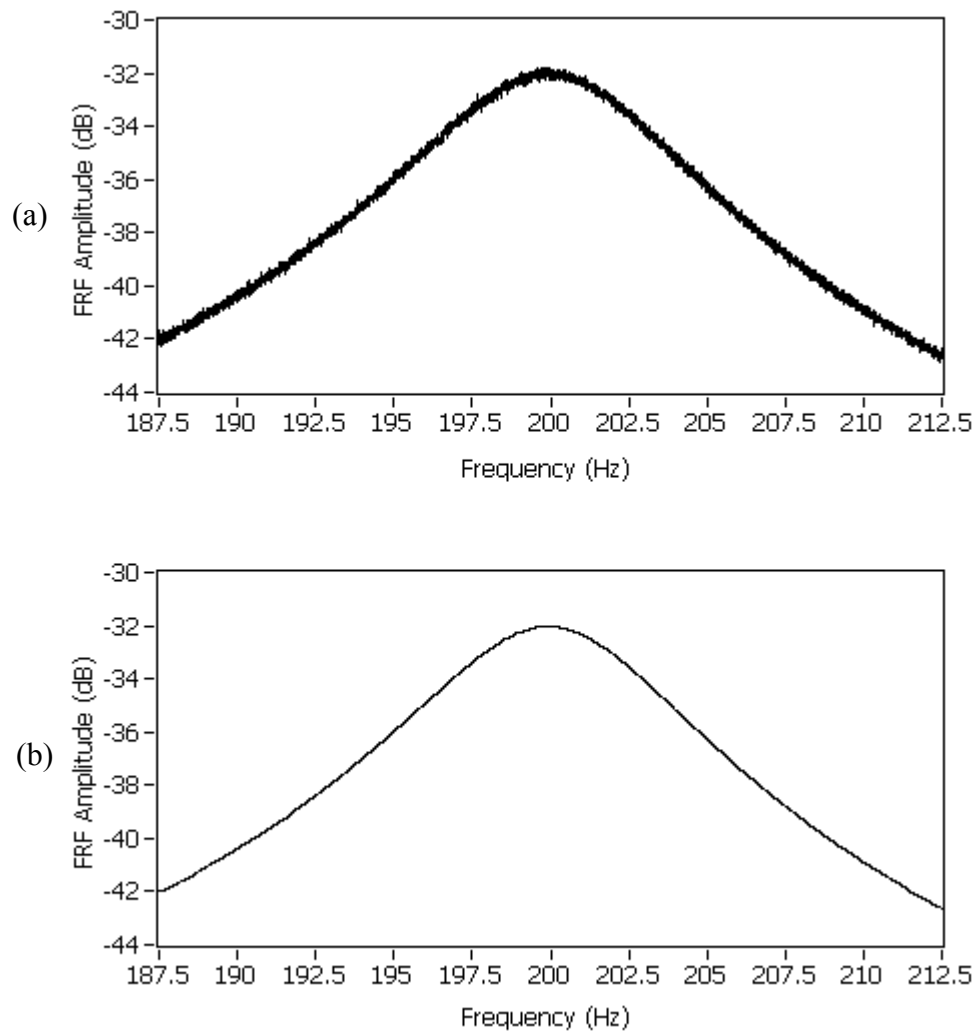


Figure 4.3. (a) A simulated noisy accelerance FRF with natural frequency of 200 Hz and damping ratio of 2%. (b) Denoising result from a five-order undecimated wavelet transform with the calculated natural frequency of 199.79 Hz and damping ratio 1.99%.

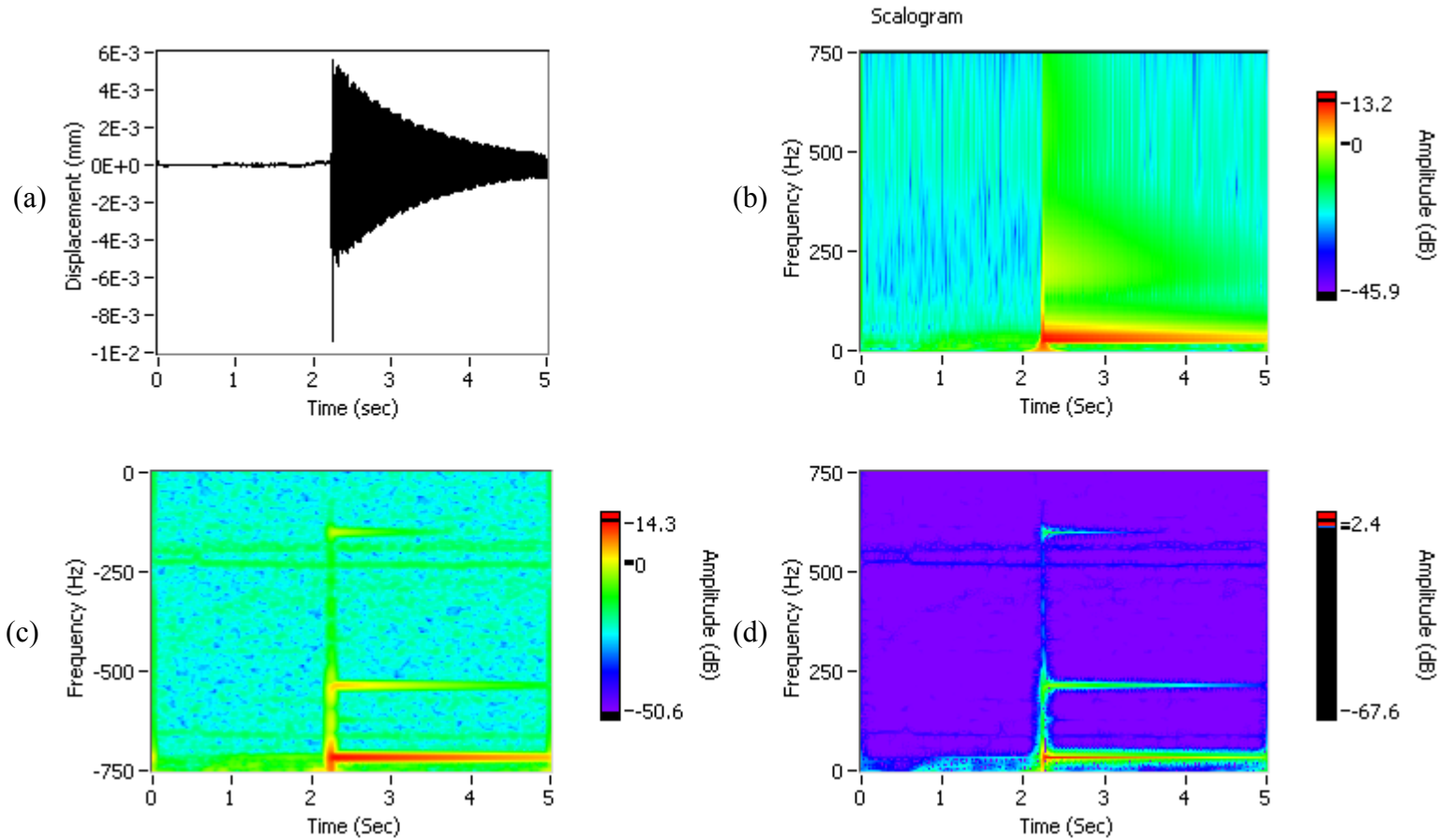


Figure 4.4. (a) A free vibration signal measured from an aluminum cantilever beam. (b) The wavelet scalogram.

(c) The original Gabor coefficients. (d) The Gabor spectrogram.

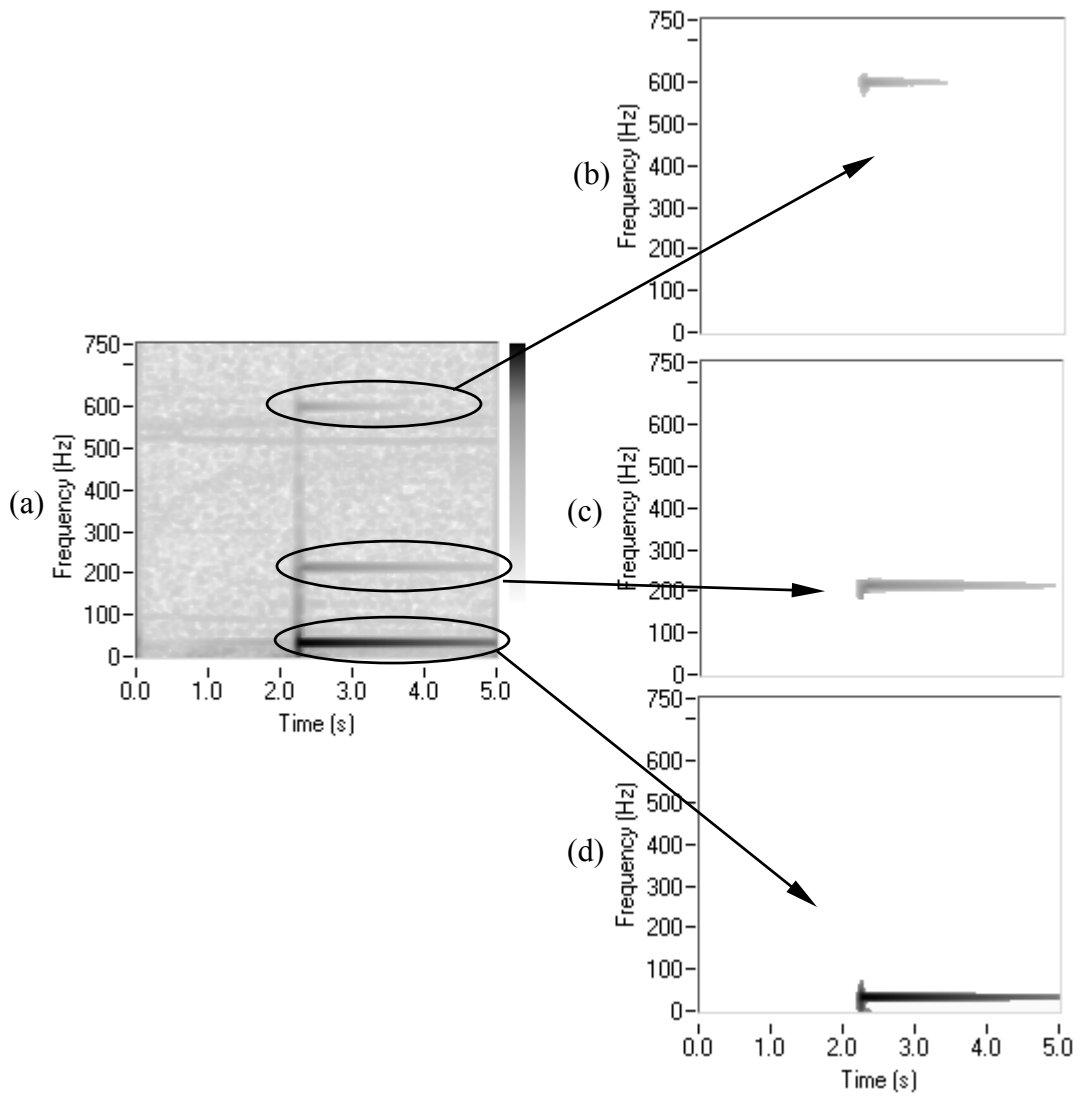


Figure 4.5. (a) The original Gabor coefficients of signal shown in Fig 4.4 (a).  
 (b) (c) (d) The modified Gabor coefficients of three modes by using three mask matrices.

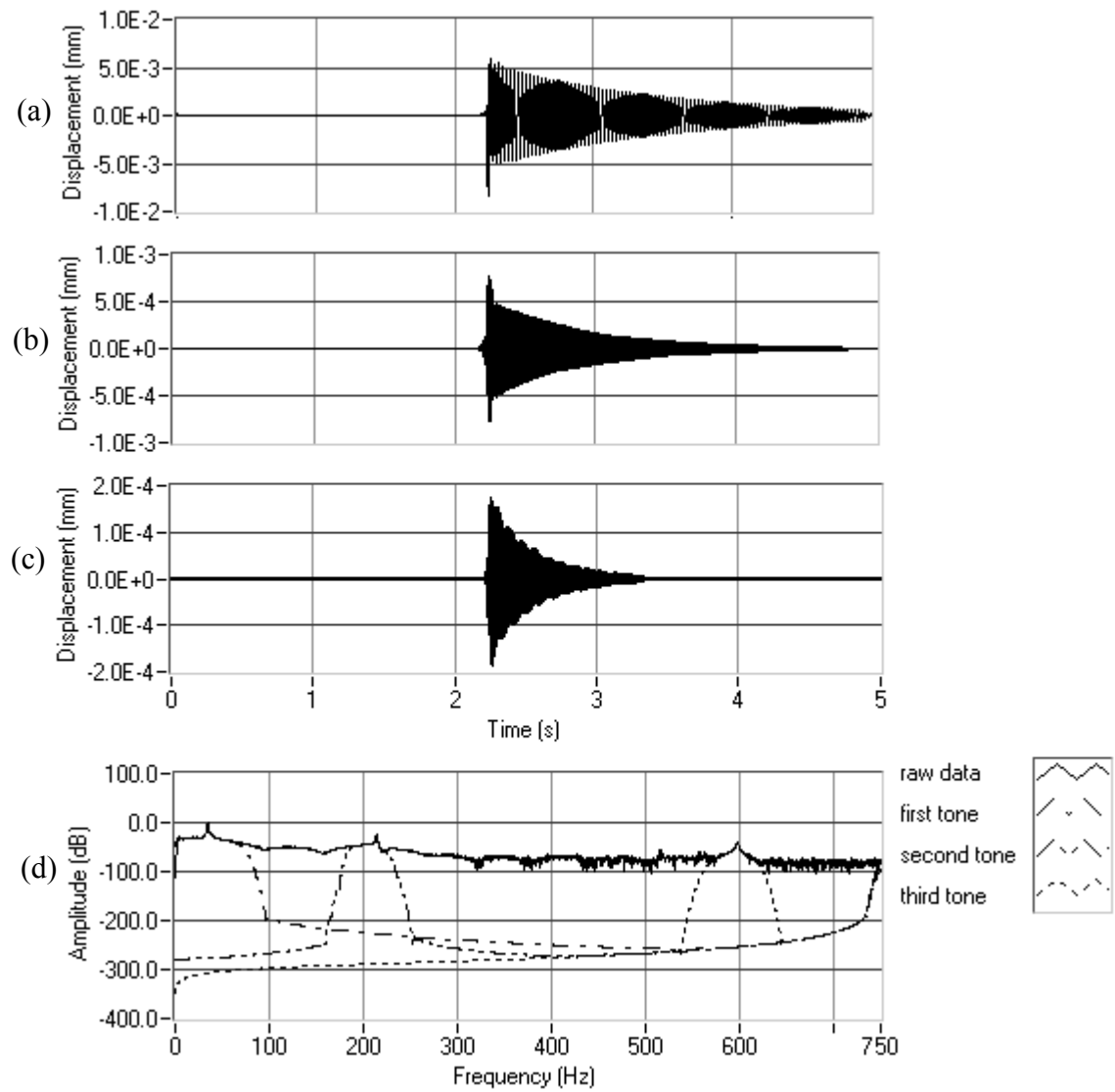


Figure 4.6. The decoupled modal responses using Gabor expansion.

(a) The first mode, (b) the second mode, (c) the third mode, and

(d) spectra of the three reconstructed signals.



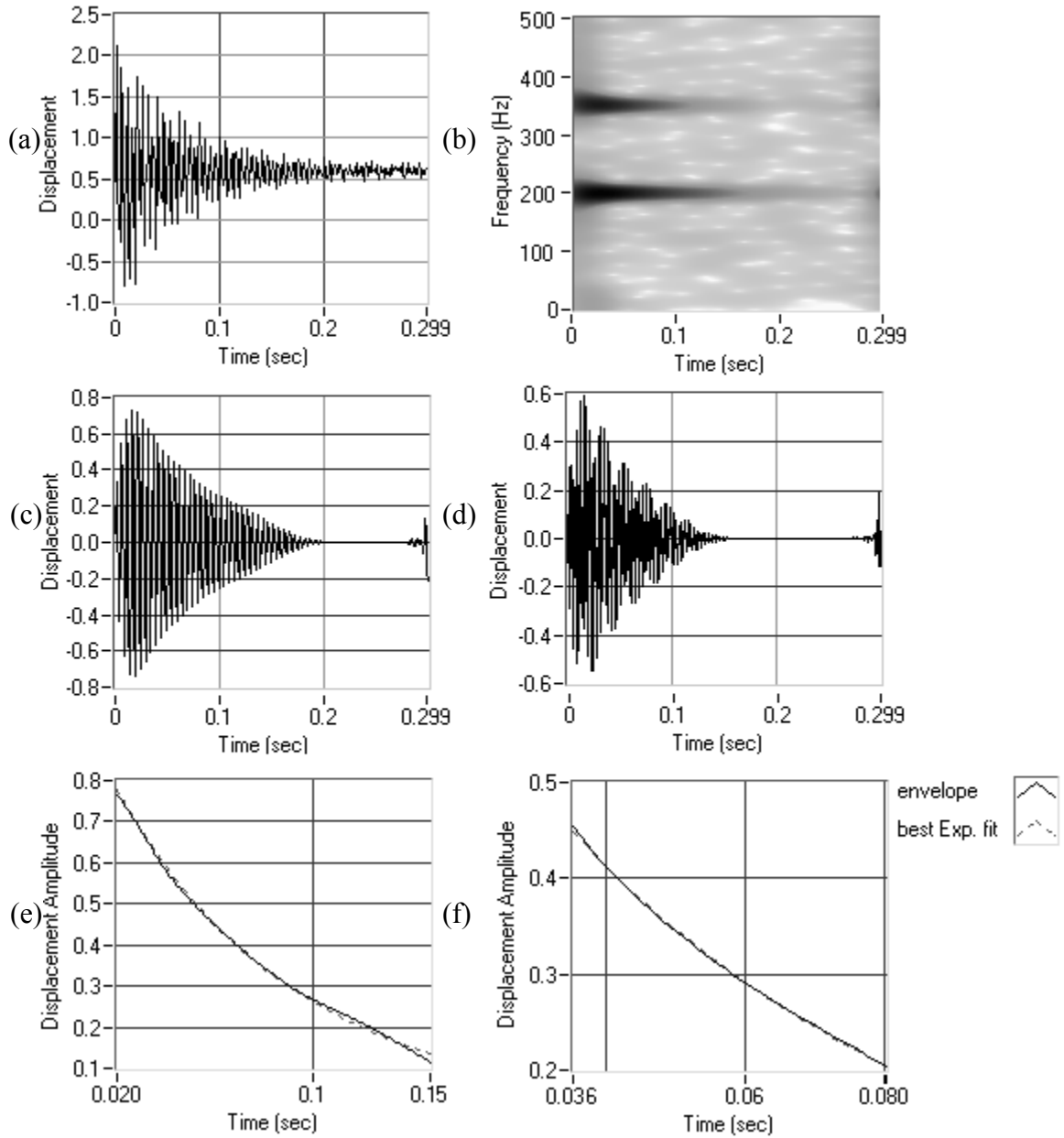


Figure 4.7. Damping calculation simulation using the Gabor transform.

- (a) A simulated free vibration signal, (b) the original Gabor coefficients of this signal, (c) and (d) the reconstructed modal responses, and (e) and (f) envelopes established using the Hilbert transform and the best exponential fits.

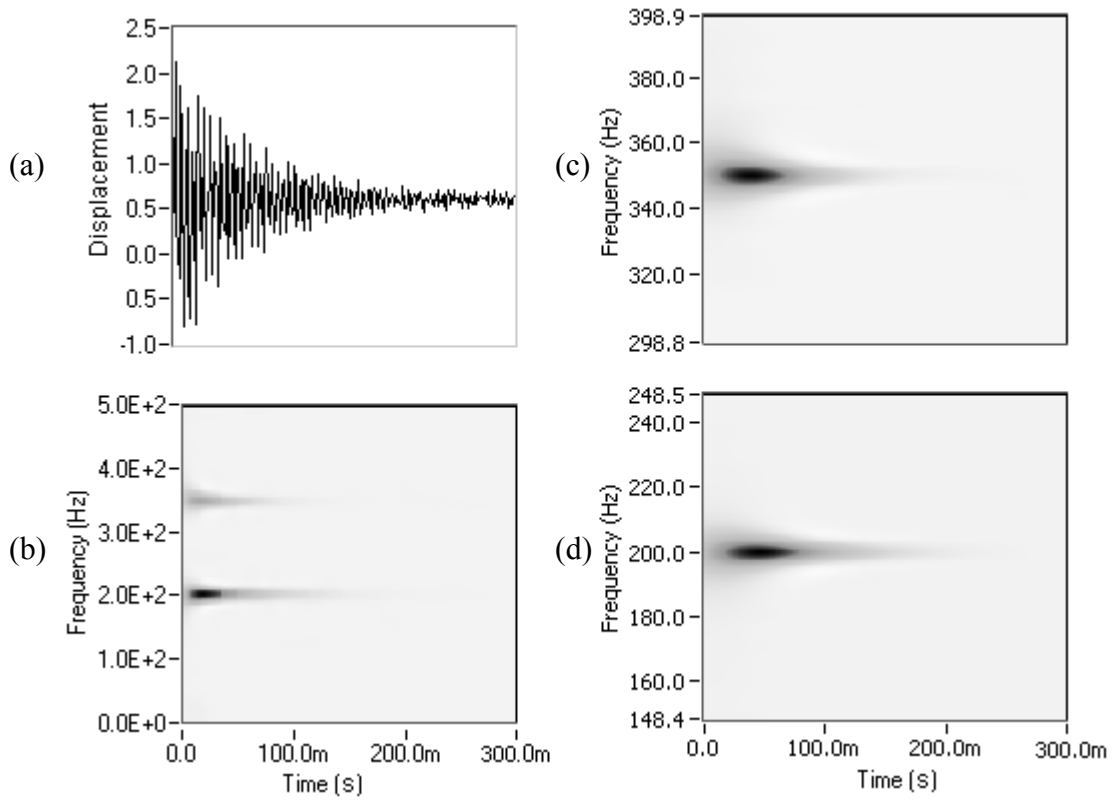


Figure 4.8. Damping calculation simulation using the Gabor spectrogram.

- (a) A simulated free vibration signal, (b) the Gabor spectrogram,  
(c) and (d) the two vibration modes calculated using zoom Gabor spectrogram.

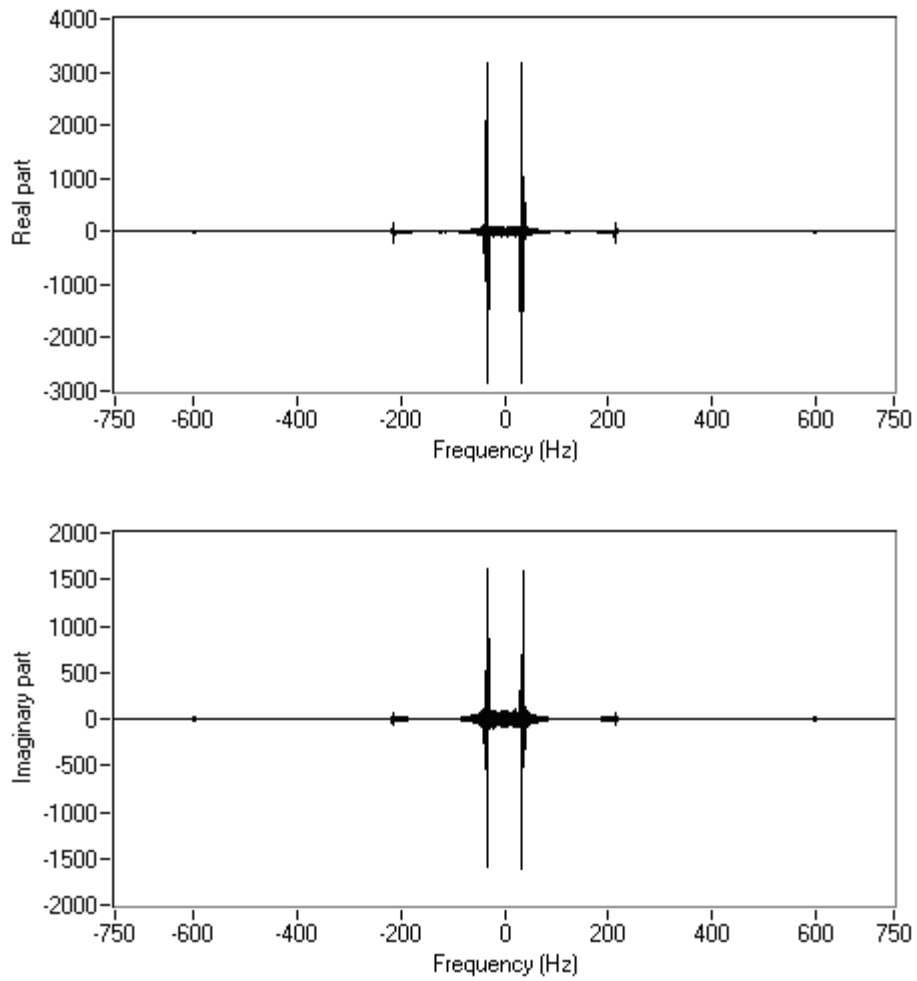


Figure 4.9. The original complex FFT of a free vibration signal containing three modes.

(a) Real part, (b) imaginary part.

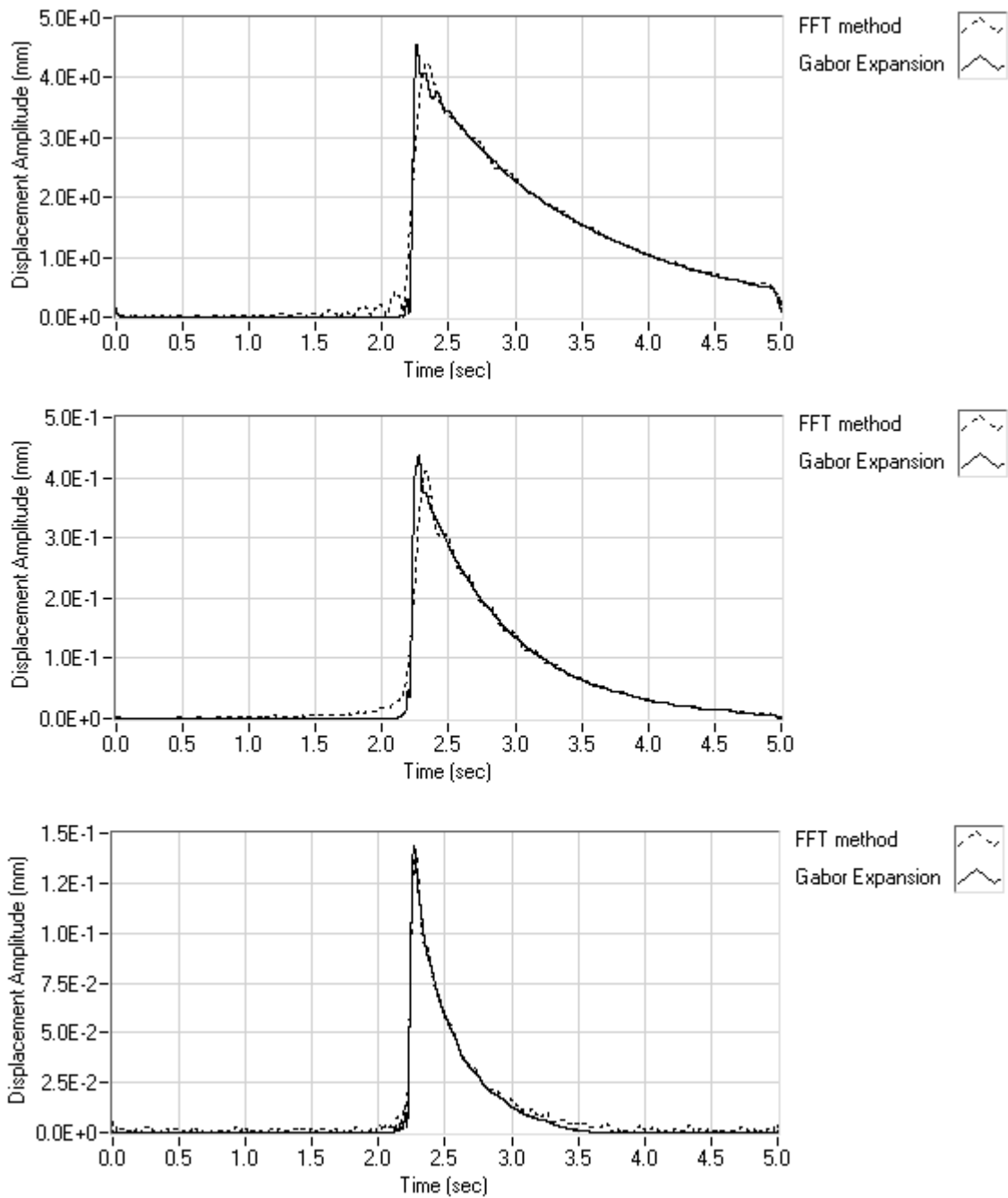


Figure 4.10. Comparison of the envelopes of the displacement components reconstructed using the FFT and Gabor expansion methods.

(a) First mode, (b) second mode, (c) third mode.

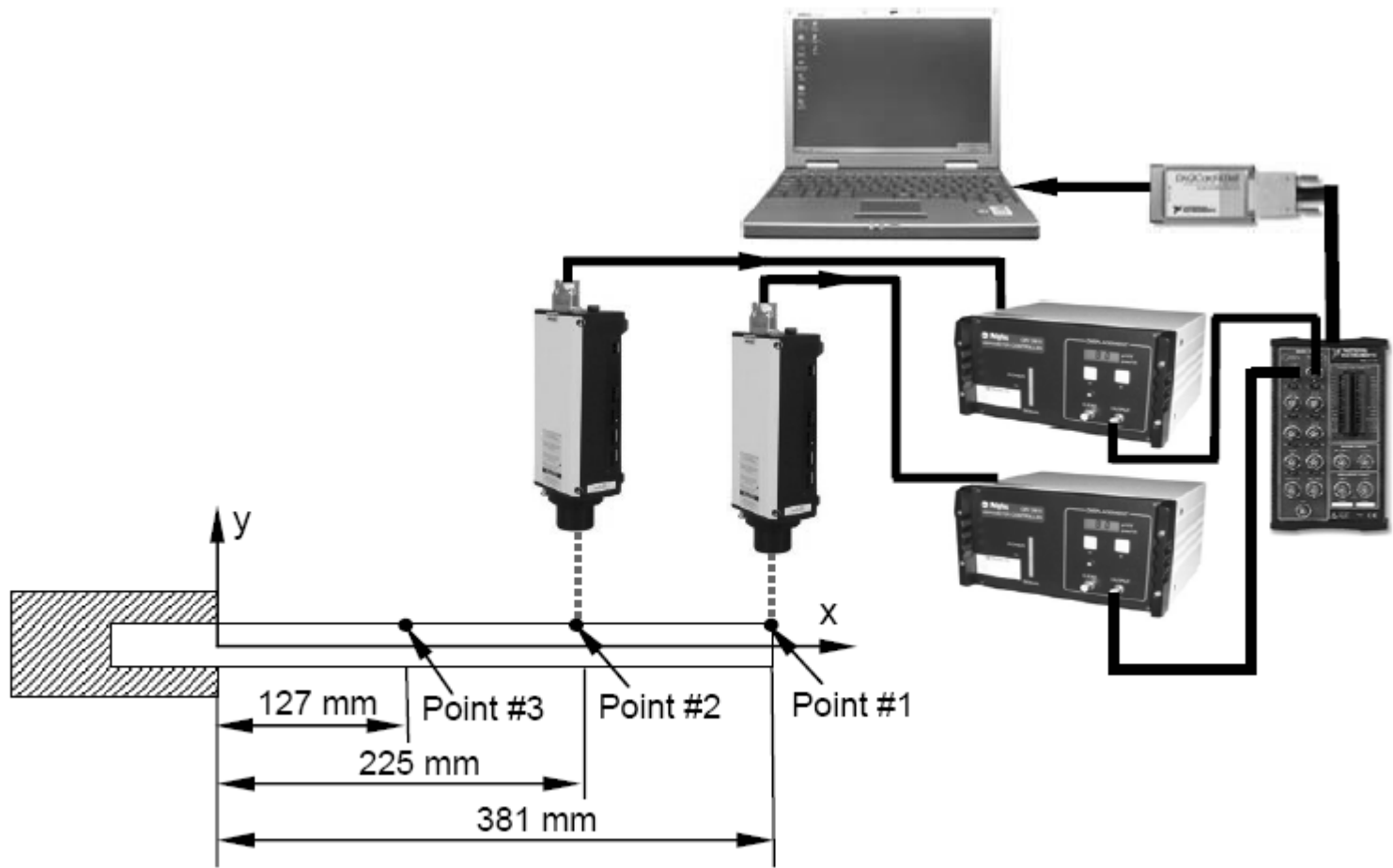


Figure 4.11. Experimental setup for modal testing.

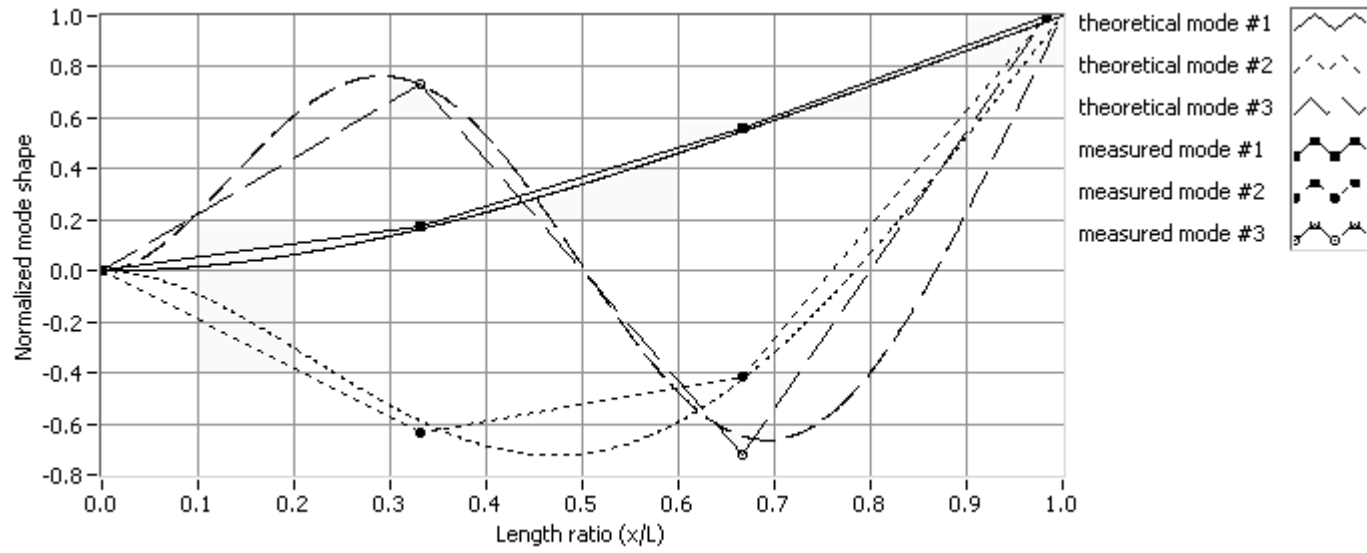


Figure 4.12. Comparison of the theoretical and measured mode shapes.

## CHAPTER 5 ANALYSIS OF SOUND TRANSMISSION THROUGH SANDWICH PANELS

Sound transmission loss (TL), or referred to as the sound reduction index, of a panel is the difference between the incident sound power level and the transmitted sound power level for a specified frequency or frequency band. This number indicates the noise insulation capability of the panel. The sound transmission loss is often an important consideration in the analysis and design of partitions or panels separating adjoining spaces in industry, housing and various types of vehicles. It can be described in terms of the panel impedance  $Z$  [127]. For a homogeneous thin panel, if the stiffness and the damping are neglected at low frequencies, the panel impedance depends purely on its surface density. In this case,  $Z = i\omega\rho_s$ , where  $\rho_s$  is the mass per unit area of the panel. In such a simple case, the sound transmission loss is determined by “mass law” which says that the TL increases by 6 dB per octave [128]. However, for a real panel, the TL depends not only on the surface density, but on its bending stiffness, damping loss factor and the orientation of the incident sound waves as well. Due to the coincidence effect, when the free flexural wave speed of the panel  $C_p$ , which increases with frequency, approaches the speed of sound in air, the impedance of the panel to incident sound wave ceases to be mass-like and the TL becomes much less than that given by mass law. The frequency at which the coincidence effect begins to occur is called the critical coincidence frequency

(often known as simply as the critical frequency). For an isotropic homogeneous panel, the critical frequency is given by

$$f_c = \frac{c^2}{2\pi\kappa c_l}, \quad (5-1)$$

where  $c$  is the sound wave speed in air,  $\kappa$  is the radius of gyration of the panel, and  $c_l$  is the speed of longitudinal wave propagating in the panel. Note that  $\kappa = t/\sqrt{12}$  for a rectangular cross-section panel with thickness  $t$ , and  $c_l = \sqrt{E/\rho}$  for a homogeneous material. An intuitive solution is to raise the critical frequency of the panel out of the audio frequency range. However, from Eq. (5-1) we can see this means either reducing the thickness of the panel or reducing the stiffness to density ratio. Unfortunately, in practice, most of the panels must also serve as structural partitions. From an engineering point of view, a reduction in the stiffness to density ratio may degrade the performance of the whole structure in other respects. So improving the sound transmission loss without compromising the stiffness to density ratio is an interesting problem.

This chapter will start with a brief literature review of the sound transmission of sandwich structures. A theoretical prediction of the TL of a three-layer sandwich structure is performed using statistical energy analysis (SEA). Some optimization considerations are presented as well. Experimental results are discussed at the end of the chapter.

## 5.1 Review of the Sound Transmission Loss of Sandwich Panels

Research on the sound transmission loss of sandwich structures can be traced back to 1959. Kurtze and Watters undertook a very early design study of sandwich plates and



analyzed their acoustical behavior [129]. By inserting a soft core between two thin face sheets, the shear waves, which are not dispersion waves, are introduced in a wide middle frequency range. If the shear wave speed is less than the speed of sound in air, the critical frequency is then shifted to higher frequencies, which avoids locating the critical frequency in the range of interest. They derived the impedance of a sandwich plate and the speed of transverse wave propagation through the structure using a circuit analogy. They also designed a periodic wall structure in which bridges are used to connect the face-sheets of the composite. Their experimental results agree with the theoretical estimation of the anti-symmetric motion. However, since they assumed that the core material is incompressible, their model cannot predict the symmetric thickness motion which was studied subsequently by other researchers.

Ford, Lord and Walker assumed instead the polyurethane foam core as compressible material, and they studied both the anti-symmetric (or flexural) and symmetric (or dilatational) modes of vibration [130]. However, as pointed out later by Smolenski and Krokosky, the energy expression used in [130] is incorrect. Smolenski and Krokosky corrected the energy expression and investigated the influence of the core material properties on the critical frequency due to the dilatation mode [131]. They also measured the TL of two panels with different configurations and explained the discrepancies between the predicted and experimental results.

Dym, Lang and their colleagues conducted a series of researches on the sound transmission of sandwich plates [132-136]. Dym and Lang derived five equations of motion for sandwich panels with identical face sheets in [133]. The five equations are decoupled into two sets which represent the symmetric and anti-symmetric vibration

modes. They also calculated the impedance for both the symmetric and anti-symmetric cases, thus obtaining the TL as well. Note that an error in [132] was corrected later in [134]. Lang and Dym presented optimal TL properties for sandwich panels using indirect and direct methods [133]. They reported that an increase in the stiffness of the core would eliminate the coincidence effect caused by the symmetric vibration mode. However, the anti-symmetric coincidence effect would still occur at a low frequency. Dym and Lang later expanded their theoretical model to include infinite sandwich panels with unequal isotropic face sheets and an elastic orthotropic core [135]. They assumed the presence of damping in both the face sheets and the core.

Ordubadi and Lyon studied the effect of orthotropy on the sound transmission through plywood panels [137]. By assuming that the bending stiffness and phase wave speed change gradually from the stiff direction to the soft direction of the orthotropic panels, they presented an analytical expression for the TL of such panels.

Narayanan and Shanbhag used Mead's [41] equations of motion of viscoelastically damped sandwich panels to study the sound transmission characteristics [139]. Their parametric study shows that the transmission loss is more sensitive to the variation of the core shear parameter than to the change of other parameters. However, since Mead's model only considered flexural vibration modes, Narayanan and Shanbhag's analysis did not include the dilatational modes. They only calculated the TL at some particular angles of incidence rather than integrating the results to obtain the field incident representation.

Moore and Lyon developed analytical models for sandwich panels with isotropic and orthotropic cores [140]. They considered both the flexural and dilatational modes. This analysis describes the propagation of shear and dilatational waves within the

sandwich panel cores and their interaction with face-sheets in the transmission of sound through the panels. For dilatational modes, coincidence occurs near the conventional double wall resonance frequency, which is determined by the stiffness of the core and the mass of the face sheets. They further developed a design approach which lowers the double wall resonance frequency to below the frequency band of interest, and shifts the critical frequency to higher frequencies.

Wang, Sokolinsky, Rajaram and Nutt derived expressions to predict the TL in infinitely wide sandwich panels using two models, (1) the consistent high-order approach, and (2) the two-parameter foundation model [141]. In both the models, the TL is calculated using a decoupled equation which represent the symmetric and anti-symmetric motions. They compared their numerical prediction with experimental results. The consistent high-order approach is more accurate, while the two-parameter foundation model is more convenient.

The TL of multi-layer panels has also been analyzed by some other researchers. Guyander and Lesueur studied the equation of motion, the modal density and the TL of viscoelastic and orthotropic multi-layer plates [142-144]. They used both plane wave and reverberation sound excitations to study the TL. Panneton and Atalla developed a three-dimensional finite element model to predict the TL through a multi-layer system made of elastic, acoustic and porous-elastic media [145]. The three-dimensional Biot theory was used to model the porous-elastic medium. However, at low frequencies (lower than 100 Hz, and sometimes even 200 Hz), the predicted behavior is completely incorrect. For higher frequencies, the model is only useful for unbonded plates. Kurra and Arditi used the ASTM and ISO standards to measure the sound transmission loss of multi-layered

plates [146,147]. Uris and Estelles studied the sound transmission of multi-layered sandwich plates using different configurations of polyurethane and polystyrene layers [148]. They found that multi-layered sandwich plates possess better sound transmission loss, and the coincidence effect is not as obvious as with three-layer sandwich plates. These observations are actually because multi-layered plates are much thicker and the surface densities help to increase the sound transmission loss.

## 5.2 Prediction of Sound Transmission through Sandwich Panels using SEA

As discussed in Chapter 2, SEA method was first developed by Lyon and others in the 1960's. Crocker and Price used SEA to predict the sound transmission loss of isotropic single-layered panels [15]. The same theoretical model is used for the sandwich panels.

The subsystems and energy flow relationship are illustrated schematically in Fig. 5.1. The subscripts represent the subsystem number. The source room and the receiving room are the first and third subsystems, and the panel under study is the second subsystem. Here the two rooms are assumed to be reverberant. This means that the sound pressure level measured in each room is the same at any position in that particular.  $W_1^{in}$  is the power input from loudspeakers in the source room,  $W_i^d$  is the power dissipated in the  $i$ -th subsystem, and  $W_{ij}$  is the power flow from the  $i$ -th to the  $j$ -th subsystem.

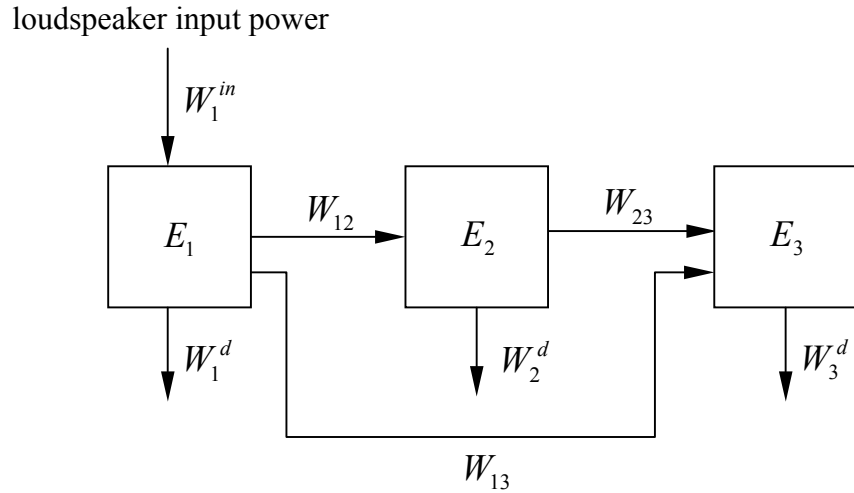


Figure 5.1. Schematic of the power flow in three-coupled systems using SEA.

If only the source room is excited using loudspeakers and there is no other power input to the other subsystems, the power balance equations can be expressed as:

$$\left. \begin{aligned} W_1^{in} &= W_1^d + W_{12} + W_{13}, \\ W_{12} &= W_2^d + W_{23}, \\ W_3^d &= W_{13} + W_{23}. \end{aligned} \right\} \quad (5-2)$$

The power dissipated in a system in a specified frequency band is related to the energy stored in the system,  $E_i$ , through the internal loss factor  $\eta_i$ , namely,

$$W_i^d = E_i \omega \eta_i, \quad (5-3)$$

where  $\omega$  is the center frequency of the frequency band. The power flow between subsystems  $i$  and  $j$  is

$$W_{ij} = \omega \eta_{ij} n_i \left( \frac{E_i}{n_i} - \frac{E_j}{n_j} \right), \quad (5-4)$$

where  $n_i$  and  $n_j$  are the modal densities of subsystems  $i$  and  $j$ , and  $\eta_{ij}$  is the coupling loss factor from subsystem  $i$  to subsystem  $j$ . The equation  $\frac{\eta_{ij}}{\eta_{ji}} = \frac{n_j}{n_i}$  must be satisfied.

Applying Eq.s (5-4) to (5-2) gives the power balance of the partition in a frequency band with the center frequency  $\omega$ :

$$W_{12} = \omega \eta_{21} n_2 \left( \frac{E_1}{n_1} - \frac{E_2}{n_2} \right) = E_2 \omega \eta_2 + E_2 \omega \eta_{23}. \quad (5-5)$$

Note that generally  $E_3 / n_3 \ll E_1 / n_1$ , so the  $E_3 / n_3$  term is neglected in Eq. (5-5). Here the coupling loss factors  $\eta_{23}$  and  $\eta_{32}$  are related to the sound radiation efficiency  $\sigma_{\text{rad}}$ :

$$\eta_{21} = \eta_{32} = \eta_{\text{rad}}^{2\pi} = \frac{\rho c \sigma_{\text{rad}}^{2\pi}}{\rho_s \omega}. \quad (5-6)$$

The subscript  $2\pi$  means that  $\sigma_{\text{rad}}^{2\pi}$  represents the one-sided radiation efficiency. Since the source room sound field is assumed to be reverberant, the energy stored in it is expressed by the pressure  $p_1$ , and volume  $V_1$ :

$$E_1 = \langle p_1^2 \rangle V_1 / \rho c^2. \quad (5-7)$$

The mechanical energy stored in the panel is expressed by its velocity and mass:

$$E_2 = \langle v^2 \rangle \rho_s A_p, \quad (5-8)$$

where  $\rho_s$  and  $A_p$  are the surface density and area of the panel.

Combining the results above, the averaged squared velocity of the panel is obtained

$$\langle v^2 \rangle = \frac{n_2}{n_1} \cdot \frac{\eta_{\text{rad}}^{2\pi}}{2\eta_{\text{rad}}^{2\pi} + \eta_2} \cdot \frac{V_1}{\rho_s A_p} \cdot \frac{\langle p_1^2 \rangle}{\rho c^2}. \quad (5-9)$$

Thus the power radiated by the resonant modes into the receiving room is

$$W_{23} = \rho c A_p \sigma_{\text{rad}}^{2\pi} \langle v^2 \rangle. \quad (5-10)$$

Similarly,  $W_{13} = \omega \eta_{13} E_1$ . The coupling loss factor  $\eta_{13}$  due to non-resonant random incidence mass-law transmission is obtained from [15]

$$10 \log_{10} \eta_{13} = -\text{TL}_{\text{RI}} + 10 \log_{10} \left( \frac{A_p c}{4 \omega V_1} \right), \quad (5-11)$$

$$\text{TL}_{\text{RI}} = 10 \log_{10} a^2 - 10 \log_{10} \left[ \ln(1 + a^2) \right], \quad (5-12)$$

where  $a = \omega \rho_s / 2 \rho c$ , and  $\text{TL}_{\text{RI}}$  is called the random incidence transmission loss.

Substituting (5-12) in (5-11),  $\eta_{13}$  can be derived as

$$\eta_{13} = \frac{A_p \rho^2 c^3}{V_1 \omega^3 \rho_s^2} \ln \left[ 1 + \frac{\omega^2 \rho_s^2}{4 \rho^2 c^2} \right]. \quad (5-13)$$

$$\Rightarrow W_{13} = \frac{\langle p_1^2 \rangle A_p \rho c}{(\omega \rho_s)^2} \ln \left[ 1 + \frac{\omega^2 \rho_s^2}{4 \rho^2 c^2} \right]. \quad (5-14)$$

In the source room, the sound power incident on the dividing partition of area  $A_p$  is:

$$W_{\text{inc}} = \frac{\langle p_1^2 \rangle}{4 \rho c} A_p. \quad (5-15)$$

Below the critical frequency, the sound transmission loss of a finite panel is more controlled by the contribution of those modes that have their resonance frequencies outside the frequency band of the excitation signal than by those with resonance frequencies within that band. So taking into account both the forced and resonant panel motions, the transmission coefficient can be approximated by

$$\frac{1}{\tau} = \frac{W_{\text{inc}}}{W_{23} + W_{13}} = \frac{A_p / 4 \rho c}{\frac{n_2}{n_1} \cdot \frac{\eta_{\text{rad}}^{2\pi}}{2 \eta_{\text{rad}}^{2\pi} + \eta_2} \cdot \frac{V_1}{\rho_s c} \cdot \sigma_{\text{rad}}^{2\pi} + \frac{A_p \rho c}{(\omega \rho_s)^2} \ln \left[ 1 + \frac{\omega^2 \rho_s^2}{4 \rho^2 c^2} \right]}. \quad (5-16)$$

Then, the sound transmission loss TL can be calculated by

$$TL = 10 \log(1/\tau) . \quad (5-17)$$

For a given panel and enclosure,  $A_p$ ,  $\rho_s$ ,  $V_1$ ,  $n_1$ , and  $\rho c$  are constants. So, in order to optimize the sound transmission loss, we narrow the problem down to some properties of the sandwich panel: the modal density  $n_2$ , the internal loss factor  $\eta_2$ , and the radiation efficiency  $\sigma_{\text{rad}}^{2\pi}$ .

### 5.2.1 Modal density

The modal density is defined as the number of vibration modes of a system in a unit frequency interval. It can be derived from the wavenumber space as shown in Fig. 5.2. For a given frequency  $\omega$ , the wavenumber of an isotropic plate,  $k = \sqrt{k_x^2 + k_y^2}$ , forms a quarter of a circle. If all the boundaries are simply-supported, for a plate with side lengths  $a$  and  $b$ , the modal count  $N(\omega)$  and modal density  $n(\omega)$  are

$$N(\omega) = \frac{\frac{\pi}{4} k^2}{\frac{\pi}{a} \cdot \frac{\pi}{b}} = \frac{A_p}{4\pi} k^2 ,$$

$$\Rightarrow n(\omega) = \frac{dN(\omega)}{d\omega} = \frac{A_p}{4\pi} \cdot \frac{dk^2}{d\omega} . \quad (5-18)$$

Most of the researchers simplified the equation of motions of a sandwich panel to fourth-order, although they deal with sandwich beams using sixth-order equations [59,100,105]. However, as shown in Chapter 3, the equation of motion of sandwich panels should be sixth-order. In this chapter the equation derived by Mead is used [41]:

$$D_f \nabla^6 w - g(D_f + Y) \nabla^4 w - \rho_s \omega^2 \nabla^6 w + \rho_s \omega^2 g(1 - \nu^2) w = 0 . \quad (5-19)$$



Here  $w$  is the transverse displacement of the sandwich panel,  $D_f$  is the bending stiffness of one face sheet about its own neutral axis, as defined in Chapter 3,  $\rho_s$  is the surface density of the sandwich panel, and  $\nu$  is the Poisson ratio of the panel. For symmetric sandwich panels, the two parameters are  $Y = d^2 E_f t_f / 2$ , and  $g = 2G / E_f t_f t_c$ . By assuming simple harmonic solution, the wavenumber  $k$  can be obtained by the use of the bi-cubic equation:

$$k^6 + g \left( 1 + 3 \frac{d^2}{t_f^2} \right) k^4 - \frac{\rho_s \omega^2}{D_f} k^2 - \frac{\rho_s \omega^2 g}{D_f} (1 - \nu^2) = 0. \quad (5-20)$$

Then the modal density can be calculated using Eq. (5-18) by solving for  $k^2$  from Eq. (5-20). Note that although Eq. (5-18) is derived from simply-supported panels, the shape and the boundary conditions do not affect the result much. However, as shown in Fig. 5.2 (b), if the panel is not isotropic, the wavenumber  $k$  does not form a quarter of a circle. In this case, the value of  $k$  solved using Eq. (5-20) is angle dependent, because both  $E_f$  and  $G$  change with angle. Then modal count must then be modified as

$$N(\omega) = \frac{A_p}{2\pi^2} \int_0^{\pi/2} k^2(\omega, \phi) d\phi. \quad (5-21)$$

### 5.2.2 Analysis of critical frequency

As discussed before, the critical frequency is the frequency at which the speed of flexural waves in the panel is the same as the speed of sound wave in air. By setting  $k = 2\pi f / C_p$ , and  $C_p = 343$  m/s, and substituting these in Eq. (5-20), the critical frequency of a sandwich panel can be found as

$$f_c = \frac{1}{2\sqrt{2}\pi} \sqrt{B + \sqrt{B^2 + 4C}}, \quad (5-22)$$

where

$$B = \frac{\rho_s (343)^4}{D_f} - g \left( 1 + 3 \frac{d^2}{t_f^2} \right) (343)^2, \quad (5-23)$$

$$C = \frac{(343)^6 \rho_s g}{D_f} (1 - \nu^2). \quad (5-24)$$

Next we will simplify the expressions for  $B$  and  $C$  to study the relationship between the critical frequency and other parameters. If the core is thick enough compared to the face sheet, then we have  $d = t_c + t_f \approx t_c$ . Substituting this and the expression of parameter  $g$  into Eq.s (5-23) and (5-24), then,

$$B = \frac{12 \times (343)^4 \rho_s}{E_f t_f^3} - \frac{2G \cdot (t_f^2 + 3d^2) \cdot (343)^2}{E_f t_f^3 t_c} \quad (5-25)$$

$$\approx \frac{12 \times (343)^4 \rho_s}{E_f t_f^3} - \frac{6 \times (343)^2 G}{E_f t_f^3},$$

$$C = \frac{24 \times (343)^6 \cdot \rho_s \cdot G}{E_f^2 \cdot t_f^4 \cdot t_c} (1 - \nu^2). \quad (5-26)$$

Since the surface density  $\rho_s$  increases with an increase in the core thickness, it can be seen, from Eqs. (5-25) and (5-26), that both  $B$  and  $C$  increase, if other parameters do not change. Consequently, the critical frequency increases with an increase in the core thickness. However, this conclusion is only valid in some range, because it is drawn from Eq. (5-20) which is derived for a thin panel. Intuitively, the critical frequency should decrease with an increase in the thickness.

Other cases are relatively more complicated. For example, a change in the face sheet thickness leads to changes in the surface density and shear modulus of the entire panel. The Young's and shear moduli, however, generally change simultaneously, but not

necessarily in the same direction. So for different sandwich panels, it is not easy to predict the trend of the change in the critical frequency. In most the cases, the critical frequency needs to be evaluated quantitatively based on the material properties and geometry of the sandwich panel under study. However, one can use Eq. (5-22) as a guide to select appropriate materials so that the critical frequency can be removed from the frequency range in which human hearing is most sensitive.

## **5.3 Experimental Results and Discussion**

### **5.3.1 Transmission loss measurement using two-room method**

As described in the previous section, the two-room method was used to determined the sound transmission loss in the Sound and Vibration Laboratory at Auburn University. The two-room suite consists of two reverberation rooms. The panels under investigation were mounted in the window in the walls between the two rooms, as shown in Fig. 5.3. The volumes of the source room and receiving room are  $51.15 \text{ m}^3$  and  $51.51 \text{ m}^3$ , respectively. The area of the panels under test is  $0.36 \text{ m}^2$ . In order to reduce environmental noise, each room has two walls made of wood with fiberglass filled in between them. The two rooms are also separated from each other using fiberglass, and mounted on air bags to reduce the flanking transmission between them. The inner walls of both rooms are made with materials with low absorption coefficients so that the rooms have long reverberation times and the sound fields therein can be assumed to be diffuse. However, since each sound field is not completely diffuse, the sound absorption in each should be taken into account. By assuming that the panel under test is the only path that

the sound travels through, the sound transmission loss measured using the two-room method is given by

$$TL = L_{p1} - L_{p2} + 10 \log \frac{A_p c T_{R2}}{24V_2 \ln 10} = NR + 10 \log \frac{A_p c T_{R2}}{24V_2 \ln 10} , \quad (5-27)$$

where  $L_{p1}$  and  $L_{p2}$  are the sound pressure levels measured in the two rooms, and  $T_{R1}$  and  $V_2$  are the reverberation time and volume of the receiving room [149].

Table 5.1 lists the properties of the panels in study. Two homogenous aluminum panels were pre-tested in order to make sure the measurement procedure was correct because the sound transmission properties of aluminum panels are already known.

First of all, the reverberation times in the receiving room were measured for each panel using B&K PULSE system. Table 5.2 shows the reverberation times measured for one-third octave frequency bands from 80 Hz to 8 kHz.

Then a steady white noise is generated using two loudspeakers and an air jet nozzle in the source room. The air jet nozzle was used to increase the noise level in the high frequency region. The sound pressure levels in two rooms were measured using two B&K microphones, type 4188, whose optimized frequency response range is from 8 Hz to 12.5 kHz. For each panel listed in Table 5.1, the measurements of the sound pressure levels in both the source and receiving rooms ( $L_{p1}$  and  $L_{p2}$ ) were repeated eight times by putting the two microphones at eight randomly selected positions. The spatial averages were calculated to obtain the noise reduction (NR). Note that the background noise in the receiving room was also measured and subtracted from  $L_{p2}$ . The sound transmission loss was then calculated using Eq. (5-20).

### 5.3.2 Transmission loss measurement using sound intensity method

The sound intensity measurement technique using the cross-spectrum of two microphones was presented by Fahy, and Waser and Crocker [150,151]. This technique was then used in the sound transmission loss measurement by Crocker and other researchers [151,152]. The experimental setup is shown in Fig. 5.3 (b). In this technique, the receiving room is changed from a reverberation room to an anechoic room. The anechoic room can be constructed using wedges or fiberglass rolls with very high sound absorption capability so that the sound field can be assumed to be essentially a free field. An intensity probe is used to measure the sound intensity in the anechoic room,  $L_{I2}$ . Then the sound transmission loss is the difference in the sound intensity levels incident on the panel and transmitted by it into anechoic room:

$$TL = L_{I1} - L_{I2} = \frac{\langle p_i^2 \rangle}{4\rho c} - L_{I2}, \quad (5.28)$$

where  $\langle p_i^2 \rangle$  is the spatial average of the incident sound pressure square.

Compared to the two-room method, the sound intensity method is less time consuming, and it is not necessary to measure the reverberation times in the receiving room. However, a disadvantage of the sound intensity method is the frequency limitations. The low frequency limit is due to the phase mismatch between the two microphones. The high frequency limit is caused by the finite distance approximation error [151]. The intensity probe used in the Sound and Vibration Laboratory is a B&K type 3548, which has two ½ inch microphones, and its optimal frequency range is from 125 Hz to 5 kHz when a 12 mm spacer is used.

Figure 5.4 compares the sound transmission loss of Panel A using the two-room method and the sound intensity method. The two results are in good agreement. The maximum difference is about 2 dB. Because the sound field in the anechoic room is not an ideal free field, the measured sound intensity level,  $L_{I2}$ , also contains some reflected sound. This makes the measured transmitted sound intensity level somewhat less than the true value, especially for frequency bands higher than the critical frequency.

So considering the frequency range limit of the sound intensity method, the conventional two-room method was used to measure the sound transmission loss.

### 5.3.3 Radiation efficiency

As discussed before, the radiation efficiency of a panel is an important parameter needed in the prediction of its sound transmission loss using SEA. The radiation efficiency can be obtained experimentally by measuring the radiation resistance  $R_{\text{rad}}$ . The radiation resistance is defined as the ratio of the sound power radiated to the space averaged mean-square value of the panel's normal velocity:  $R_{\text{rad}} = W_{\text{rad}} / \langle v^2 \rangle_{\text{s,t}}$ . With the two-room method measurement setup, the panel was excited by a shaker using white noise. One microphone was located in each room to measure the sound radiated from the panel under the external excitation. An accelerometer was used to measure the panel response. For each panel, the sound pressure levels in the two rooms and the acceleration responses were measured at eight randomly selected positions, and averages were made. The two-sided radiation resistance of the panel is given by

$$R_{\text{rad}}^{4\pi} = \frac{13.8\omega^2}{S_a \rho c^2} \left[ \frac{S_1 V_1}{T_{R1}} + \frac{S_3 V_3}{T_{R3}} \right], \quad (5-29)$$

where  $S_1$ ,  $S_3$ ,  $S_a$  are the power spectral density functions of the signals obtained from the two microphones and the accelerometer,  $V_1$  and  $V_3$  are the volumes of the source room and the receiving room, respectively, and  $T_{R1}$  and  $T_{R3}$  are the reverberation times of the two rooms [15]. The radiation efficiency is then expressed as

$$\sigma_{\text{rad}}^{2\pi} = \frac{R_{\text{rad}}^{4\pi}}{2A_p \rho c}. \quad (5-30)$$

### 5.3.4 Simulation using AutoSEA

AutoSEA is an interactive vibro-acoustics simulation tool based on the SEA method. In order to calculate the sound transmission loss and the radiation efficiency of a panel, two virtual rooms and a panel must be created in AutoSEA, as shown in Fig. 5.5. The two virtual rooms were assumed each to have a diffuse sound field, and to have the identical volumes as do the two real rooms in the Sound and Vibration Laboratory. A random sound source was used to simulate the white noise generation in the source room. The panel under investigation has clamped boundary conditions. For an isotropic aluminum panel, the material and geometric properties, such as mass density, Young's modulus, Poisson's ratio, thickness, area and perimeter must be defined. To create a sandwich panel in AutoSEA, the material properties of the face sheets and the core are required separately. The face sheets of a sandwich panel must only be isotropic while the core can be orthotropic. The material properties assumed for the face sheets and the core are listed in Appendix B.

The internal loss factor in AutoSEA can be frequency dependent. The loss factors for all of the one-third octave bands, which are called the damping spectra, were

predefined and input to the software based on the measured damping loss factors. Note that the sound transmission loss depends on the internal damping, while the radiation efficiency does not.

### **5.3.5 Experimental and simulation results**

In order to verify the experimental method, measurements on two aluminum panels were carried out first, because the radiation and sound transmission properties of isotropic materials have been well established. Figures 5.6 and 5.7 compare the measured radiation efficiency and sound transmission loss of Panel E, with the results simulated using AutoSEA software in which the internal loss factor was set to 1%. It can be seen that the measured results agree quite well with the results simulated using AutoSEA. Both the measured and the simulated results show the critical frequency at 4000 Hz which is the same as the one calculated using Eq. (5-1). Below the critical frequency, the radiation efficiency increases with frequency. At the critical frequency, it reaches a maximum value. Above the critical frequency, the radiation efficiency decreases to a plateau level. The discrepancies between the measured and the simulated results in the low frequency region are mainly because the area of the panel is not large enough. Since the modal density of a homogenous aluminum panel is constant, there are not enough modes at low frequencies to make a good statistical frequency average of the sound transmission loss.

Figures 5.8 and 5.9 show the measured and simulated radiation efficiency of Panels A and B. The predictions using AutoSEA are quite close to the measured results. However, it should be noted that for frequencies higher than the critical frequency, the



radiation efficiency does not decrease to a plateau value. Sandwich and isotropic panels thus appear to have a different behavior.

Figures 5.10 and 5.11 illustrate the measured and simulated sound transmission loss of Panels A and B. For Panel A, two cases with different values of damping were evaluated with AutoSEA. The first damping spectrum used the measured loss factors as shown in Chapter 3. In this case, the internal loss factor increases with frequency. In the other case, the loss factor was assumed to be constant, 2%, in all the frequency bands. By comparing the two simulated cases with the measured result, it can be seen that the simulated result with measured frequency-dependent damping is closer to the measured result. This means that for the sound transmission loss prediction using SEA, the frequency-dependent damping is more suitable.

The first natural frequency of Panel A mounted in the window is about 170 Hz. At frequencies below the first natural frequency, the behavior of the panel is stiffness controlled. This explains the dip in the sound transmission loss curve in the 160 Hz band in Fig.11. Since the face sheets in Panel B are twice thick as those in Panel A, the first natural frequency is higher. It can be seen in Fig.12 that the dip in the sound transmission loss is in the 200 Hz band.

The measured sound transmission loss results of all the panels used in the study are shown in Fig. 5.13. In order to quantify and compare the overall sound transmission loss properties of these panels, their sound transmission classes (STC) were calculated using the procedure defined in ASTM standard E413-87. These sound transmission class values are listed in the legend of Fig. 5.13. It is seen that the sound transmission loss values of all the four sandwich panels are smaller than those of the two aluminum panels. This

implies that the surface mass density still dominates the overall transmission loss behaviors of these panels. The foam-filled honeycomb sandwich design does not demonstrate any advantage of sound transmission over heavier metal counterpart, although the sandwich structures have higher damping. That means such a foam-filled honeycomb sandwich design must be modified if it is to obtain higher sound transmission loss.

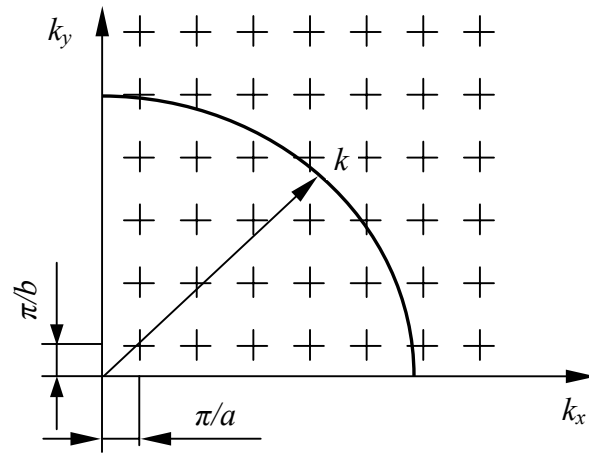
For further comparison, another aluminum panel with a similar surface mass density to the studied sandwich panels was simulated in AutoSEA. The thickness of this aluminum panel was set to 1 mm. Its surface density is  $2.7 \text{ kg/m}^3$  which is very close to the surface density values of Panels A, B and C. Figure 5.14 compares the calculated TL of such an aluminum panel with the measured TL of Panel A. Since the simulated aluminum panel is thinner than Panels E and F, its critical frequency increases to 12.5 kHz. The STC values also show that the overall TL of the aluminum panel is higher than the sandwich panels studied.

<b>Panel</b>	<b>Core thickness (mm)</b>	<b>Face sheet thickness (mm)</b>	<b>Density (kg/m<sup>3</sup>)</b>	<b>Surface density (kg/m<sup>2</sup>)</b>
A	6.35	0.33	327.75	2.41
B	6.35	0.66	336.97	2.57
C	12.7	0.66	190.96	2.50
D	25.4	0.66	130.25	3.28
E	3.175 mm thick homogeneous aluminum			8.57
F	6.35 mm thick homogeneous aluminum			17.15

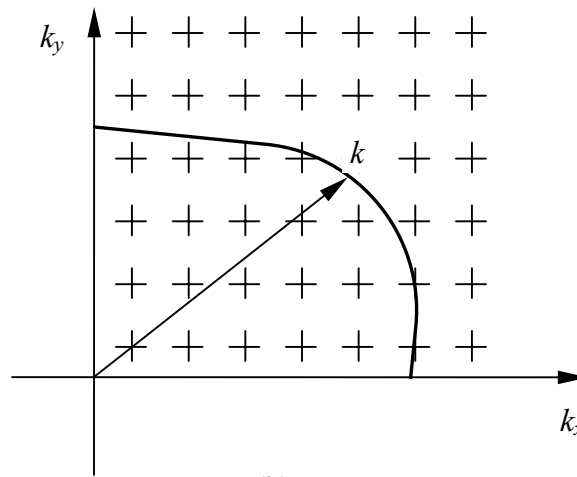
Table 5.1. Geometry parameters of panels under study.

<b>Center frequency (Hz)</b>	<b>Panel A</b>	<b>Panel B</b>	<b>Panel C</b>	<b>Panel D</b>	<b>Panel E</b>	<b>Panel F</b>
80	0.380	0.375	0.421	0.377	0.370	0.370
100	0.632	0.544	0.557	0.506	0.574	0.675
125	0.493	0.395	0.352	0.360	0.405	0.374
160	0.636	0.659	0.699	0.634	0.634	0.610
200	0.578	0.740	0.736	0.698	0.740	0.643
250	0.903	0.818	0.856	0.860	0.865	0.887
315	1.048	1.086	1.034	1.043	1.079	1.110
400	1.240	1.162	1.155	1.111	1.196	1.190
500	1.264	1.254	1.309	1.345	1.293	1.329
630	1.316	1.407	1.324	1.344	1.362	1.349
800	1.411	1.449	1.473	1.430	1.420	1.376
1000	1.326	1.364	1.368	1.338	1.309	1.335
1250	1.238	1.248	1.224	1.247	1.203	1.235
1600	1.132	1.157	1.121	1.146	1.144	1.136
2000	1.028	1.036	1.016	1.016	1.033	0.983
2500	0.947	0.916	0.947	0.937	0.912	0.960
3150	0.846	0.809	0.865	0.830	0.846	0.861
4000	0.778	0.759	0.780	0.747	0.764	0.782
5000	0.698	0.688	0.690	0.713	0.702	0.709
6300	0.633	0.639	0.629	0.652	0.629	0.632
8000	0.556	0.545	0.555	0.538	0.526	0.541

Table 5.2. Reverberation times of the receiving room with different panels.



(a)



(b)

Figure 5.2. Modal distribution of (a) isotropic and (b) anisotropic plates.

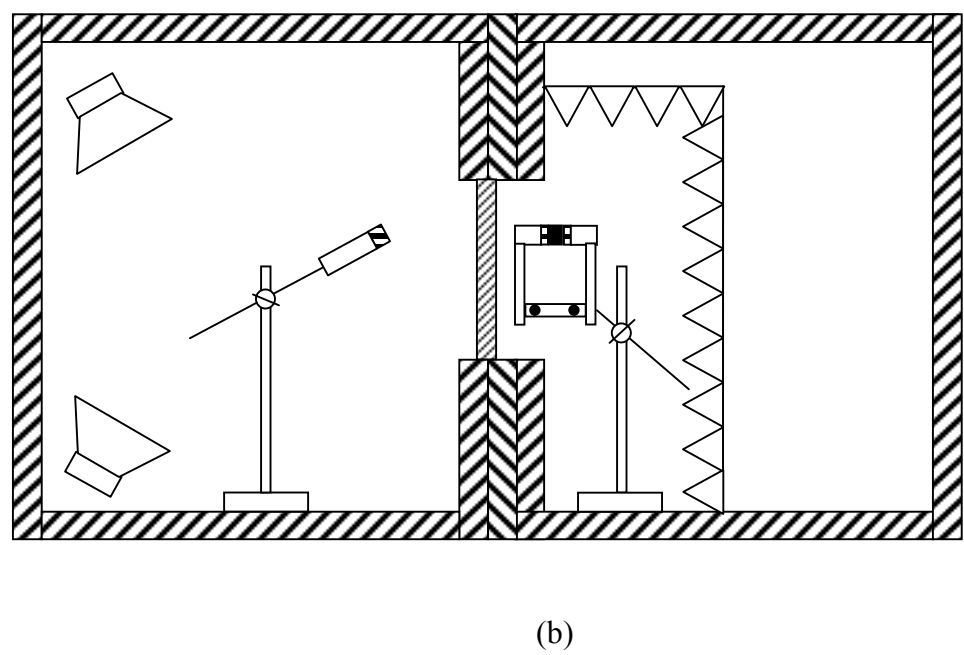
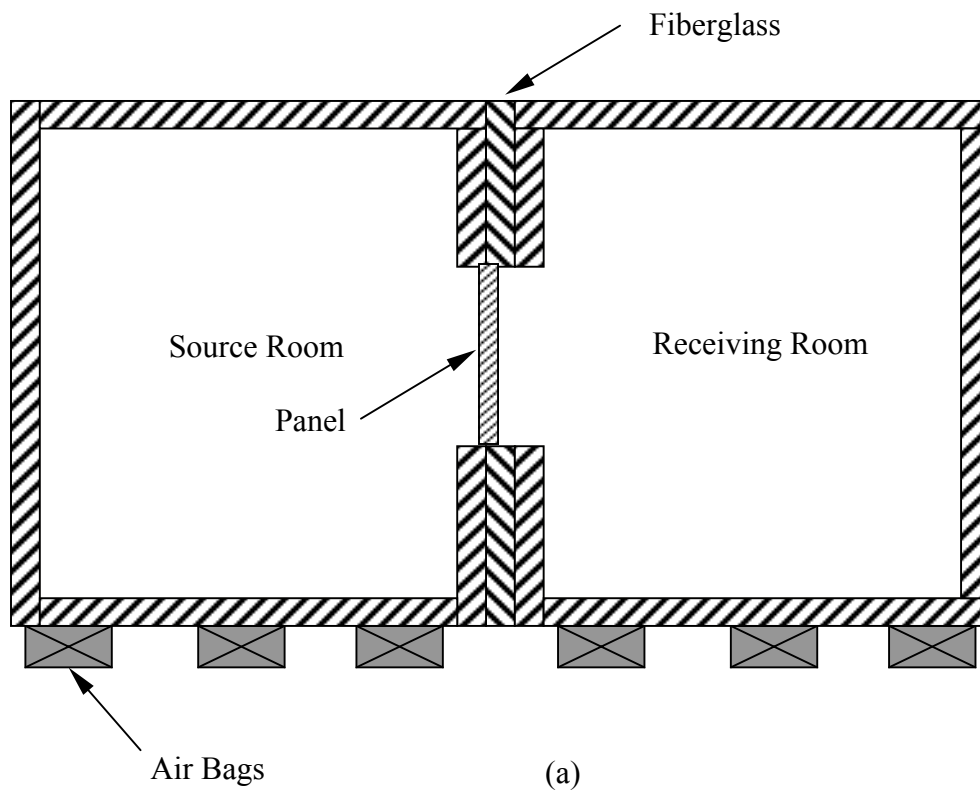


Figure 5.3. Side views of (a) the two reverberation rooms, and (b) experimental setup for transmission loss measurements using sound intensity method.

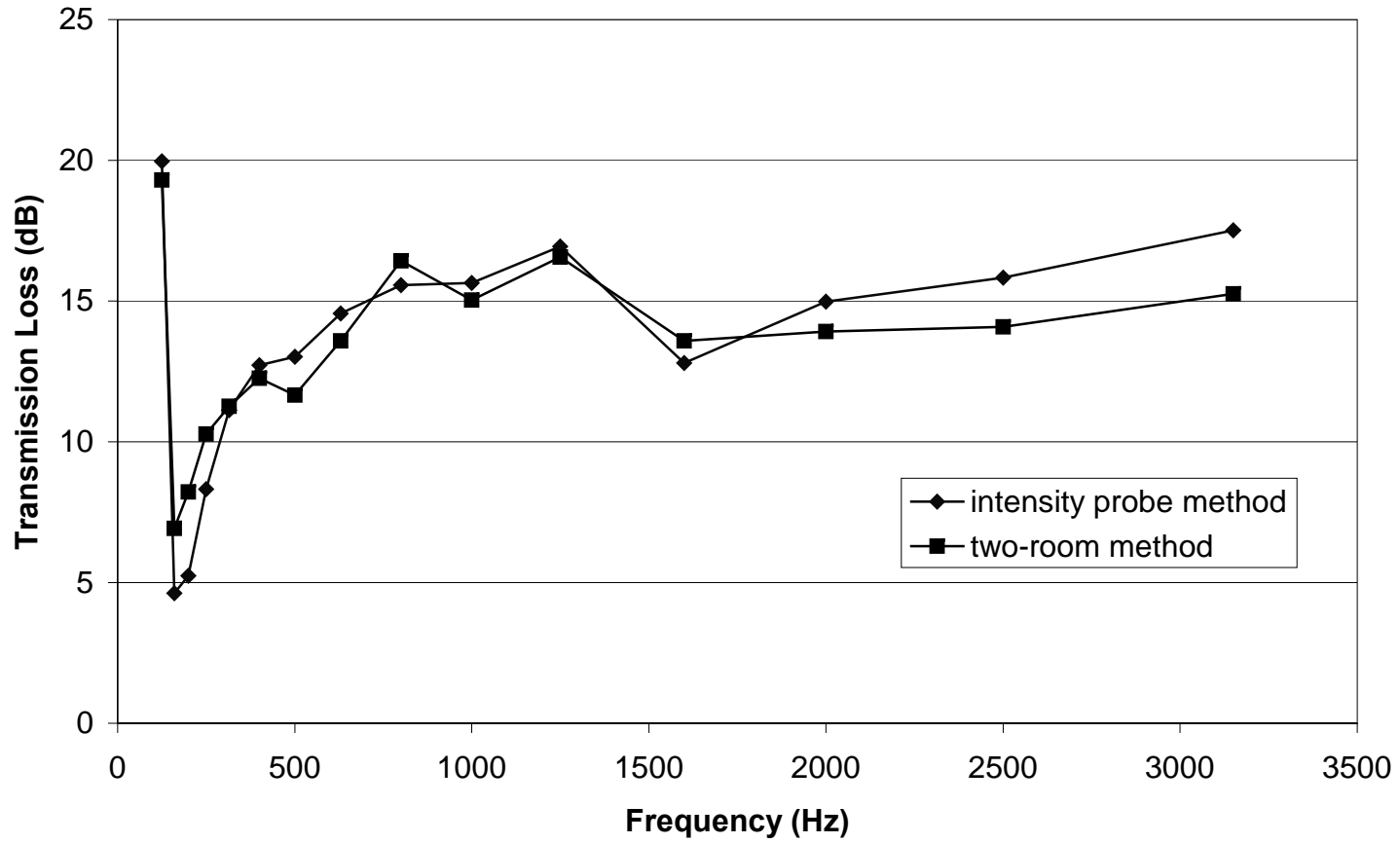


Figure 5.4. Comparison of sound transmission loss measurements of composite Panel A using two-room method and sound intensity method.

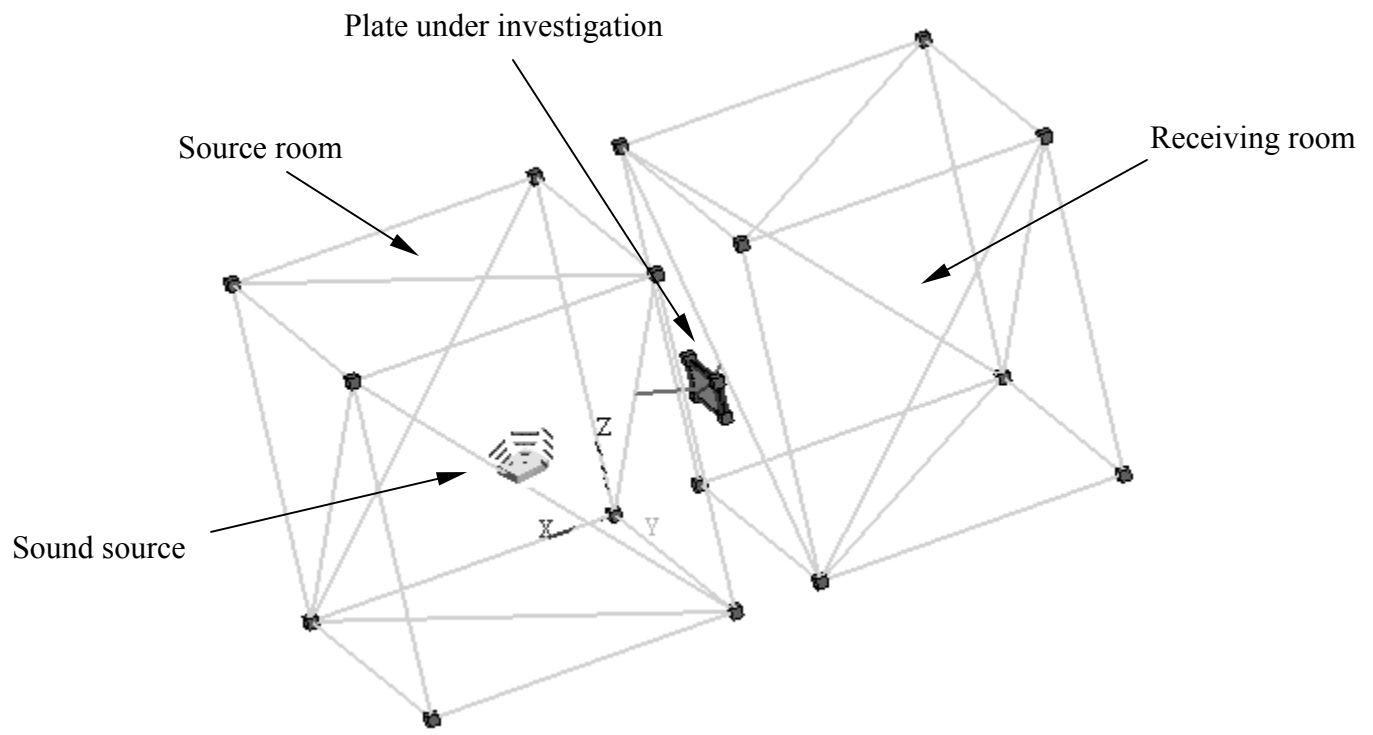


Figure 5.5. Sound transmission loss model using AutoSEA software.



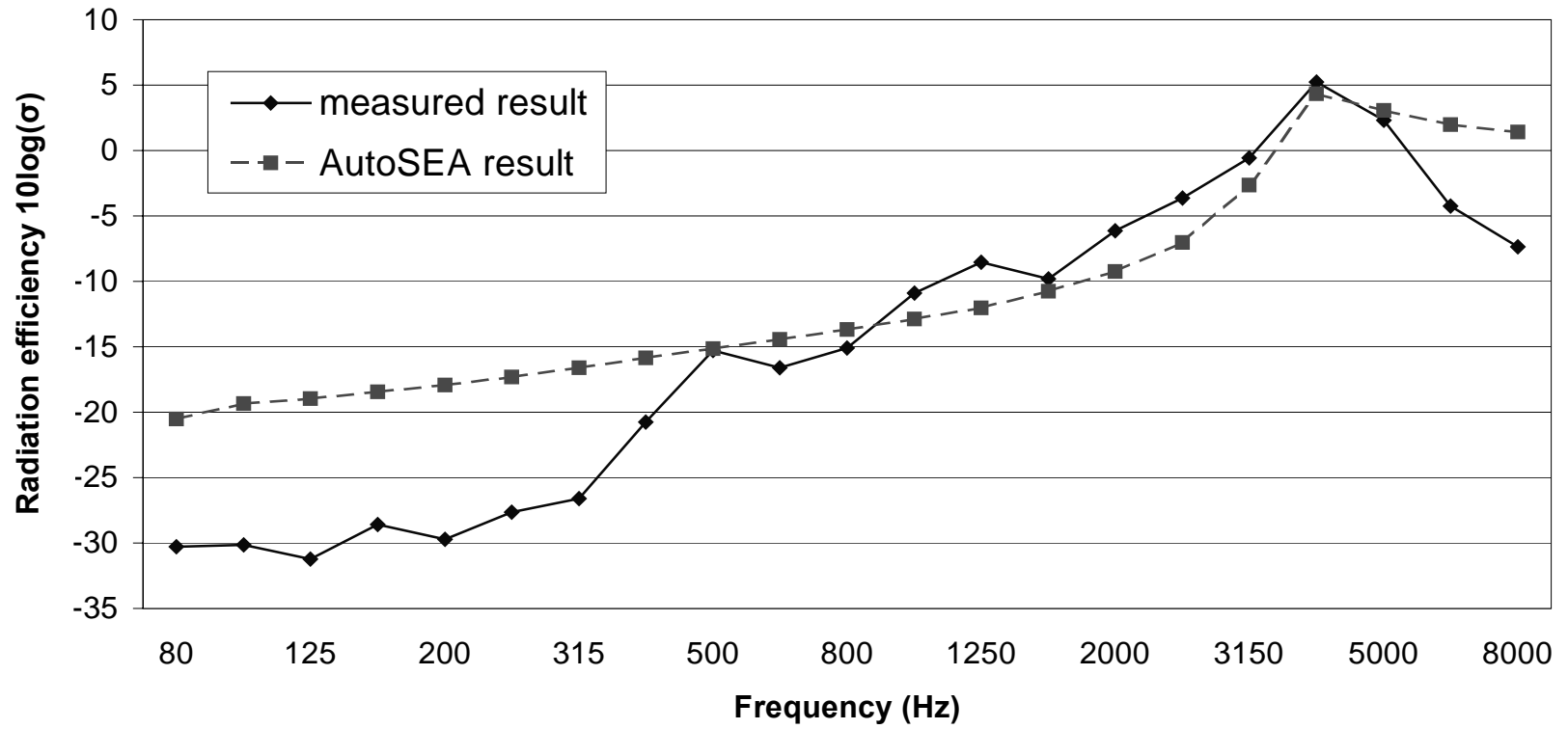


Figure 5.6. The measured and simulated radiation efficiency of Panel E.

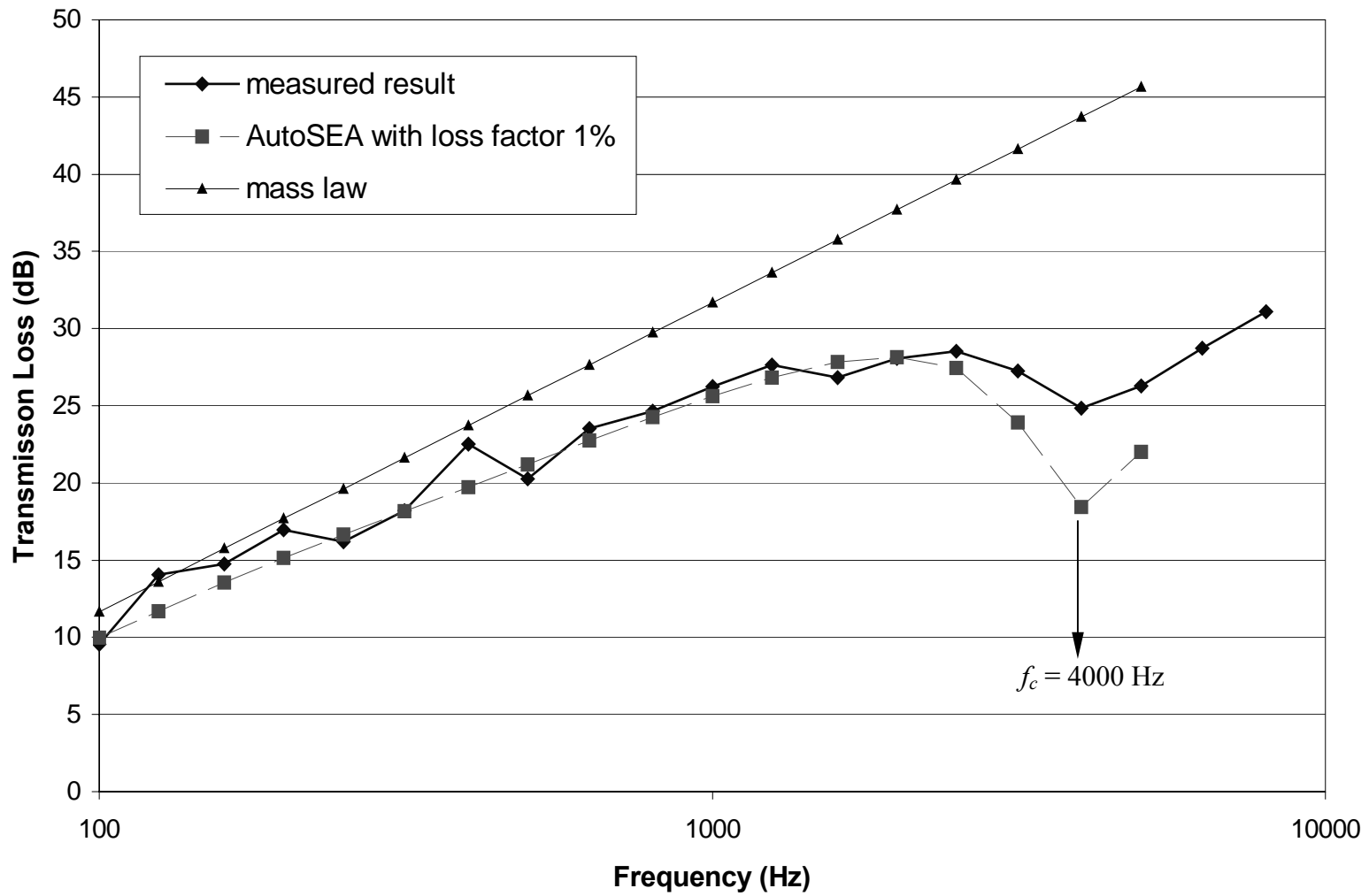


Figure 5.7. Sound transmission loss of Panel E.

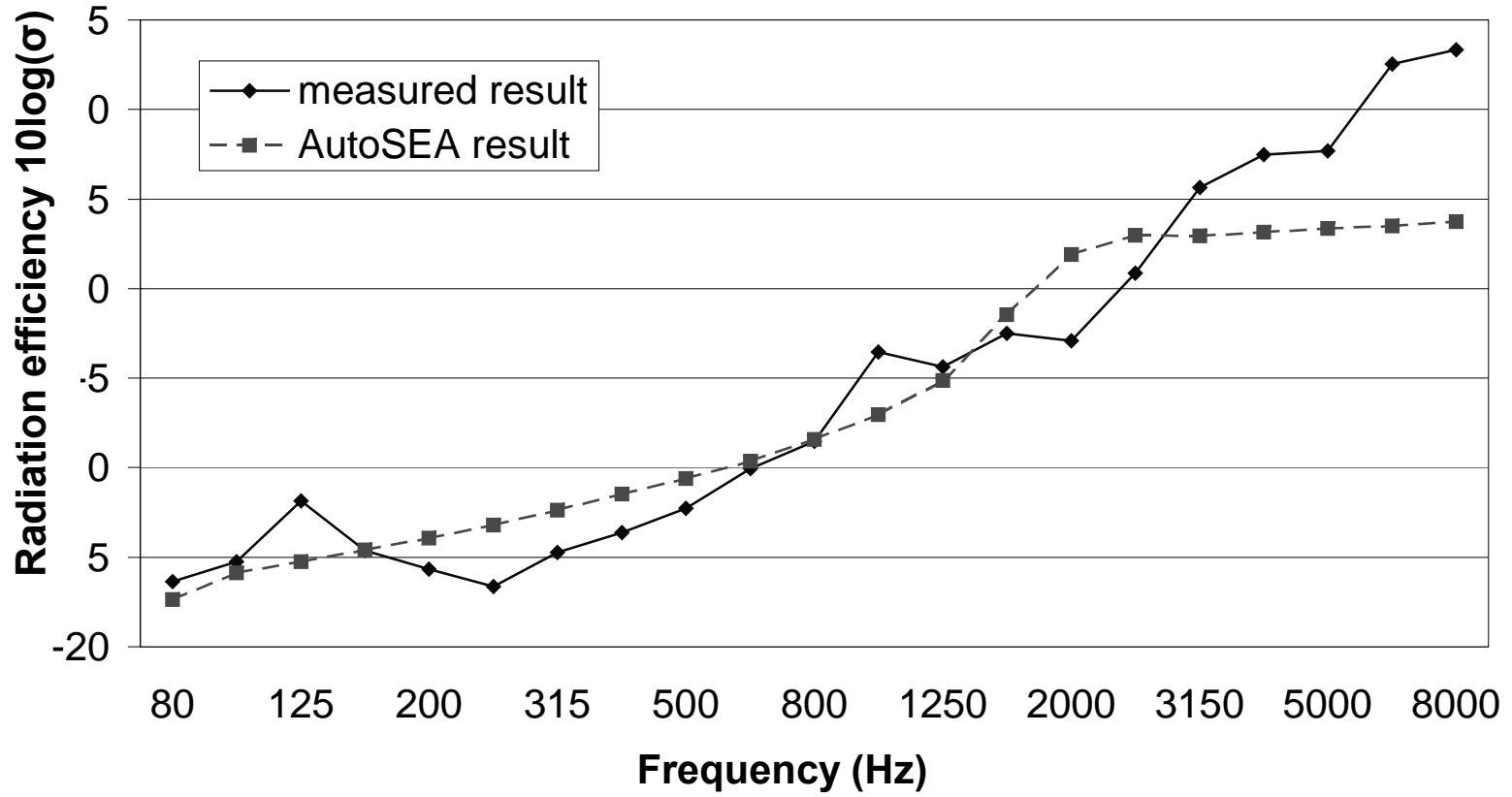


Figure 5.8. Measured and simulated radiation efficiency of Panel A.

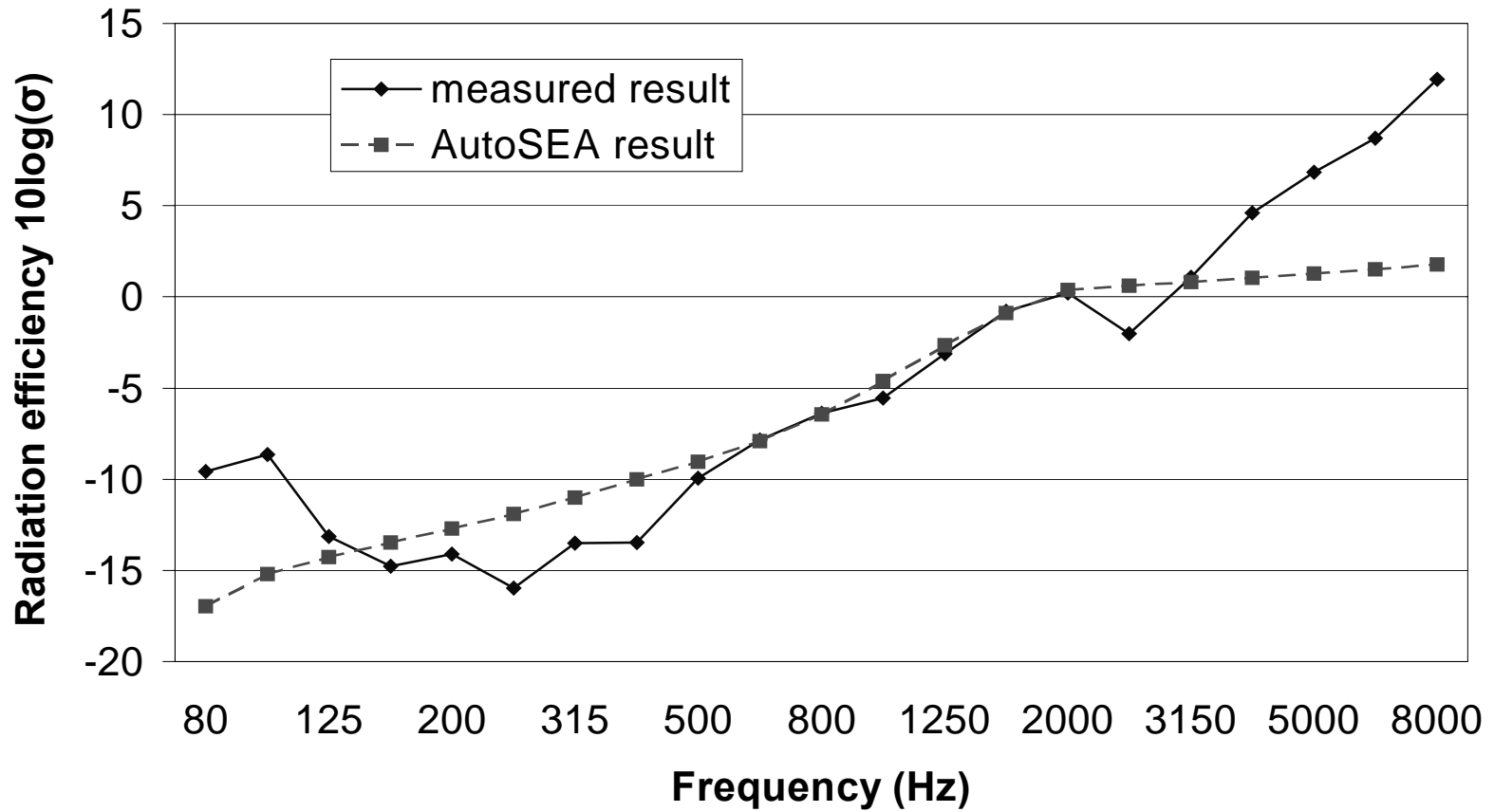


Figure 5.9. Measured and simulated radiation efficiency of Panel B.

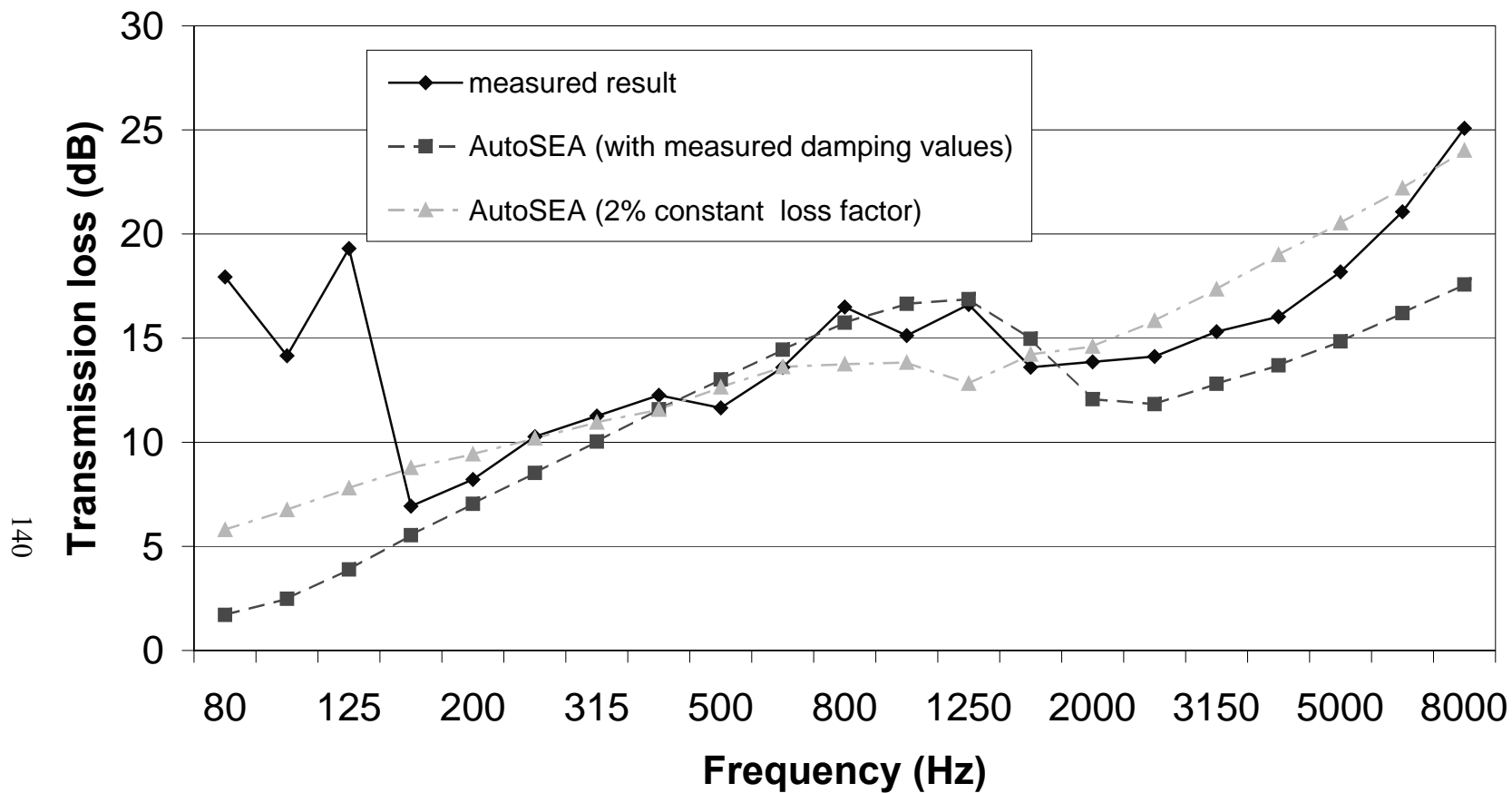


Figure 5.10. The measured and simulated sound transmission loss of Panel A.

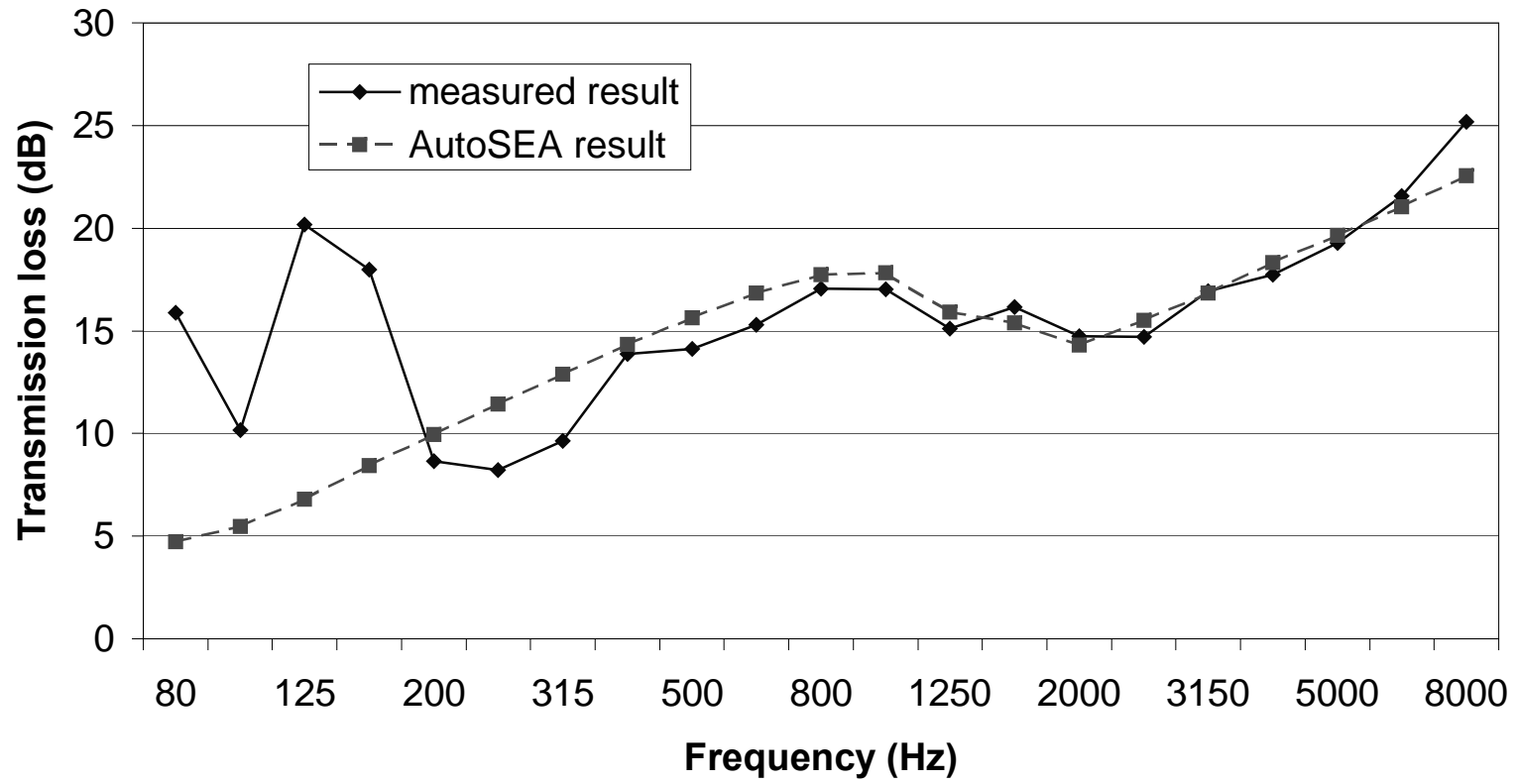


Figure 5.11. Measured and simulated transmission loss of Panel B.

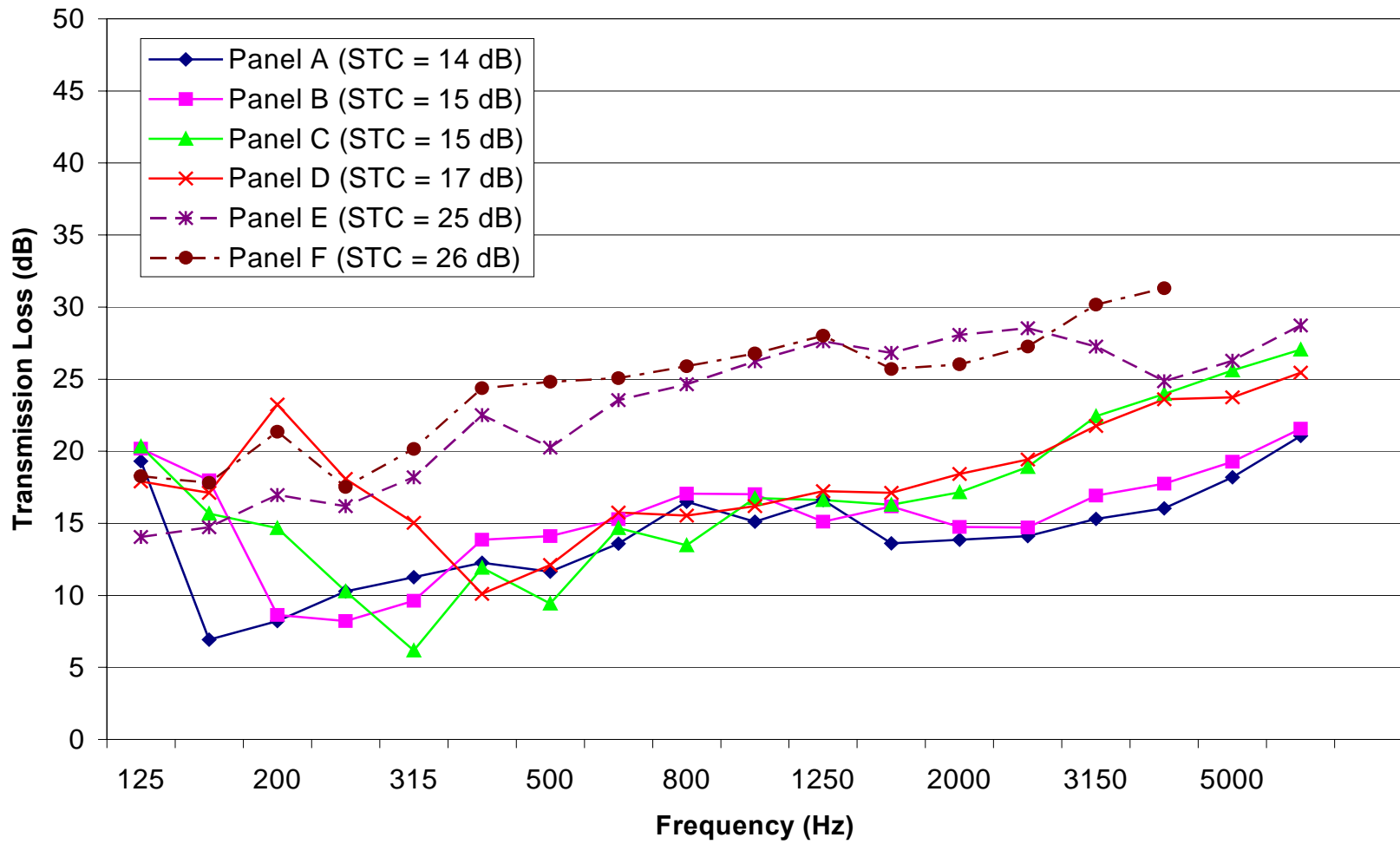


Figure 5.12. Comparison of sound transmission loss and sound transmission class of panels studied.

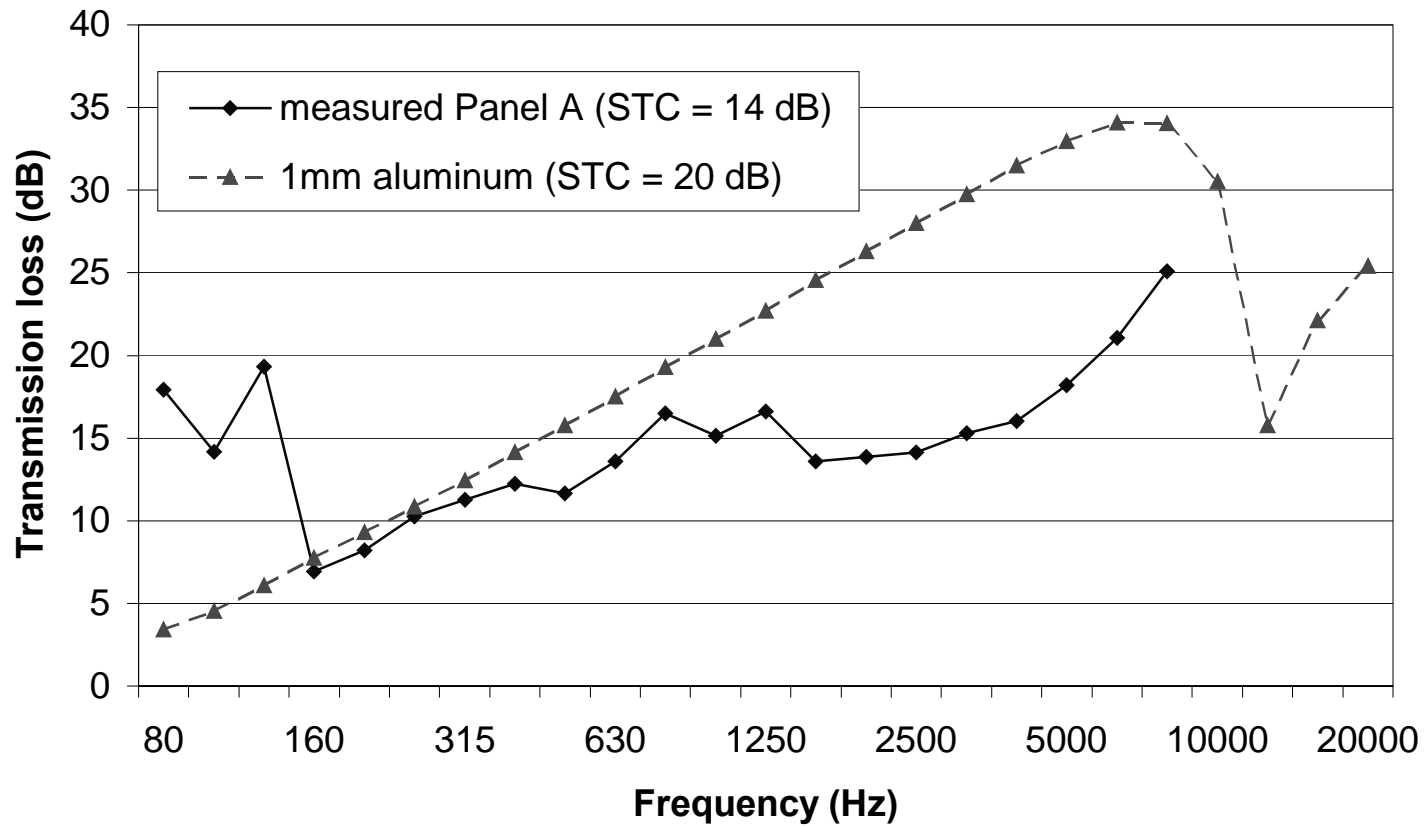


Figure 5.13. Comparison of sound transmission loss and sound transmission class of Panel A with an aluminum panel having the same surface density.



## CHAPTER 6 ANALYSIS OF FOAM-FILLED HONEYCOMB

### CORES USING FEM

As we study the dynamics of foam-filled honeycomb sandwich structures, an important issue associated with the material properties is the honeycomb cell size effect. Onck et al. analyzed the size effect of pure hexagonal honeycombs on the Young's and shear moduli in terms of the ratio  $\alpha$ , of the honeycomb width,  $b$ , to the cell size,  $D$ , as shown in Fig. 6.1 [153,154]. They reported that as the integer value of  $\alpha$  increases, or the honeycomb cell size decreases relative to the specimen size, the Young's modulus increases to a plateau level which is called the bulk Young's modulus of the honeycomb. This is due to the increased constraint of the cell walls at the free surface and the decreasing area fraction of the open-cell walls. However, for non-integer values of  $\alpha$ , the Young's modulus drops as  $\alpha$  increases from one integer to the next. As shown in Fig. 6.1, the longitudinal cell walls of a honeycomb carry most of the uniaxial load. As  $\alpha$  varies from one integer to the next, the number of longitudinal cell walls in the width direction does not change, but the cross-sectional area increases. This results in the Young's modulus drop when  $\alpha$  varies from one integer to the next. Figure 6.2 shows the change in the Young's modulus with respect to  $\alpha$  [153].

As discussed in the previous chapters, the sandwich structures with foam-filled honeycomb cores show some advantages compared with pure honeycomb cores. By filling foam in the honeycomb cells, not only the longitudinal cell walls but also the foam

can carry the uniaxial load. So the foam is expected to reduce the discontinuity of the Young's modulus observed with pure honeycomb cores.

Onck et al. only derived the theoretical expressions for the honeycomb beam of one cell wide,  $\alpha = 1$ , which is the simplest case [153]. Compared to the use of the finite element method, the theoretical derivation for honeycomb beams with higher values of  $\alpha$  will be much more difficult. So Onck et al. used the finite element software ABAQUS to study those more complicated cases.

Similar finite element models were developed to analyze the material properties of foam-filled honeycombs using ANSYS, and are presented in this chapter. Sections 6.1 and 6.2 describe the modeling procedure and present results of the effect of cell size on the Young's modulus and shear modulus. Composite materials may have a negative value of Poisson's ratio. The influence of Poisson's ratio is studied in Section 6.3. The relationship between the cell size and other properties is discussed as well.

### 6.1 Size Effect on the Young's Modulus

Gibson and Ashby stated that the Young's moduli of a honeycomb in the L- and W-directions are the same if the cell size is sufficiently small [155]. That means that there are a large number of honeycomb cells in both the L- and W-directions. In this case the bulk Young's modulus  $E_{\text{bulk}}$  in both the L- and W-directions of a honeycomb is

$$E_{\text{bulk}} = \frac{4E_w}{\sqrt{3}} \left( \frac{t}{l} \right)^3, \quad (6-1)$$

where  $E_w$  is the Young's modulus of the honeycomb cell wall, and  $t$  and  $l$  are the thickness and length of the cell wall as shown in Fig. 6.3. Figure 6.3 illustrates a section of a honeycomb and the beam model of the cell wall.  $D$  is the cell size which is the

distance from two parallel cell walls,  $D = \sqrt{3}l$ , and  $d$  is the thickness of the whole honeycomb.

If there is only one cell in the W-direction, or  $\alpha = 1$ , then the compression modulus in the L-direction becomes

$$E^* = \frac{2E_w}{\sqrt{3}} \left( \frac{t}{l} \right)^3, \quad (6-2)$$

which is one half of the result calculated using Eq. (6-1).

A finite element model was developed using ANSYS to study the Young's modulus of the foam-filled honeycombs. The basic idea is to build a beam as shown in Fig 6.1 and calculate the deflection  $\delta$  under a uniaxial pressure  $P$ . Then the Young's modulus can be obtained. All the foam-filled honeycombs have the same width,  $b = 30$  mm, and thickness,  $d = 0.25$  inch = 6.35 mm. As the cell size is varied, the number of cells in the width direction varies accordingly. The bottom end of the beam is assumed clamped. Since the foam is much softer than the honeycomb wall, a single force applied on the top of the beam may cause stress concentration. Instead, the uniaxial load is simulated by imposing a uniform pressure of 10,000 Pa on the top.

Since the model is assumed to be a plane stress problem, the whole beam is simplified using a 2-D model. The honeycomb cell walls are modeled using beam elements (BEAM3), as shown in Fig. 6.3 (b). The cross-sectional area, area moment of inertia and cell wall thickness are input as "Real Constants" to the database. The foam in honeycomb cells is modeled using triangular elements (PLANE2) with the same thickness as the whole foam-filled honeycomb beam. Note that the cell wall thickness,  $t$ , and the foam-filled honeycomb beam thickness,  $d$ , are different.

The honeycomb walls are assumed to be isotropic with the Young's modulus  $E_w = 109.5$  GPa , Poisson's ratio  $\nu_w = 0.35$  , and density  $533$  kg/m<sup>3</sup>. These values are provided by honeycomb manufacturer, Hexcel Corporation. According to these values, the bulk Young's modulus of a pure honeycomb structure is  $E_{\text{bulk}} = 120$  MPa . Polyurethane foam is assumed to be orthotropic in the x-y plane, but isotropic in the thickness direction. Polyurethane foams are categorized into several quality grades. The material properties used in Chapter 6 are those of Grade 120 Polyurethane foam tested in [155]. They are  $E_{\text{foam}} = 22$  MPa , and  $G_{\text{foam}} = 13.3$  MPa . Poisson's ratio is set to be 0.4.

Before running the foam-filled honeycomb finite element models, a pre-test was conducted for a pure honeycomb beam with  $\alpha = 1$ . The calculated compression modulus is 61 MPa, which is the same as the result calculated using Eq. (6-2). This result verifies that the finite element model is feasible.

The calculated Young's moduli of foam-filled honeycomb beams with different cell sizes are listed in Table 6.1. Note that for different cell sizes, the cell thickness-to-length ratio is set to be constant,  $t/l = 0.078$ , which is the same ratio used in [153]. The cell wall constants and volume ratios are also listed in Table 6.1. From reference [155], for hexagonal honeycombs, the ratio of the volume of honeycomb walls to the volume of the entire structure is

$$\frac{V_{\text{honeycomb}}}{V_{\text{total}}} = \frac{2}{\sqrt{3}} \frac{t}{l}. \quad (6-3)$$

When  $t/l = 0.078$ ,  $V_{\text{honeycomb}}/V_{\text{total}} = 9\%$ .

From Table 6.1 some conclusions can be drawn: (1) The most significant effect of the honeycomb cell size is that the Young's modulus increases as the cell size decreases

( $\alpha$  increases). This is because the honeycomb cells become denser as structural elements so that the constraint increases at the boundary. This trend is the same as that predicted in reference [153]. However, unlike the non-integer  $\alpha$  cases, because of foam filled in honeycombs, there are no non-load-carrying honeycomb cell walls when  $\alpha$  is non-integer. So as  $\alpha$  varies from one integer to the next, the Young's modulus still increases instead.

(2) The Young's modulus of foam-filled honeycombs is greater than those of the corresponding pure honeycombs and pure foam, and even greater than the simple summation of the Young's moduli of the pure honeycomb and foam. (3) As the cell size is decreased, the volume percentage of honeycomb also decreases to the theoretical value of 9% calculated using Eq. (6-3). Considering that polyurethane foam is less costly than honeycombs, these conclusions indicate that even though the volume of the honeycomb cells decreases, the cell size decrement will lead to cheaper and stiffer structures.

## 6.2 Size Effect on the Shear Modulus

Gibson and Ashby give the bulk shear modulus of pure honeycombs with a sufficiently large number of cells in the width direction as follows [155]

$$G_{\text{bulk}} = \frac{E_w}{\sqrt{3}} \left( \frac{t}{l} \right)^3. \quad (6-4)$$

For the honeycomb materials investigated in this chapter,  $G_{\text{bulk}} = 30 \text{ MPa}$ . After foam is filled in the honeycomb cells, the constraints at the boundary become larger compared with the pure honeycomb structures. So the bulk shear modulus of a foam-filled honeycomb structure is higher than the value calculated using Eq. (6-4). However, the relationship between the honeycomb cell size and the shear modulus is not obvious.

Smaller cell size leads to dense honeycomb frame, which seems to increase the constraints at the boundaries. On the other hand, since the thickness of the honeycomb cell wall also decreases when the cell size becomes smaller, it is hard to predict analytically how the constraints at the boundary actually change with the cell size. So a finite element model was developed in ANSYS to study the effect of cell size on the shear modulus of the foam-filled honeycomb structures.

In order to simulate pure shear deformation, the translation in the y-direction of both the upper and lower edges is restricted, as shown in Fig. 6.4 (a), so that these two edges can only slide in the x-direction. The shear forces are simulated using a series of forces of the same magnitude applied along the two edges with uniform distribution. The shear deformation angle should be measured on the centerline. For all samples with different cell size simulated in ANSYS, the total shear force is the same, 8 N. This means although the force distribution along the boundary becomes denser when the cell size is increased, the magnitude of each distributed force element is decreased, so that the summation of the shear force is always equal to 8 N.

Note that in order to obtain accurate results, one dimension, for example the x-direction in Fig. 6.4 (a) of the specimen, must be longer than the other dimension. The aspect ratio should be around 4. This value is obtained from some trial-and-error calculations for aluminum samples modeled using triangular elements and isotropic material properties with the Young's modulus (70 GPa) and Poisson's ratio (0.3). The theoretical shear modulus value is then 26.9 GPa. Table 6.2 lists the calculated shear moduli for different aspect ratios using the finite element model, and relative error compared with the theoretical value of 26.9 GPa.

The same beam and triangle elements used in the previous section were used to model the honeycomb cell walls and foam in ANSYS to study the cell effect on the shear modulus. Figure 6.4 (b) illustrates the deformed element mesh under pure shear forces. Table 6.3 lists the calculated shear moduli of foam-filled honeycombs with different cell sizes. It can be concluded that after foam is filled in the honeycomb cells, the shear modulus of the structure becomes larger than that of a pure honeycomb calculated using Eq. (6-4). As the cell size is decreased, the shear modulus also decreases, which is opposite to the change in the Young's modulus. This means as the cell size is decreased, although the honeycomb frame becomes denser, the cell walls become thinner, which decrease the constraints at the boundary, and therefore decreases the shear modulus of the whole foam-filled honeycomb structure.

Figure 6.5 presents a plot of the results listed in Tables 6.1 and 6.3 in terms of  $\alpha$ . It can be seen that as the cell size is decreased, both the Young's modulus and the shear modulus converge to plateau values which are the bulk Young's modulus and shear modulus.

### **6.3 Influence of Poisson's Ratio**

Poisson's ratio values of conventional materials are generally positive with a theoretical upper limit of 0.5 [157]. However, the development of composite materials has made negative Poisson's ratio values possible. Although hexagonal honeycombs always have positive Poisson's ratios, honeycombs of different shapes and foams can possess negative Poisson's ratios. Figure 6.6 shows three foam microstructures which have negative values of Poisson's ratio from [155]. Figure 6.6 (a) shows an inverted

shape, which can be produced from conventional foams in a variety of ways. Figure 6.6 (b) shows solid cylinders or spheres attached to each other by thin elastic strips or wires. When the structure is stretched in the direction of the arrows, the ligaments unwrap from the cylinders or spheres, causing them to rotate. Therefore the structure expands in other directions. The structure shown in Fig 6.6(c) is an example of a family of open tensile networks of nodes, linked by simple tensile springs, and constrained by hinged inextensible rods or threads. When the material is stretched axially, such constraints force a lateral expansion.

For simplification, the foam modeled in this section is assumed to be isotropic.

Since  $G = \frac{E}{2(1+\nu)}$ , a negative Poisson's ratio will increase the shear modulus if the

Young's modulus does not change. In addition, under longitudinal compression, the foam elements with negative Poisson's ratio do not expand, but also become compressed, in the transverse direction. This phenomenon also increases the compression modulus in the longitudinal direction.

Figures 6.7 and 6.8 show the influence of Poisson's ratio on the Young's modulus and the shear modulus of foam-filled honeycombs. Both the Young's modulus and the shear modulus decrease as the Poisson's ratio increases from -0.8 to 0.4. From the discussion in the previous two sections, we know that the size effects are not significant, when the cell size is small enough relative to the sample size, because both the Young's modulus and the shear modulus converge to the bulk values. However, Figs. 6.7 and 6.8 imply that the material properties can be dramatically modified by changing the Poisson's ratio of the foam. For example, the Young's modulus of the foam-filled honeycomb with



cell size of 4 mm increases from 149.65 MPa to 346.85 MPa (2.3 times stiffer) with a change of Poisson's ratio from 0.4 to -0.8.

#### **6.4 More Considerations of Cell Size Effects**

So far we have seen that the material properties of foam-filled honeycombs can be changed considerably by varying the honeycomb cell size and the Poisson's ratio of the polyurethane foam. These effects are quite useful in the design stage. One can obtain the optimal design according to meet the application goal. However, it should be stated that these effects may be contrary to those needed for different functions of sandwich structures. For example, we always expect high stiffness since the sandwich elements work as structural parts in most engineering applications. On the other hand, as discussed in Chapter 5, sandwich structures are expected to be soft in shear so that the shear wave speed is less than the speed of sound in air. Merely decreasing the honeycomb cell size satisfies both the requirements. Smaller cell sizes also lead to lighter structures.

However, foam with negative Poisson's ratio will increase both the Young's modulus and the shear modulus. An increased Young's modulus will also increase the critical frequency. If the critical frequency is in the high frequency range, one may be able to increase the critical frequency out of the frequency band of interest by increasing the Young's modulus. Unfortunately, as shown in Fig. 5.6, the critical frequency of a sandwich plate is usually in low frequency range. So an increase of stiffness will shift the critical frequency towards the frequency band of interest.

Therefore, a trade-off between the overall stiffness and the sound transmission properties should be considered in the design stage.

<b>Cell size (mm)</b>	$\alpha$	<b>Cell wall length (mm)</b>	<b>Cell wall thickness (mm)</b>	<b>Cross-sectional area (m<sup>2</sup>)</b>	<b>Moment of inertia (m<sup>4</sup>)</b>	<b>Young's modulus (MPa)</b>	<b>Volume ratio <math>V_{\text{honeycomb}}/V_{\text{total}}</math> (%)</b>
30	1	17.32	1.35	8.57e-6	1.30e-12	93.20	10.99
20	1.5	11.55	0.90	5.72e-6	3.86e-13	113.09	10.10
15	2	8.66	0.68	4.32e-6	1.66e-13	124.69	9.91
12	2.5	6.93	0.54	3.43e-6	8.33e-14	130.56	9.65
10	3	5.77	0.45	2.86e-6	4.82e-14	136.48	9.55
7.5	4	4.33	0.34	2.15e-6	2.04e-14	140.58	9.42
6	5	3.46	0.27	1.72e-6	1.04e-14	144.78	9.33
5	6	2.89	0.23	1.43e-6	6.03e-15	146.15	9.29
4	7.5	2.31	0.18	1.14e-7	3.09e-15	149.03	9.23

Table 6.1. Cell size effect on the Young's modulus of foam-filled honeycomb beams.

<b>Aspect ratio</b>	<b>Calculated shear modulus (GPa)</b>	<b>Relative error (%)</b>
1	17.9	-33.50
2	23.76	-11.75
3	25.3	-5.95
4	26.6	-1.11
5	25.4	-5.58
6	25.5	-5.20

Table 6.2. Influence of aspect ratio on the shear modulus calculation using FEM.

<b>Cell size (mm)</b>	<b>Length (m)</b>	<b>Aspect ratio</b>	<b>Shear deformation (m)</b>	<b>Shear modulus (MPa)</b>
30	0.13856	4.62	0.29113e-5	93.7
15	0.12124	4.83	0.92062e-5	52.9
10	0.11547	3.85	1.54958e-5	47.2
7.5	0.11258	3.75	1.07763e-5	45.3
6	0.110828	3.69	1.38337e-5	44.2
5	0.12701	4.23	1.67838e-5	43.8
3	0.117776	3.93	1.43748e-5	42.6

Table 6.3. Cell size effect on the shear modulus of foam-filled honeycomb beams.

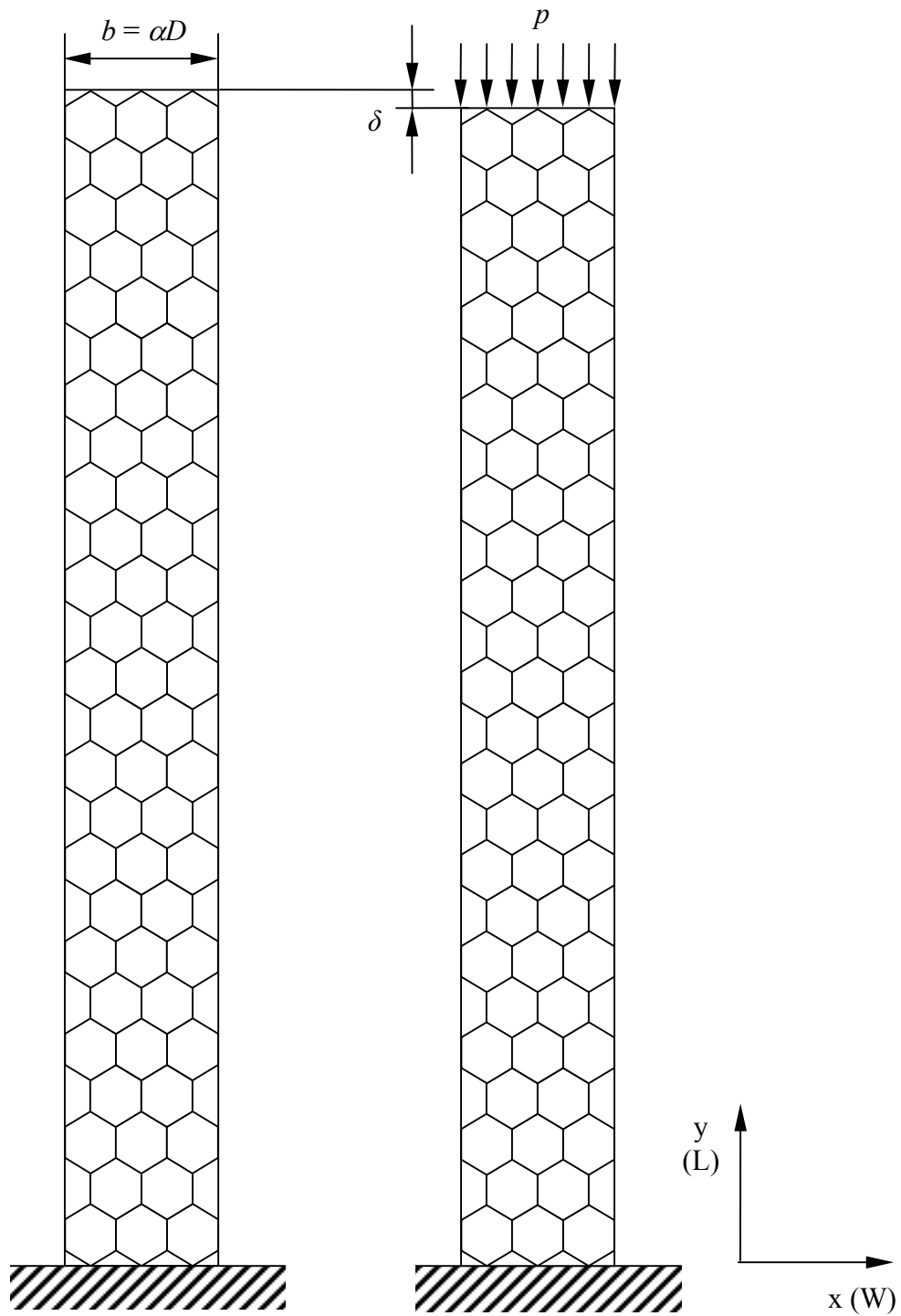


Figure 6.1. (a) A section of the honeycomb structure. (b) Beam element used to model the honeycomb cell wall.

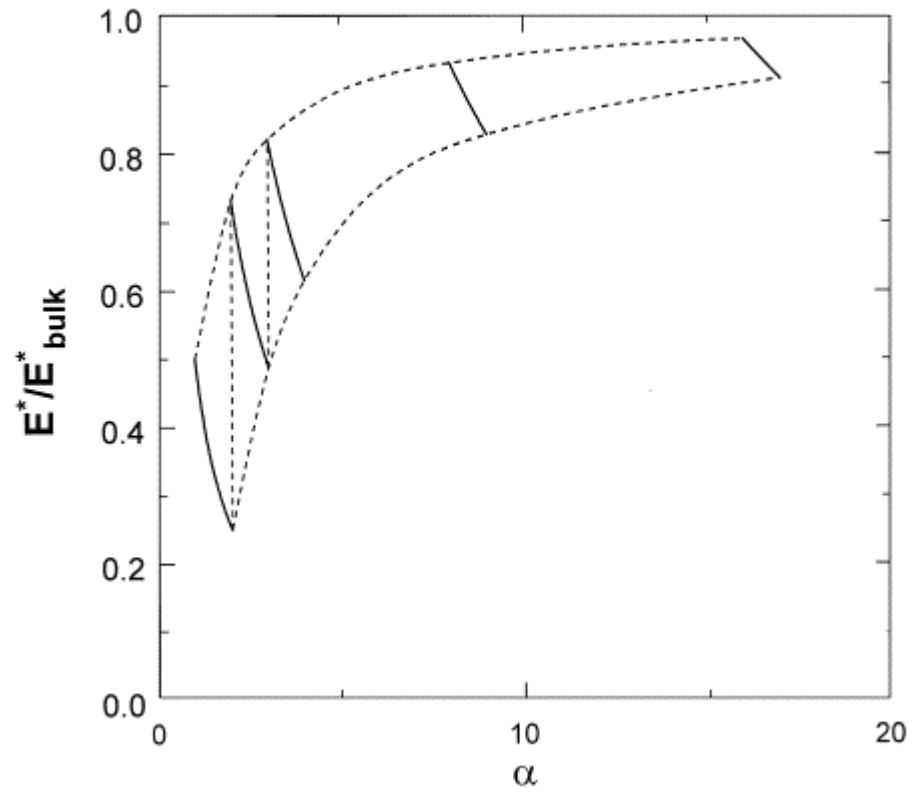


Figure 6.2. Cell size effect on the Young's modulus of pure honeycomb structures.

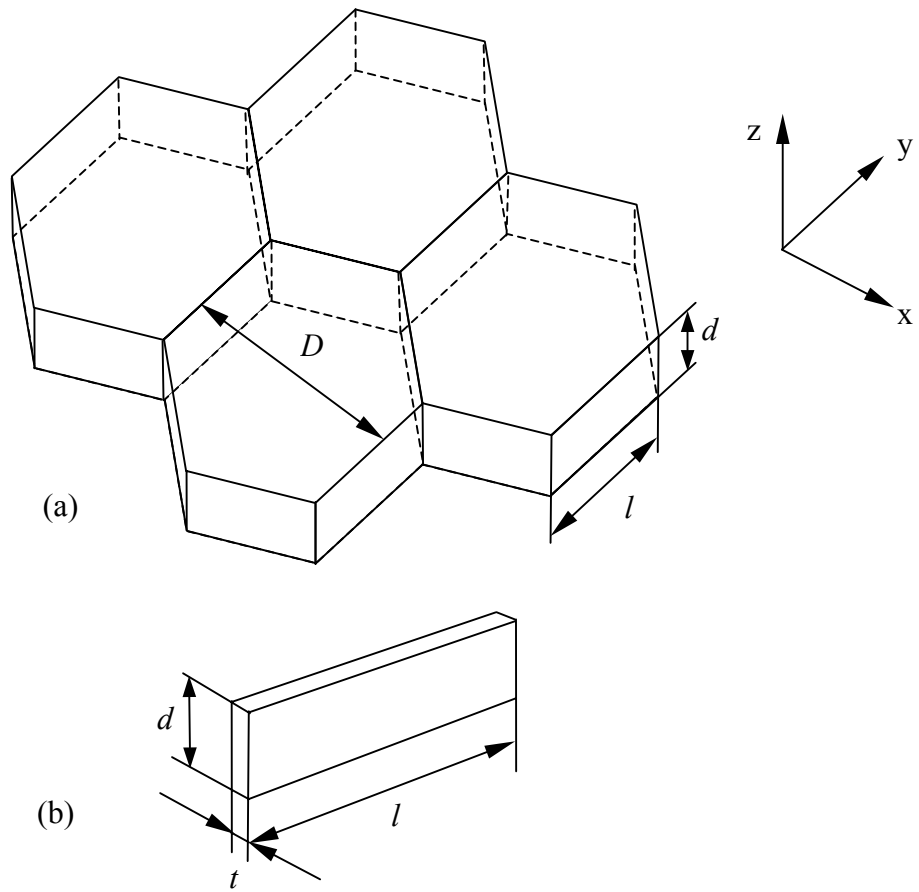


Figure 6.3. (a) A section of the honeycomb structure.  
(b) Beam element used to model the honeycomb cell wall.

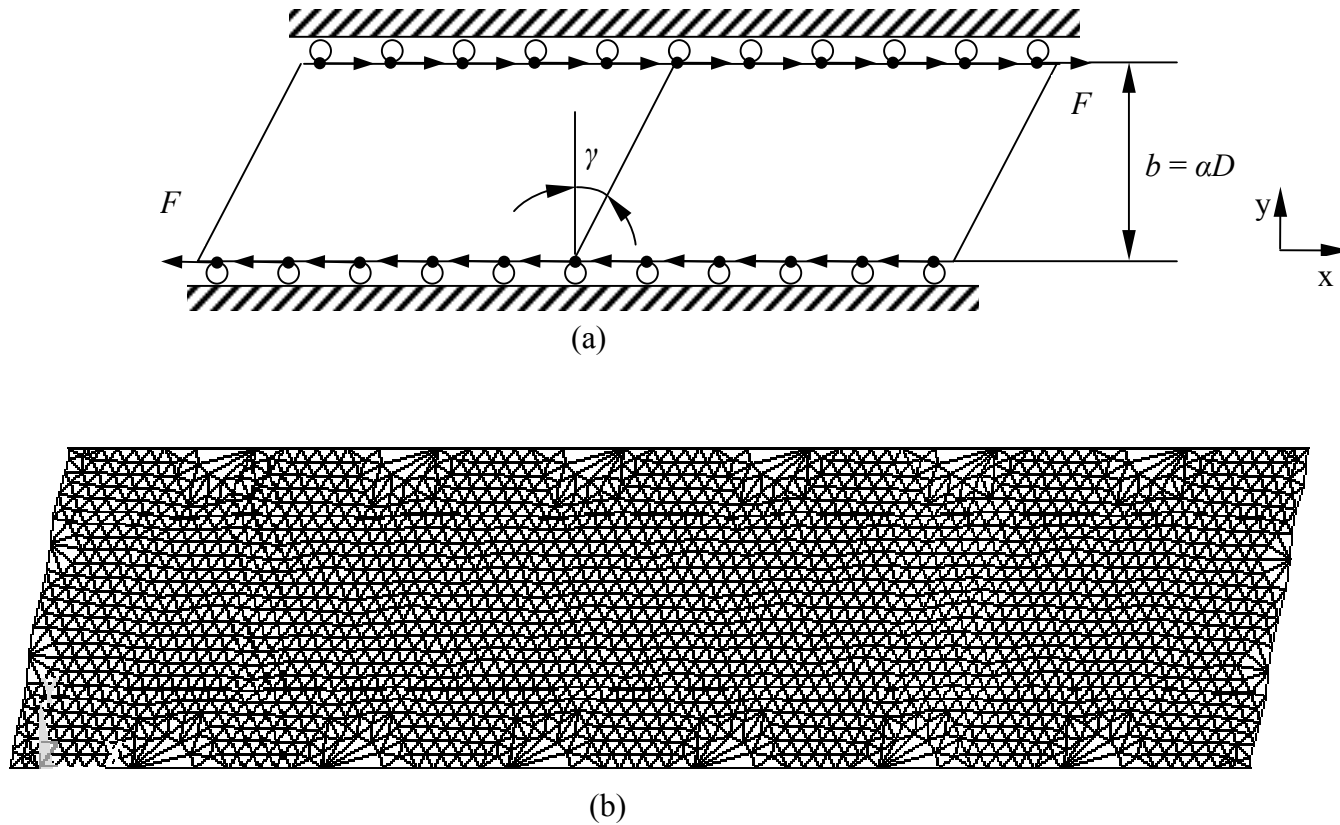


Figure 6.4. (a) Schematic of the shear modulus calculation.

(b) Foam-filled honeycomb finite element mesh and pure shear deformation.



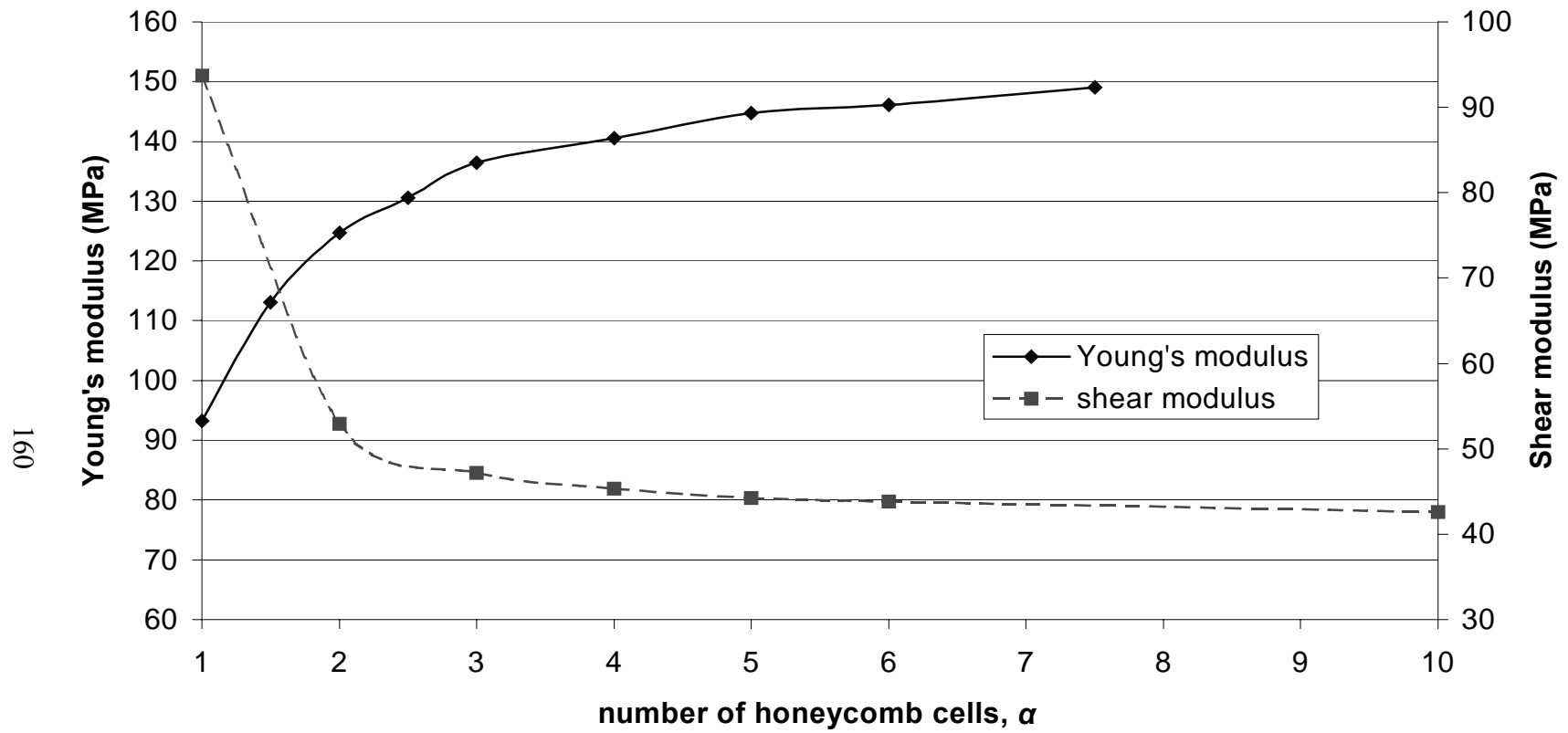


Figure 6.5. Honeycomb cell size effect on Young's modulus and shear modulus of foam-filled honeycomb structures.

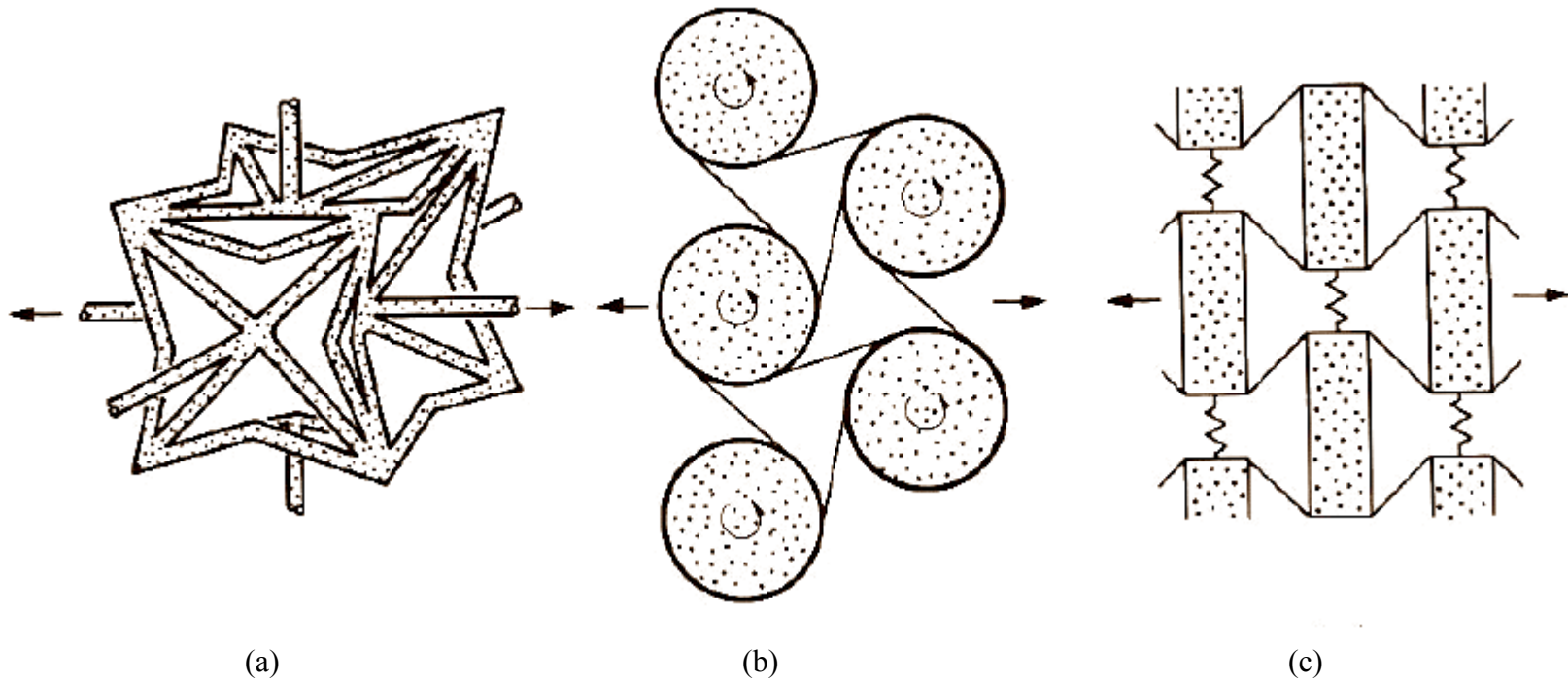


Figure 6.6. Microstructures giving negative Poisson's ratios [155]. (a) Inverted "reentrant" cell shape.

(b) Solid cylinders or spheres attached to each other by elastic strips.

(c) Nodes, connected by tensile springs, and constrained by hinged inextensible rods.

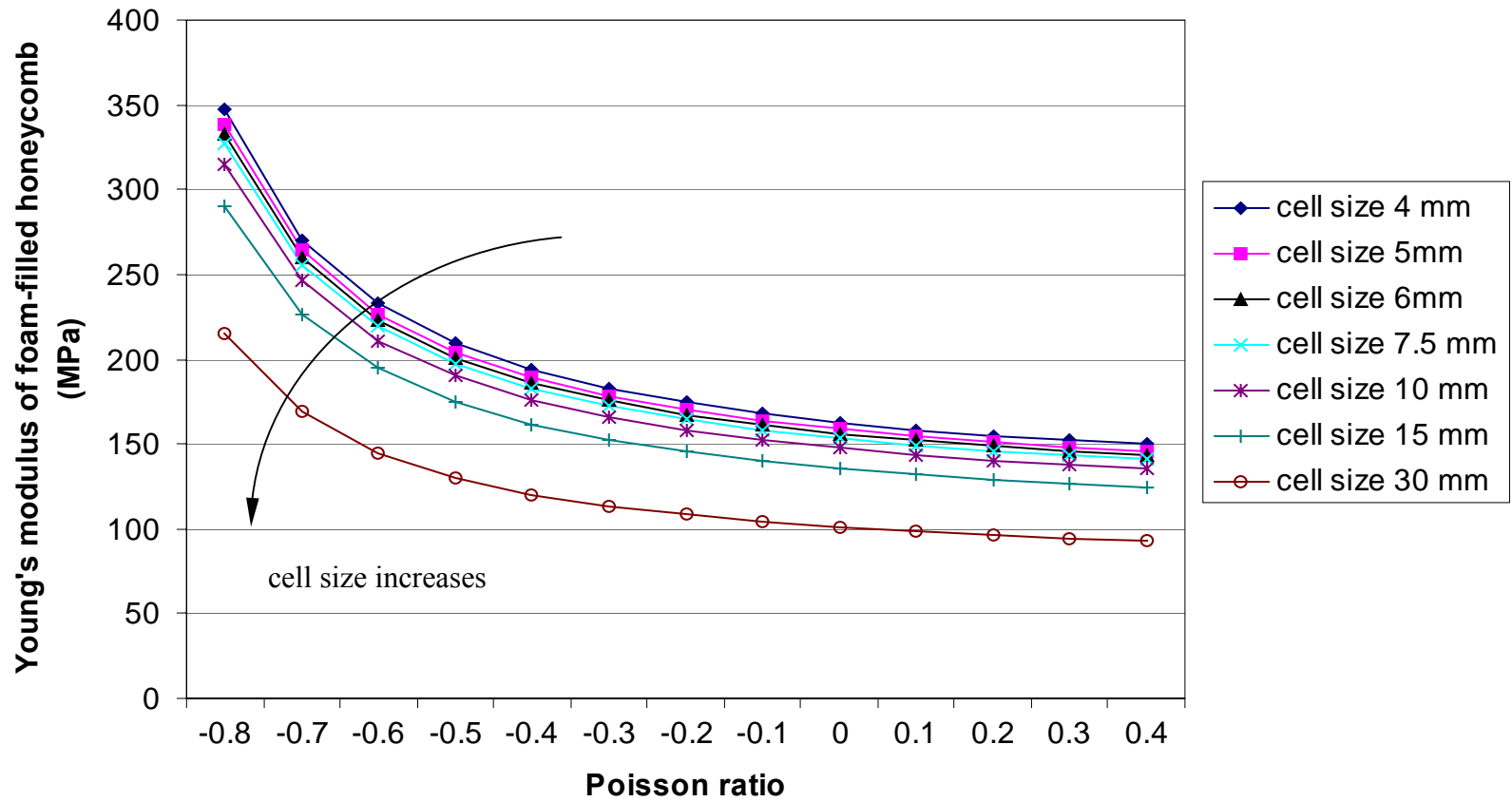


Figure 6.7. Influence of Poisson's ratio on the Young's modulus of foam-filled honeycomb structures.

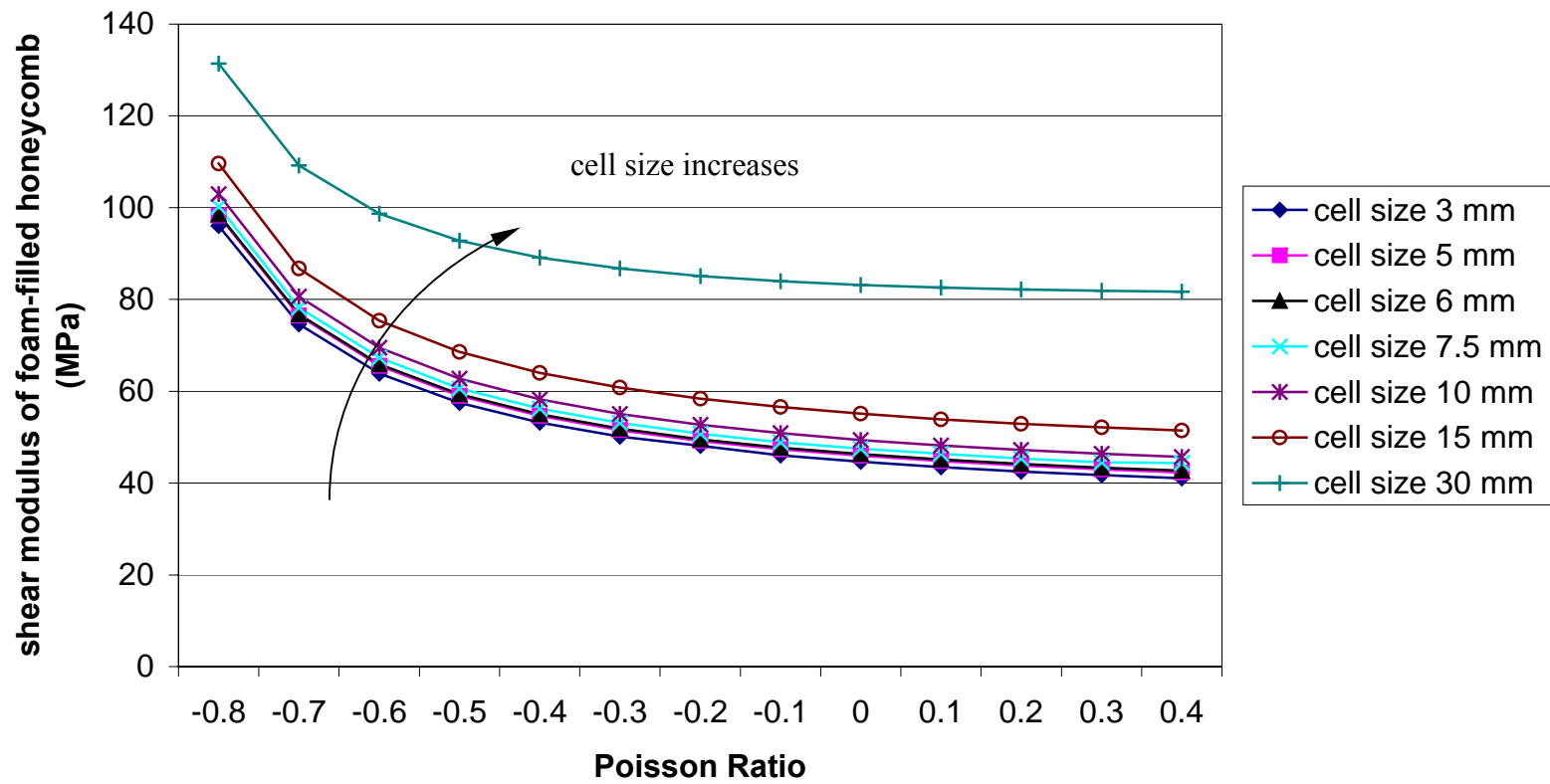


Figure 6.8. Influence of Poisson's ratio on the shear modulus of foam-filled honeycomb structures.

## CHAPTER 7 CONCLUSIONS

The research objects in this dissertation are sandwich beams and plates with the core made of paper honeycomb filled with polyurethane foam. The honeycomb material is expected to increase the stiffness of the entire structure, and the foam improves the damping. In this research, the static strain-stress relationship was studied, and the equations of motion were derived using Hamilton's principle. The expressions of the wavenumber and speed of flexural wave in sandwich beams and plates were obtained. Based on both statics and dynamics studies, the frequency dependence of damping was analyzed for foam-filled honeycomb sandwich beams, in which the face sheets are much thinner than the core, or the structural parameter is large. It was found that if the face sheet thickness is increased, the damping in the low and high frequency ranges is decreased, but it remains high in the middle frequency range. If the thickness of the core is increased, the damping is increased in the middle and high frequency ranges. Delamination introduces more friction in a composite beam structure and thus makes the damping increase. However, delamination also reduces the stiffness as well as the natural frequencies of sandwich structures. Experiments on beams with different configurations and with delamination were carried out. The experimental results are consistent with the analytical predictions.

A wavelet analysis-based noise reduction technique was used for damping calculations using frequency response function analysis. Unlike the traditional digital

wavelet transform, the undecimated wavelet transform is time-invariant, and does not depend on the denoising-threshold selection which may lead to quite different results if the traditional digital wavelet transform is used. The results obtained from simulated signals show quite high accuracy.

A new damping calculation method was developed using the Gabor transform and Gabor spectrogram. This method was developed for free vibration signals. Since the amplitude of free vibration signal decreases exponentially, the signal is not stationary. Both linear and quadratic Gabor analyses can decompose the signal onto the joint time-frequency domain, and have a globally optimal time-frequency resolution compared to the wavelet analysis. By using the Gabor transform and expansion (linear Gabor analysis), the time signal can be reconstructed after a noise reduction process in the time-frequency domain. The complex analytic signal of the reconstructed time signal is then constructed using the Hilbert transform. Then the damping ratio can be calculated based on the best exponential fit of the analytic signal's envelope. The Gabor spectrogram method cannot be used to reconstruct the time signal, but it can be used to calculate the damping ratio using ridge detection techniques.

The linear Gabor transform and expansion procedure can also be applied to modal testing without force information. For an N-DOF system, in general a vibration signal contains the dynamic deflection of N modes if these modes are all properly excited. The Gabor transform and expansion can be used to decouple and reconstruct these modes to effectively make them into single-mode signals. Then the natural frequency, modal damping, vibration magnitude and phase can be extracted for each mode. The mode shape can also be obtained by comparing the magnitudes and phase angles at different

grid points. Compared to the FFT-based decoupling/reconstruction, the Gabor expansion method benefits from higher SNR. The measurements were made on a cantilever beam. Without any information on the excitation, the modal parameters can be obtained very well using the Gabor expansion approach.

The analysis of the sound transmission loss of foam-filled honeycomb sandwich panels was carried out. A theoretical model was developed using the statistical energy analysis (SEA) method. For a given sandwich panel, the sound transmission loss depends on its internal damping, modal density and radiation efficiency. The internal damping can be estimated using the method presented in Chapter 3. The modal density can be obtained by calculating the wavenumber using a bi-cubic function. A parameter study was made for the sound transmission loss. It can be concluded that an increase in the core thickness will increase the critical frequency. Two measurement methods, the two-room method, and the sound intensity method, were compared. The sound intensity method is less complicated than the two-room method, but restricted in an optimal frequency band which is narrower than that in the two-room method. Measurements on six different panels, including two isotropic aluminum panels and four sandwich panels, were carried out using the two-room method. Simulations of the radiation efficiency and sound transmission loss were conducted using AutoSEA software. The measured results agree with quite well with the results simulated using AutoSEA. It was found that the radiation efficiency of the foam-filled honeycomb sandwich panels does not decrease at frequencies beyond the critical frequency. The surface densities of the sandwich panels are much smaller than those of the aluminum panels. The measured results show that the overall sound transmission loss values of sandwich panels are smaller than those of the

aluminum panels. This implies that the surface density still dominates the overall transmission loss behavior of these panels. The foam-filled honeycomb sandwich design does not show any sound reduction advantage over their heavier metal counterparts, although the sandwich structures have higher damping capacity. That means such a foam-filled honeycomb sandwich design must be modified to obtain higher sound transmission loss properties. The measured transmission loss curves also show that the critical frequency increases as the core thickness is increased, if other parameters do not change, which agrees with the theoretical prediction.

The honeycomb cell size effects on the Young's modulus and the shear modulus of the foam-filled honeycomb structures were studied using finite element models developed in ANSYS. As the cell size is decreased, the honeycomb cells become denser, and the honeycomb frame is more resistant to external loads, although the volume ratio is smaller. This effect increases the Young's modulus. Reference [153] studied the cell size effect of pure honeycomb structures, and reported the same trend for integer values of  $\alpha$ , the number of cells in the width direction, while for non-integer values of  $\alpha$ , the Young's modulus was found to decrease as  $\alpha$  is increased from one integer to the next. However, for foam-filled honeycomb structures, the Young's modulus does not decrease as non-integer values of  $\alpha$  increase from one integer to the next. For pure honeycomb structures, only longitudinal cell walls carry the external loads. When non-integer values of  $\alpha$  are increased from one integer to the next, the number of longitudinal cell walls in the width direction does not increase, but the cross-section area increases. On the contrary, for the foam-filled honeycomb structures, the longitudinal honeycomb cell walls, as well as the foam, carry the external loads. Even when non-integer value of  $\alpha$  is increased, the foam



in those open cells still can carry external loads. The shear modulus, on the other hand, decreases as the cell size is decreased. This is because the cell walls become thinner, which decreases the constraints at the boundary.

Hexagonal honeycomb structures always have positive Poisson's ratio. However, polyurethane foam can possess a negative value of Poisson's ratio. By filling honeycomb cores with foam having a negative value of Poisson's ratio, both the Young's modulus and the shear modulus increase dramatically. It is worth noticing that the effects of cell size and Poisson's ratio may have opposite effects and can be used to achieve different functional purposes with sandwich structures. A trade-off between the overall stiffness and the sound transmission properties may be made in the design stage.

This research work has approved that the foam-filled honeycomb sandwich design does not show any advantage of sound reduction advantaged over their heavier metal counterparts, although the sandwich structures have higher damping capacity. So an important future work is to improve the sound transmission properties of sandwich structures using different design or different material elements, such as braided material and nano-material.

## REFERENCES

- [1] D. Zenkert, *An Introduction to Sandwich Construction*. EMAS publishing, London (1997)
- [2] D. Zenkert, *The Handbook of Sandwich Construction*. EMAS publishing, London (1997)
- [3] J. M. Davies, *Lightweight Sandwich Construction*. Blackwell Science, Condon (2001)
- [4] W. J Jung, A. J. Aref, "A Combined Honeycomb and Solid Viscoelastic Material for Structural Damping Application", *Mechanics and Materials*. **53**(8), 831-844 (2003)
- [5] J. E. Ruzicka, *Structural Damping*. ASME, New Jersey (1959)
- [6] B. J. Lazan, *Damping of Materials and Members in Structural Mechanics*. Pergamon Press, London (1968)
- [7] A. D. Nashif, D. I. G. Jones, J. P. Henderson, *Vibration Damping*. John Wiley & Sons, Inc., New York (1985)
- [8] D. I. G. Jones, *Handbook of Viscoelastic Vibration Damping*. John Wiley & Sons, Inc., New York (2001)
- [9] C. T. Sun, Y. P. Lu, *Vibration Damping of Structural Elements*. Prentice Hall PTR, Englewood Cliffs, NJ (1995)
- [10] C. F. Beards, *Structural Vibration Analysis: Modeling, Analysis, and Damping of Vibrating Structures*. Halsted Press, Chichester (1983)
- [11] E. E. Ungar, "Structural Damping", Chapter 12 in *Noise and Vibration Control Engineering: Principles and Applications*, Leo. L. Beranek (Editor). John Wiley & Sons, Inc. (1992)
- [12] D. J. Mead, *Passive Vibration Control*. John Wiley & Sons, New York (1999)
- [13] R. H. Lyon, G. Maidanik, "Power Flow between Linearly Coupled Oscillators", *Journal of the Acoustical Society of America*. **34**(5), 623-639 (1962)
- [14] G. Maidanik, "Response of Ribbed Panels to Reverberant Acoustic Fields", *Journal of the Acoustical Society of America*. **34**(6), 809-826 (1962)
- [15] M. J. Crocker, A. J. Price, "Sound Transmission using Statistical Energy Analysis", *Journal of Sound and Vibration*. **9**(3), 469-486 (1969)
- [16] B. L. Clarkson, K. T. Brown, "Acoustic Radiation Damping", *ASME Journal of Vibration, Acoustics, Stress and Reliability in Design*. **107**, 357-360 (1985)

- [17] D. J. Mead, "Plates with Regular Stiffening in Acoustic Media; Vibration and Radiation", *Journal of the Acoustical Society of America*. **88**(1), 391-401 (1990)
- [18] S. Gade & H. Herlufsen, *Damping measurement*. Bruel and Kjaer Technical Review (1994)
- [19] M. J. Crocker, *Encyclopedia of Acoustics Vol II*. John Wiley & Sons, Inc., New York (1997)
- [20] D. J. Ewins, *Modal Testing: Theory, Practice and Application*. Research Studies Press LTD, Baldock, England (2000)
- [21] M. D. Rao, "Recent applications of viscoelastic damping for noise control in automobiles and commercial airplanes", *Journal of Sound and Vibration*. **262**(3) 457-474 (2003)
- [22] B. C. Nakra, "Vibration Control with Viscoelastic Materials", *Shock and Vibration Digest*. **8**(6), 3-12 (1976)
- [23] B. C. Nakra, "Vibration Control with Viscoelastic Materials - II", *Shock and Vibration Digest*. **13**(1), 17-20 (1981)
- [24] B. C. Nakra, "Vibration Control with Viscoelastic Materials - III", *Shock and Vibration Digest*. **16**(5), 17-22 (1984)
- [25] P. J. Torvik, "The Analysis and Design of Constrained Layer Damping Treatments", *Damping Applications for Vibration Control*. AMD-Vol 38, ASME, Chicago, IL (1980)
- [26] R. Chandra, S. P. Singh, K. Gupta, "Damping Studies in Fiber-Reinforced Composites - A Review", *Composite Structures*. **46**, 41-51 (1999)
- [27] H. G. Alalen, *Analysis and Design of Structural Sandwich Panels*. Pergamon Press, London (1969)
- [28] E. M. Kerwin, "Damping of Flexural Waves by a Constrained Viscoelastic Layer", *Journal of the Acoustical Society of America*. **31**(7), 952-962 (1959)
- [29] D. Ross, E. E. Ungar, E. M. Kerwin, "Damping of plate flexural vibrations by means of viscoelastic laminate", *Structural Damping*. 49-88, ASME, New Jersey (1959)
- [30] E. E. Ungar, "Loss Factors of Viscoelastically Damped beam Structures", *Journal of the Acoustical Society of America*. **34**(8), 1082-1089 (1962)
- [31] E. E. Ungar and E. M. Kerwin, "Loss Factors of Viscoelastic System in Terms of Energy Concepts", *Journal of the Acoustical Society of America*. **34**(7), 954-957 (1962)
- [32] J. E. Ruzicha, " Damping Structural Resonances using Viscoelastic-Damping Mechanisms, Part I Design Configurations", *ASME Journal of Engineering for Industry*. **83**, 403-413 (1961)
- [33] J. E. Ruzicha, " Damping Structural Resonances using Viscoelastic-Damping Mechanisms, Part II Experimental Results", *ASME Journal of Engineering for Industry*. **83**, 414-424 (1961)

- [34] Y. Y. Yu, "Damping of Flexural Vibrations of Sandwich Plates", *Journal of the Aerospace Sciences*. **29**, 790-803 (1962)
- [35] Y.V.K. Sadasivia Rao, B.C.Nakra, "Vibrations of Unsymmetrical Sandwich Beams and Plates with Viscoelastic Cores", *Journal of Sound and Vibration*. **34**(3), 309-326 (1974)
- [36] R. A. DiTaranto, "Theory of Vibratory Bending for Elastic and Viscoelastic Layered Finite-Length Beams", *ASME Journal of Applied Mechanics*. **32**, 881-886 (1965)
- [37] R. A. DiTaranto, W. Blasingame, "Effect of End Constraints on the Damping of Laminated Beams", *Journal of the Acoustical Society of America*. **39**(2), 405-407 (1966)
- [38] R. A. DiTaranto, W. Blasingame, "Composite Damping of Vibrating Sandwich Beams", *ASME Journal of Engineering for Industry*. **89**, 633-638 (1967)
- [39] D. J. Mead, S. Markus, "The Forced Vibration of a Three-Layer, Damped Sandwich Beam with Arbitrary Boundary Conditions", *Journal of Sound and Vibrations*. **10**(2), 163-175 (1969)
- [40] D. J. Mead, S. Markus, "Loss Factors and Resonant Frequencies of Encastred Damped Sandwich Beam", *Journal of Sound and Vibrations*. **12**(1), 99-112 (1970)
- [41] D. J. Mead, "The Damping Properties of Elastically Supported Sandwich Plates", *Journal of Sound and Vibrations*, **24**(3), 275-295 (1972)
- [42] D. J. Mead, "Governing Equations for Vibrating Constrained-Layer Damping Sandwich Plates and Beams", *ASME Journal of Applied Mechanics*. **40**, 639-640 (1973)
- [43] D. J. Mead, "Loss Factors and Resonant Frequencies of Periodic Damped Sandwich Plates", *ASME Journal of Engineering for Industry*. **98**, 75-80 (1976)
- [44] D. J. Mead, "A Comparison of Some Equations for the Flexural Vibration of Damped Sandwich Beams", *Journal of Sound and Vibrations*. **83**(3), 363-377 (1982)
- [45] M. J. Yan, E. H. Dowell, "Governing Equations for Vibrating Constrained-Layer Damping Sandwich Plates and Beams", *ASME Journal of Applied Mechanics*. **39**, 1041-1046 (1972)
- [46] M. J. Yan, E. H. Dowell, "Elastic Sandwich Beam or Plate Equations Equivalent to Classical Theory", *ASME Journal of Applied Mechanics*. **41**, 526-527 (1974)
- [47] P. Cupial and J. Niziol, "Vibration and Damping Analysis of a Three-Layered Composite Plate with a Viscoelastic Mid-Layer", *Journal of Sound and Vibrations*. **183**(1), 99-114 (1995)
- [48] Horng-Jou Wang, Lien-Wen Chen, "Vibration and damping analysis of a three-layered composite annular plate with a viscoelastic mid-layer", *Composite Structures*. **58**, 563-570 (2002)
- [49] S. He, M. D. Rao, "Vibration and Damping Analysis of Multi-Span Sandwich Beams with Arbitrary Boundary Conditions", *Journal of Sound and Vibration*. **164**(1) 125-142 (1993)

- [50] D. K. Rao, "Vibration of Short Sandwich Beams", *Journal of Sound and Vibration*. **52**(2), 253-263 (1977)
- [51] D. K. Rao, "Frequency and Loss Factors of Sandwich Beams under Various Boundary Conditions", *Journal of Mechanical Engineering Science*. **20**(5), 271-282 (1978)
- [52] S. J. Hwang, R. F. Gibson, "The Use of Strain energy-Based Finite Element Techniques in the Analysis of Various Aspects of Damping of Composite Material and Structures", *J. Composite Materials*. **26**(17), 2585-2605 (1992)
- [53] S. J. Hwang, R. F. Gibson, "The effects of Three-Dimensional States of Stress on Damping of Laminated Composites", *Composites Science and Technology*. **41**, 379-393 (1991)
- [54] S. J. Hwang, R. F. Gibson, J. Singh, "Decomposition of Coupling effects on Damping of Laminated Composites under Flexural Vibration", *Composites Science and Technology*. **43**, 159-169 (1992)
- [55] R. F. Gibson, *Principles of Composite Mechanics*. McGraw-Hill, New York (1994)
- [56] S. J. Hwang, R. F. Gibson, "Contribution of Interlaminar Stresses to Damping in Thick Laminated Composites under Uniaxial Extension", *Composite Structures*. **20**, 29-35 (1992)
- [57] B. J. Lazan, "Energy Dissipation Mechanisms in Structures, with Particular Reference to Material Damping", *Structural Damping*. 1-34, ASME, New Jersey (1959)
- [58] A. C. Nilsson, "Wave propagation in and sound transmission through sandwich plates", *Journal of Sound and Vibration*. **138**(1), 73-94 (1990)
- [59] E. Nilsson, A. C. Nilsson, "Prediction and measurement of some dynamic properties of sandwich structures with honeycomb and foam cores", *Journal of Sound and Vibration*. **251**(3), 409-430 (2002)
- [60] A. W. van Vuure, I. Verpoest, F. K. Ko, "Sandwich-Fabric Panels as Spacers in a Constrained Layer Structural Damping Application", *Composites Part B: Engineering*. **32**, 11-19 (2001)
- [61] J. A. Agbasiere, P. Groothenhuis, "Flexural Vibration of Symmetrical Multi-Layer Beams with Viscoelastic Damping", *Journal of Engineering Science*. **10**(3), 269-281 (1968)
- [62] P. Groothenhuis, "The Control of Vibrations with Viscoelastic Materials", *Journal of Sound and Vibration*. **11**(4), 421-433 (1970)
- [63] B. C. Nakra, P. Groothenhuis, "Structural Damping Using a Four-Layer Sandwich", *ASME Journal of Engineering for Industry*. **94**, 81-86 (1972)
- [64] N. T. Asnani, B. C. Nakra, "Vibration Damping Characteristics of Multilayered Beams with Constrained Viscoelastic Layers", *ASME Journal of Engineering for Industry*. **98**, 895-901 (1976)

- [65] N. Alam, N. T. Asnani, "Vibration and Damping Analysis of Multilayered Rectangular Plates with Constrained Viscoelastic Layers", *Journal of Sound and Vibration*. **97**(4), 597-614 (1984)
- [66] N. Alam, N. T. Asnani, "Vibration and Damping Analysis of Fibre einforced Composite Material Plates", *Journal of Composite Materials*. **20**, 2-18 (1986)
- [67] N. Alam, N. T. Asnani, "Refined Vibration and Damping Analysis of Multilayered Rectangular Plates", *Journal of Sound and Vibration*. **119**(2), 347-362 (1987)
- [68] A. Bhmaradi, "Sandwich Beam Theory and the Analysis of Constrained Layer Damping", *Journal of Sound and Vibration*. **179**(4), 591-602 (1995)
- [69] M. D. Rao, S. He, "Dynamic Analysis and Design of Laminated Composite Beams with Multiple Damping Layers", *AIAA Journal*. **31**(4), 736-745 (1993)
- [70] S. He, M. D. Rao, "Longitudinal Vibration and Damping Analysis of Adhesively Bonded Double Strap Joints", *ASME Journal of Vibration and Acoustics*. **114**, 330-337 (1992)
- [71] B. K. Nanda, A. K. Behera, "Damping in Layered and Jointed Structure", *International Journal of Acoustics and Vibration*. **5**(2), 89-95 (2000)
- [72] E. R. Marsh, L. C. Hale, "Damping of Flexural Waves with Imbedded Viscoelastic Materials", *ASME Journal of Vibration and Acoustics*. **120**, 188-193 (1998)
- [73] S. Prasad, L. A. Carlsson, "Debonding and Crack Kinking in Foam Core Sandwich Beams – I. Analysis of Fracture Specimens", *Engineering Fracture Mechanics*. **47**(6), 813-824 (1994)
- [74] S. Prasad, L. A. Carlsson, "Debonding and Crack Kinking in Foam Core Sandwich Beams – II. Experimental Investigation", *Engineering Fracture Mechanics*. **47**(6), 825-841 (1994)
- [75] H. Luo, S. Hanagud, "Dynamics of Delaminated Beams", *International journal of Solid and Structures*. **37**(10), 1501-1519 (2000)
- [76] H.Y. Kim, W. Hwang, "Effect of Debonding on Natural Frequencies and Frequency response Functions of Honeycomb Sandwich Beams", *Composite Structures*. **55**, 51-62 (2002)
- [77] Y. Frostig, "Behavior of delaminated sandwich beam with transversely flexible core — high order theory", *Composite Structures*. **20**(1), 1-16 (1992)
- [78] D. J. Mead, "Criteria for Comparing the Effectiveness of Damping Treatments" *Noise Control*. **7**, 27-38 (1961)
- [79] Y. P. Lu, B. E. Douglas, "On the Forced Vibrations of Three-Layer Damped Sandwich Beams", *Journal of Sound and Vibration*. **32**(4), 513-516 (1974)
- [80] Y. P. Lu, J. W. Killian, G. C. Everstine, "Vibrations of Three Layered Damped Sandwich Plate Composites", *Journal of Sound and Vibration*. **64**(1), 63-71 (1979)
- [81] Y. P. Lu, G. C. Everstine, "More One Finite Element Modeling of Damped Composite Systems", *Journal of Sound and Vibration*. **69**(2), 199-205 (1980)

- [82] J. W. Killian, Y. P. Lu, "A Finite Element Modeling Approximation for Damping Material Used in Constrained Damped Structures", *Journal of Sound and Vibration*. **97**(2), 352-354 (1984)
- [83] Y. P. Lu, J. C. Clemens, A. J. Roscoe, "Vibrations of Composite Plate Structures Consisting of a Constrained-Layer Damping Sandwich with Viscoelastic Core", *Journal of Sound and Vibration*. **153**(3), 552-558 (1992)
- [84] C. D. Johnson, D. A. Kienholz, "Finite element prediction of damping in structures with constrained viscoelastic layers", *AIAA Journal*. **20**(9), 1284-1290 (1981)
- [85] D. E. Veley, S. S. Rao, "Two-dimensional finite element modeling of constrained layer damping", *Smart structures and Materials 1994: Passive Damping*, C. D. Johnson (Editor), Proc. SPIE 2193. 276-283 (1994)
- [86] A. Zambrano, J. A. Inaudi, J. M. Kelly, "Accuracy of the Modal Strain Energy Method", *Smart structures and Materials 1994: Passive Damping*, C. D. Johnson (Editor), Proc. SPIE 2193. 284-295 (1994)
- [87] T. S. Plagianakos, D. A. Saravanos, "High-Order Layerwise Mechanics and Finite Element for the Damped Dynamic Characteristics of Sandwich Composite Beams", *International journal of Solid and Structures*. **41**(24-25), 6853-6871 (2004)
- [88] P. J. Shorter, "Wave propagation and damping in linear viscoelastic laminates", *Journal of the Acoustical Society of America*. **115**(5), 1917-1925 (2004)
- [89] D. J. McTavish, P. C. Hughes, Finite element modeling of linear viscoelastic structures: the GHM method. *Proceedings of 33<sup>rd</sup> AIAA/ASME/ASCE/AHS/AHS Structures, Structural Dynamics and Materials Conference*, Paper No. AIAA-92-2380-CP. (1992)
- [90] G. Wang, S. Veeramani, N. M. Wereley, Analysis of sandwich plates with isotropic face plates and a viscoelastic core. *ASME Journal of Vibration and Acoustics*. **122**, 305-312 (2000)
- [91] X. Chen, H. L. Chen, X. L. Hu, "Damping Prediction of Sandwich Structures by Order-Reduction-Iteration Approach", *Journal of Sound and Vibration*. **222**(5), 803-812 (1999)
- [92] S. A. Nayfeh, "Damping of flexural vibration in the plane of lamination of elastic-viscoelastic sandwich beams", *Journal of Sound and Vibration*. **276**(3-5), 689-711 (2004)
- [93] R. H. Lyon, R. G. DeJong, *Theory and Applications of Statistical Energy Analysis*. RH Lyon Corp, Massachusetts (1998)
- [94] B. Bloss, M. D. Rao, "Measurements of Damping in Structures by the Power Input Method", *Experimental Techniques*. **26**(3), 30-33 (2002)
- [95] J.P.D. Wilkinson, "Modal Densities of Certain Shallow Structural Elements", *Journal of the Acoustical Society of America*. **43**(2), 245-251 (1968)
- [96] L.L Erickson, "Modal Densities of Sandwich Panels: Theory and Experiment", *The Shock and Vibration Bulletin*. **39**(3), 1-16 (1969)

- [97] B. L. Clarkson, R J Pope, "Experimental determination of modal densities and loss factors of flat plates and cylinders", *Journal of Sound and Vibration*. **77**(4), 535-549 (1981)
- [98] B. L. Clarkson, "The derivation of modal densities from point impedances", *Journal of Sound and Vibration*. **77**(4), 583-584, (1981)
- [99] M. F. Ranky, B. L. Clarkson, "Frequency averaged loss factors of plates and shells", *Journal of Sound and Vibration*. **89**(3), 309-323 (1983)
- [100] B. L. Clarkson, M. F. Ranky, "Modal density of honeycomb plates", *Journal of Sound and Vibration*. **91**(1), 103-118 (1983)
- [101] K. T. Brown, "Measurement of modal density: an improved technique for use on lightly damped structures", *Journal of Sound and Vibration*. **96**(1), 127-132 (1984)
- [102] K. T. Brown, M. P. Norton, "Some comments on the experimental determination of modal densities and loss factors for statistical energy analysis applications", *Journal of Sound and Vibration*. **102**(4), 588-594 (1985)
- [103] P.R. Keswick, M. P. Norton, "A Comparison of Modal Density Measurement Techniques", *Applied Acoustics*. **20** (2), 137-153 (1987)
- [104] B. Hakansson, P. Carlsson, "Bias Errors in Mechanical Impedance Data Obtained with Impedance Head", *Journal of Sound and Vibration*. **113**(1), 173-183 (1987)
- [105] K. Renji, P. S. Nair and S. Narayanan, "Modal density of composite honeycomb sandwich panels" *Journal of Sound and Vibration*. **195** (5), 687-699 (1996)
- [106] K. Renji, "Experimental modal densities of honeycomb sandwich panels at high frequencies", *Journal of Sound and Vibration*. **237**(1), 67-79 (2000)
- [107] K. Renji, S. Narayan, "Loss factors of composite honeycomb sandwich panels", *Journal of Sound and Vibration*. **250**(4), 745-761 (2002)
- [108] M. P. Norton, *Fundamentals of Noise and Vibration Analysis for Engineers*. Cambridge University Press, New York (1989)
- [109] M. Serrige and T. R. Licht, *Piezoelectric Accelerometers and Vibration Preamplifiers Handbook*. Bruel & Kjaer, Naerum, Denmark (1987)
- [110] D. Rormenti, M. Richardson, "Parameter estimation from frequency response measurements using rational fraction polynomials," *20<sup>th</sup> International Modal Analysis Conference*. (2002)
- [111] M. Richardson, B. Schwarz, "Modal parameter estimation from operating data," in *Sound and Vibration Magazine*. **37**(1), 28-36 (2003)
- [112] L. Cohen, *Time-Frequency Analysis*. Prentice Hall PTR, Englewood Cliffs (1995)
- [113] S. Qian, *Introduction to Time-Frequency and Wavelet Transforms*. Prentice Hall PTR, Upper Saddle River (2002)
- [114] National Instruments, *Signal Processing Toolset User Manual*. (2001)



- [115] G. Strang, T. Nguyen, *Wavelets and Filter Banks*. Wellesley-Cambridge Press, Cambridge (1995)
- [116] H. Shao, W. Jin, S. Qian, "Order tracking by discrete Gabor expansion", in *IEEE Transactions on Instrumentation and Measurement*. **52**(3), 754-761 (2003)
- [117] M. J. Shensa, "The Discrete Wavelet Transform: Wedding the A Trous and Mallat Algorithms", *IEEE Trans on Signal Processing*. **40**(10), 2464-2482 (1992)
- [118] M. Jansen 2001 *Noise Reduction by Wavelet Thresholding*. Springer, New York (2001)
- [119] D. Donoho, "De-Noising by Soft-Thresholding", *IEEE Transactions on Information Theory*. **41**(3), 613-627 (1995)
- [120] B. Schwarz, M. Richardson, "Modal parameter estimation from ambient response data," *19<sup>th</sup> International Modal Analysis Conference*. (2001)
- [121] P. Bonato, R. Ceravolo, A. De Stefano, "Use of cross-time-frequency estimators for structural identification in non-stationary conditions and under unknown excitation," *Journal of Sound and Vibration*. **237**(5), 775-791 (2003)
- [122] W. J. Staszewski, "Identification of damping in MDOF systems using time-scale decomposition," *Journal of Sound and Vibration*. **203**(2), 283-305 (1997)
- [123] J. Lardies, S. Gouttebroze, "Identification of modal parameters using the wavelet transform," *Mechanical Sciences*. **44**, 2263-2283 (2002)
- [124] R. Carmona, W. Hwang, B. Toetersani, *Practical Time-Frequency Analysis: Gabor and Wavelet Transforms with an Implementation in S*. Academic Press, San Diego (1998)
- [125] G. V. Welland, *Beyond Wavelets*. Academic Press, San Diego (2003)
- [126] T. K. Caughey, "Classical normal modes in damped linear dynamic systems," *Journal of Applied Mechanics*. **27**, 69-271 (1960)
- [127] L. L. Beranek, I. L. Ver, "Noise and vibration control engineering-principles and applications". John Wiley&Sons, Inc. (1992)
- [128] M. J. Crocker, F. M. Kessler, *Noise and noise control Vol. II*. CRC Press, Cleveland (1982)
- [129] G. Kurtze, B.G. Watters, "New Wall Design for High Transmission Loss or High Damping", *Journal of the Acoustical Society of America*. **31**(6), 739-748 (1959)
- [130] R. D. Ford, P. Lord, A. W. Walker, "Sound Transmission through Sandwich Constructions", *Journal of Sound and Vibration*. **5**(1), 9-21 (1967)
- [131] C.P. Smolenski, E. M. Krokosky, " Dilatational-Mode Sound Transmission in Sandwich Panels", *Journal of the Acoustical Society of America*. **54**(6), 1449-1457 (1973)
- [132] C. L. Dym, M. A. Lang, "Transmission of Sound through Sandwich Panels", *Journal of the Acoustical Society of America*. **56**(5), 1523-1532 (1974)

- [133] M. A. Lang, C. L. Dym, "Optimal Acoustic Design of Sandwich Panels", *Journal of the Acoustical Society of America*. **57**(6), 1481-1487 (1975)
- [134] C. L. Dym, C. S. Ventres, M. A. Lang, "Transmission of Sound through Sandwich Panels: A Reconsideration", *Journal of the Acoustical Society of America*. **59**(2), 364-367 (1976)
- [135] C. L. Dym, D. C. Lang, "Transmission Loss of Damped Asymmetric Sandwich Panels with Orthotropic Cores", *Journal of Sound and Vibration*. **88**(3), 299-319 (1983)
- [136] S. E. Markris, C. L. Dym, J. M. Smith, "Transmission Loss Optimization in Acoustic Sandwich Panels", *Journal of the Acoustical Society of America*. **79**(6), 1833-1843 (1986)
- [137] A. Ordubadi, R. H. Lyon, "Effect of Orthotropy on the Sound Transmission through Plywood Panels", *Journal of the Acoustical Society of America*. **65**(1), 133-139 (1979)
- [138] S. Narayanan, R. L. Shanbhag, "Sound Transmission through Elastically Supported Sandwich Panels into a Rectangular Enclosure", *Journal of Sound and Vibration*. **77**(2), 251-270 (1981)
- [139] S. Narayanan, R. L. Shanbhag, "Sound Transmission through a Damped Sandwich Panels", *Journal of Sound and Vibration*. **80**(3), 315-327 (1982)
- [140] J. A. Moore, R. H. Lyon, "Sound Transmission Loss Characteristics of Sandwich Panel Constructions", *Journal of the Acoustical Society of America*. **89**(2), 777-791 (1991)
- [141] T. Wang, V. Sokilinsky, S. Rajaram, S. R. Nutt, "Assessment of Sandwich Models for the Prediction of Sound Transmission Loss in Unidirectional Sandwich Panels", *Applied Acoustics*. **66**(3), 245-262 (2005)
- [142] J. L. Guyader, C. Lesueur, "Acoustic Transmission through Orthotropic Multilayered Plates, Part I: Plate Vibration Modes", *Journal of Sound and Vibration*. **58**(1), 51-68 (1978)
- [143] J. L. Guyader, C. Lesueur, "Acoustic Transmission through Orthotropic Multilayered Plates, Part II: Transmission Loss", *Journal of Sound and Vibration*. **58**(1), 69-86 (1978)
- [144] J. L. Guyader, C. Lesueur, "Transmission of Reverberant Sound through Orthotropic, Viscoelastic Multilayered Plates", *Journal of Sound and Vibration*. **70**(3), 319-332 (1980)
- [145] R. Panneton, N. Atalla, "Numerical Prediction of Sound Transmission through Finite Multilayer Systems with Poroelastic Materials", *Journal of the Acoustical Society of America*. **100**(1), 346-354 (1996)
- [146] S. Kurra, D. Arditi, "Determination of Sound Transmission Loss of Multilayered Elements, Part I: Prediction and Measured Results", *Acta Acustica*. **87**(5), 582-591 (2001)

- [147] S. Kurra, D. Arditi, “ Determination of Sound Transmission Loss of Multilayered Elements, Part2: An experimental Study”, *Acta Acustics*. **87**(5), 592-603 (2001)
- [148] A. Uris, H. Estelles, “Experimental Sound Transmission Improvement in Multilayered Sandwich Partitions”, *Journal of Noise Control Engineering*. **50**(5), 157-159 (2002)
- [149] M. J. Crocker, *The Response of Structures to Acoustic Excitation and the Transmission of Sound and Vibration*. Doctoral Thesis, University of Liverpool (1969)
- [150] F. J. Fay, “Measurement of Acoustic Intensity using the Cross-Spectral Density of Two Microphone Signals”, *Journal of the Acoustical Society of America*. **62**(4), 1057-1059 (1977)
- [151] M. P. Waser, M. J. Crocker, “Introduction to the Two-Microphone Cross-Spectral Method of Determining Sound Intensity”, *Noise Control Engineering*. **22**, 76-85 (1984)
- [152] A. Cops, M. Minten, “Comparative Study Between the Sound Intensity Method and the Conventional Two-Room Method to Calculate the Sound Transmission Loss of Wall Constructions”, *Noise Control Engineering*. **22**, 104-111 (1984)
- [153] P.R. Onck, E.W. Andrews, L.J. Gibson, “Size Effects in Ductile Cellular Solids. Part I: Modeling”, *International Journal of Mechanical Sciences*. **43**(3), 681-699 (2001)
- [154] E.W. Andrews, G. Gioux, P. Onck, L.J. Gibson, “Size Effects in Ductile Cellular Solids. Part II: Experimental Results”, *International Journal of Mechanical Sciences*. **43**(3), 701-713 (2001)
- [155] L.J. Gibson, M. F. Ashby, *Cellular Solids*. Cambridge University Press, Cambridge, United Kingdom (1997)
- [155] M. S. Thompson, I. D. McCarthy, L. Lidgren, L. Ryd, “Compressive and Shear Properties of Commercially Available Polyurethane Foams”, *Journal of Biomechanical Engineering*. **125**(5), 732-734 (2003)
- [156] J. M. Gere, S. P. Timoshenko, *Mechanics of Materials*. PWS Publishing Company, Boston (1997)

## APPENDICES

**APPENDIX A**

**MATLAB PROGRAMS FOR WAVENUMBER AND WAVE SPEED OF**

**SANDWICH PANELS**

**A1 Sandwich Panel with Isotropic Core**

```

E1 = 2.5e10;
rho1 = 2250.;
v1 = 0.3;
t1 = 3.3e-4;
G2 = 5.06e7;
rho2 = 155.;
v2 = 0.2;
E2 = G2*2*(1+v2);
t2 = 6.35e-3;
S2 = G2*t2;

Bc = E1/(1-v1^2)*(t1^3+3*t1*(t1+t2)^2)/6+E2*t2^3/(1-v2^2)/12;
M1 = rho1*t1;
M2 = rho2*t2;
Mc = 2*M1+M2;
B1 = E1*t1^3/12/(1-v1^2);

% Frequency-dependant wavenumber in the plate "k"
for i=1:500
    f(i)=10+100*(i-1); %from 100Hz to 10000Hz
    w(i)=2*pi*f(i);
    i
    syms kp;
    eq1=2*Bc*B1*kp^6+Bc*S2*kp^4-w(i)^2*Mc*(Bc+2*B1)*kp^2-w(i)^2*Mc*S2;
    kp=solve(eq1, 'kp');
    k(i)=real(double(kp(1)));
end
% wave speed in the sandwich plate

cp = w./k;
ca = 343;
cs = sqrt(S2/Mc);
cb_composite = sqrt(w)*sqrt(sqrt(Bc/Mc));
cb_skin_halfcore = sqrt(w)*sqrt(sqrt(2*B1/Mc));
% Critical frequency
P = 2*Bc*B1;
Q = Bc*S2*ca^2-Mc*(Bc+2*B1)*ca^4;
R = -Mc*S2*ca^6;
fc = 1/(2*pi)*sqrt((-Q+sqrt(Q^2-4*P*R))/(2*P))

```

```

figure;
loglog(f,cp,f,ca,f,cs,f,cb_composite,f,cb_skin_halfcore);
ylabel ('speed of wave propagation (m/s)');
xlabel ('Frequency (Hz)');

```

## A2 Sandwich Panel with Orthotropic Core

```

E1 = 2.5e10;
rho1 = 2250.;
v1 = 0.3;
t1 = 6.35e-3;
E11 = 5e6;
E22 = E11;
E33 = 1.08e8;
E12 = 4e5;
E13 = E12;
E23 = E12;
E44 = 5e7;
E55 = 2.3e7;
E66 = 2.3e5;
rho2 = 155;
t2 = 73.5e-3;
% Angle varying material properties
C = [4e6 4e5 4e5 0 0 0;4e5 3.7e8 4e5 0 0 0;4e5 4e5 4e6 0 0 0;0 0 0 5e7
0 0;0 0 0 0 2.3e7 0;0 0 0 0 0 2.3e5];
theta = 0;
m = cos(theta);
n = sin(theta);
T1 = [m^2 n^2 0 0 0 2*m*n;n^2 m^2 0 0 0 -2*m*n;0 0 1 0 0 0;0 0 0 m -n
0;0 0 0 n m 0;-m*n m*n 0 0 0 m^2-n^2];
T2 = [m^2 n^2 0 0 0 m*n;n^2 m^2 0 0 0 -m*n;0 0 1 0 0 0;0 0 0 m -n 0;0 0
0 n m 0;0 0 0 0 0 m^2-n^2];
C1 = inv(T1)*C*T2;
S = inv(C1);
E2 = 1/S(2,2);
v2 = -S(1,2)*E2;
G2 = 1/S(4,4);
S2 = G2*t2;

Bc = E1/(1-v1^2)*(t1^3+3*t1*(t1+t2)^2)/6+E2*t2^3/(1-v2^2)/12;
M1 = rho1*t1;
M2 = rho2*t2;
Mc = 2*M1+M2;
B1 = E1*t1^3/12/(1-v1^2);

% Frequency dependant wavenumber in the plate "k"
for i = 1:100
    f(i) = 100+100*(i-1); %from 100Hz to 10000Hz
    w(i) = 2*pi*f(i);
%
    syms kp;
    eq1 = 2*Bc*B1*kp^6+Bc*S2*kp^4-w(i)^2*Mc*(Bc+2*B1)*kp^2-w(i)^2*Mc*S2;
    kp = solve(eq1, 'kp');
    k(i) = real(double(kp(1)));
end

```

```

% Various wave speed in the sandwich plate
cp = w./k;
ca = 343;
cs = sqrt(S2/Mc);
cb_composite = sqrt(w)*sqrt(sqrt(Bc/Mc));
cb_skin_halfcore = sqrt(w)*sqrt(sqrt(2*B1/Mc));

% Critical frequency
P = 2*Bc*B1;
Q = Bc*S2*ca^2-Mc*(Bc+2*B1)*ca^4;
R = -Mc*S2*ca^6;
fc = 1/(2*pi)*sqrt((-Q+sqrt(Q^2-4*P*R))/(2*P));

figure;
loglog(f,cp,f,ca,f,cs,f,cb_composite,f,cb_skin_halfcore);
ylabel ('speed of wave propagation (m/s)');
xlabel ('Frequency (Hz)');

```

## APPENDIX B

### MATERIAL PROPERTIES OF SANDWICH PLATES

#### Face sheet (isothotropic):

$$\rho = 2250 \text{ kg/m}^3$$

$$E = 25 \text{ GPa}$$

$$\nu = 0.2$$

$$G = 10.4 \text{ GPa}$$

#### Core (orthotropic):

$$\rho = 155 \text{ kg/m}^3$$

$$E_{11} = E_{22} = 34 \text{ MPa}$$

$$E_{33} = 108 \text{ MPa}$$

$$\nu_{12} = \nu_{23} = \nu_{31} = 0.2$$

$$G_{12} = 2 \text{ MPa}$$

$$G_{23} = 41 \text{ MPa}$$

$$G_{31} = 63 \text{ MPa}$$



## NOMENCLATURE

$A$	beam cross-sectional area, amplitude
$A_p$	plate area
$C$	damping coefficient, Gabor coefficient
$C_c$	critical damping coefficient
$C_p$	speed of wave in plate
$\hat{C}$	modified Gabor coefficient
$D$	bending stiffness, honeycomb cell size, order of the Gabor spectrogram
$E$	Young's modulus, expected value
$F$	force
$H$	the Hilbert transform
$G$	shear modulus, cross-spectrum
$I$	moment of inertia of area
$J$	mass moment of inertia per unit length
$K$	stiffness
$L$	beam length, data sample length
$L_I$	sound intensity level
$L_p$	sound pressure level
$M$	mass, bending moment, mask function
$N$	total number of frequency lines, modal count
$Q$	quality factor, first moment of area
$R_{\text{rad}}$	radiation resistance
$S$	power spectral density
$T$	kinetic energy, discrete time sampling interval
$T_R$	reverberation time
$U$	potential energy
$V$	shear force, volume

$W$	energy, power
$WVD$	Wigner-Ville distribution
$X$	shear parameter
$Y$	structural parameter
$Z$	impedance
$a$	plate side length, scaling factor
$b$	beam width, plate side length, translation factor
$c$	wave speed
$d$	distance between the neutral axis of the top and bottom face sheets
$f$	frequency, force
$g$	elementary frequency of the Gabor transform, shear parameter
$h$	synthesis function
$k$	wavenumber, discrete data sample index
$k'$	shear coefficient
$l$	honeycomb cell wall length
$m$	mass per unit length, integer
$n$	modal density, integer, noise in signal
$p$	pressure
$r$	ratio of top face sheet thickness to bottom face sheet thickness
$s$	real signal
$t$	thickness
$v$	velocity
$w$	flexural displacement
$x, y$	coordinates, time signal
$\hat{x}$	reconstructed time signal
$z$	coordinate in the thickness direction of a beam or a plate
$\Pi$	power of the best exponential fit
$\Phi$	phase angle
$\Omega$	discrete frequency interval

$\alpha$	number of honeycomb cells in the width direction of a beam
$\beta$	bending deformation, loss factor in the core
$\gamma$	shear deformation, analysis function
$\zeta$	damping ratio
$\eta$	loss factor
$\kappa$	radius of gyration
$\nu$	Poisson's ratio
$\rho$	density
$\rho_s$	surface density
$\sigma$	normal stress
$\sigma_{\text{rad}}$	radiation efficiency
$\tau$	shear stress, time delay in convolution and the Hilbert transform
$\phi$	phase angle
$\psi$	mother wavelet function
$\omega$	angular frequency